Quantification of fatigue damage in AISI 316L Stainless Steel using X-Ray Powder Diffraction (XRD)

Prepared by:

Duduzile Ramasimong

MLTDUD001

Department of Mechanical Engineering

University of Cape Town

Supervised by:

Professor Robert Knutsen (University of Cape Town)

Co-supervised by:

Dr Johan Westraadt (Nelson Mandela University)

November 2023

Submitted to the Department of Mechanical Engineering at the University of Cape Town in full fulfilment of the academic requirements for a Master of Science degree in Mechanical Engineering.

Abstract

Keywords: PXRD, SEM, EBSD, TEM, Fatigue, Material characterization, AISI 316L

Candidate: Duduzile Ramasimong

Supervisor: Professor Robert Knutsen

Faculty: Engineering

Degree: Master of Science

Title: Quantification of fatigue damage in AISI 316L Stainless Steel using X-Ray Diffraction

In an electricity generation utility, there was an enduring insistence on improving the efficiency, performance, and reliability of mechanical components with respect to economic challenges. Thus, the comprehension of materials and their behaviour in a typical operating environment was key to enabling and aiding capabilities in component life assessments. Fatigue damage was among the major issues in engineering, as it increased with the number of applied loading cycles in a cumulative manner and could lead to fracture and failure of the considered part.

This study systematically investigated the microstructural changes in a material due to cyclic stressing using a non-destructive examination, Power X-ray diffraction (PXRD). In the industry, the evaluation of material deformation post-cycling loading was often performed using microscopic techniques such as transmission electron microscopy (TEM) and electron backscattered diffraction (EBSD). However, each of these techniques had its own limitations. The PXRD technique was advantageous when applied to crystalline materials, as it was sensitive to changes in the crystalline structure of the metal, thus providing a foundation for the development of a capability to enable the early detection of fatigue damage with the aim of improving asset management. The microstructural baseline undertaken in the study involved the calculation of dislocation density in the material. The evolution of dislocation density in steels was an important aspect of the mechanical response. It could potentially be used as a fingerprint to relate the material state to the life-consumption fraction in materials subjected to fatigue conditions. To

mimic the fatigue damage mechanism, cyclic loading of material specimens was performed in a laboratory.

In view of the exploratory nature of the present study, a stable single-phase austenitic microstructure, namely AISI316L stainless steel, was selected for the relative ease of characterizing dislocation development and comparison with PXRD analysis. The initial step included plotting an S-N curve for the AISI316L material in the material's annealed state following fatigue testing in the INSTRON machine. A specific stress level was selected to ensure sufficient data retrieval prior to the point of failure for the material specimen. Thereafter, candidate specimens for fatigue, including as-received and annealed specimens, formed part of the material states used in the study for microstructure analysis using three evaluation techniques. The EBSD results mostly showed good qualitative agreement with the PXRD analysis. TEM analysis was used to qualitatively visualize the individual dislocations but was very time-consuming to perform quantitatively, and the results were subject to large scatter. Validation of the PXRD techniques was performed using qualitative and quantitative TEM dislocation density results and semi-qualitative EBSD results.

This study presented a consistent approach to determining the dislocation density using a benchtop laboratory-based PXRD. The calculated dislocation density results analysed from the vast volumes of experimental data collected throughout the study highlighted important aspects to be undertaken. These included sample preparation, control of instrumentational parameters, and the correct selection of instrument modelling standards. The Williamson-Hall plot and the whole pattern fitting methods were the two evaluation techniques utilized for size and micro-strain broadening of PXRD peaks. The results proved to be repeatable owing to the systematic manner in which the number of samples used per specimen was controlled, as well as the stringent control of parameters used.

Declaration

I know the meaning of plagiarism and declare that all the work in the document, save for that which is properly acknowledged, is my own. This thesis/dissertation has been submitted to the Turnitin module (or equivalent similarity and originality checking software) and I confirm that my supervisor has seen my report and any concerns revealed by such have been resolved with my supervisor.

Signed by candidate

Name

Date

Acknowledgements

This work has been one of the defining moments in my life and career as an Eskom engineer. The journey proved to be challenging and yet satisfying for the most parts as my knowledge in the subject matter was greatly enhanced. I therefore take time to thank the vast amount of support received from several key role players. Your contribution did not go unnoticed. In Zulu we say, '*nikwenze nabakwanye'*.

- First, I would like to thank my supervisors, Professor Robert Knutsen and Dr Johan Westraadt for guidance, encouragement and stimulating discussions throughout this work.
- My collaborators Soraya von Willingh, Richard Curry and others for their assistance in running technical experiments and general support.
- The Eskom Power Plant Engineering Institute (EPPEI) and my employer Eskom are acknowledged for supporting this work financially. Including my industrial supervisor Ronnie Scheepers for providing the topics for my studies.
- Nkululeko Mfuma from Centre for HRTEM at Nelson Mandela University for the iterations performed during sample preparation i.e., mechanical polishing and electropolishing for XRD and TEM foil preparation.
- The Electron Microscope Unit at the University of Cape Town.
- The Centre for Materials Engineering (CME) at the University of Cape Town.
- The Centre for HRTEM at Nelson Mandela University.
- My mother for continuously supporting my endeavours and being a constant inspiration in this journey.
- Finally, I would like to thank my family, my husband Metsing Ramasimong, kids Phetoho and Tshepang for their enduring support during the late nights, long hours, and time away from home.

Table of contents

List of figures

List of tables

List of nomenclature

General symbols

ρ	density
α	alpha
$\boldsymbol{\theta}$	theta
$\sigma_{\bar{x}}$	Standard error of the mean (SEM)

Superscripts

‘	refers to the control volume
-	above a term indicates the term is a vector
^	above a term indicates the term is a unit vector

Abbreviations

AISI	American Iron and Steel Institute
BCC	Body-centred cubic
EBSD	Electron Back-Scattered Diffraction
FCC	Face-centred cubic
FEA	Finite Element Analysis
FPA	Fundamental Parameters Approach
FWHM	Full Width Half Maximum
GROD	Grain Reference Orientation Deviation

KAM	Kernel Average Misorientation
MATLAB	Matrix Laboratory
MTEX	MATLAB Texture Toolbox
N	Number of cycles
NIST	National Institute of Standards and Technology
PXRD	Powder X-Ray Diffraction
S	Stress
SDG	Sustainable Development Goals
SEM	Scanning Electron Microscopy
S-N	Stress (S) to Number of Cycles (N)
SRM	Standard Reference Material
STEM	Scanning Transmission Electron Microscopy
TEM	Transmission Electron Microscopy
TOPAS	Total Pattern Analysis Solution
WH	Williamson-Hall

Definitions

Dislocation	A dislocation is a lattice line defect that defines the boundary between slipped and unslipped portions of the crystal.
Dislocation density	Dislocation density is a measure of the number of dislocations in a unit volume of a crystalline material. Two methods are used to measure this parameter. In the first, the total length of dislocation line in a unit volume is measured and divided by the volume to give $\boldsymbol{\rho}D = (L / 1^3)\ m^{-2}$.

Instron	Instron is the name of a company that specializes in manufacturing testing equipment, primarily used for materials testing, including tensile, compression, and fatigue testing machines. Instron is widely known for its testing systems that help in evaluating the mechanical properties of materials, such as strength, elasticity, and durability. The company name "Instron" is derived from the combination of "instrument" and "tensile," reflecting its focus on testing equipment for materials under various stress conditions.

Chapter 1. Introduction

1.1 Background

In an electricity generation utility, there exists an enduring insistence to improve the efficiency, performance and reliability of mechanical components with respect to national economic goals and environmental goals. This study is therefore aligned to the country's sustainable development goals (SDG) 7.1 and 9.5, where the former, aims to ensure universal access to affordable, reliable and modern energy services while the latter aims to fulfil the objectives of enhancing scientific research and upgrading the technological capabilities of industrial sectors in developing countries (Nations, 2015). Thus, in a power plant, inspections are regular and entail planned checks of components or the whole plant to avoid interruptions in operation due to failure of components or systems. When carried out at regular intervals, they permit wear to be detected, pending failure to be recognised in good time and faulty parts to be replaced before they fail altogether (Kumar, 2021). Availability is, however, not only determined by interruptions in operation but also by planned shutdowns. These shutdowns are therefore kept within economically tolerable limits and permit optimal results to be obtained from inspections. To fulfil these requirements in the power plant sector, a thorough comprehension of materials as well as their behaviour in a typical operating environment is key to enabling and aiding capabilities in component life assessment, which is crucial as this impacts plant availability (Scheepers, 2014).

Fatigue damage is among the major issues in engineering failures because it increases with the number of applied loading cycles in a cumulative manner and can lead to fracture and failure of the considered part (Santecchia, 2016). This damage mechanism manifests in a cumulative process, which may or may not result in a failure. Fatigue progresses through three stages (Kamaya, 2015). The first is called the crack nucleation stage. All materials have tiny defects that are virtually undetectable by inspection. These defects could be in any form, shape or size. During the operation of any material, after a series of cycles of stress application, the defect may develop into a tiny crack. The second stage of the fatigue process is the crack propagation stage. At each stress cycle, stress is concentrated at the crack tip. The material will undergo localized yielding, and the crack will slightly enlarge. At each subsequent loading cycle, the crack will be slightly larger than in the previous cycle, resulting in a greater amount of stress concentration. As the crack grows, the cross section available to carry the load decreases as well. It is important to note

that the tip of crack can experience plastic deformation as it expands, even if the calculated stress in the overall part is well below the yield strength. It is the concentrated stress at the crack tip that governs whether or not the crack will advance. An important point to note is that crack propagation is not inevitable and will not occur if the stress in the material is low enough. Eventually, a crack may become so large that the overall stress in the part will exceed the fracture strength of the material, and the part will experience the third stage of fatigue, which is sudden fracture. There may be no outward sign of an impending failure before it is too late, since the cracks typically progress internally, and if they appear on the outer surface at all, it may only be as nearly invisible hairline cracks.

Cyclic loading of inelastic stress to a metal can cause continuous changes until cyclic stability is reached. This means that the material becomes either more or less resistant to the applied stress, implying that the material softens or hardens (Hertzberg, 1967). The reason for the hardening or softening of the material is related to the density and arrangement of the dislocation structure and substructure of the metal. . When dislocations advance along crystallographic planes in metals within individual grains, slip takes place. For materials that start of as hard or have been hardened, inelastic strain cycling is caused by the existing dislocation structure to rearrange into a configuration such that there is less resistance to deformation. This is prone to promotes more dislocation movement. Therefore, the material softens and the cyclic yield strength is less than the monotonic yield strength. Likewise, for materials that start off as soft, there is low dislocation density. Due to stress or strain cycling, inelastic deformation occurs, and the density of dislocations increases quickly. This leads to a decrease in dislocation mobility. Thus, the material cyclic hardens and the cyclic yield strength becomes considerable than the monotonic yield strength (Stephens, 2001).

The typical stages of fatigue that occur in a material are shown in

	Fracture		Cracks visible with naked eye	Fatigue crack initiation
	Non-propagating crack		Cracks visible with dye pen	Final fracture
	Very fine cracks		Visible growth and connections	

Figure 1 depending on the stress level applied. In general, slip occurs first, followed by fine cracks that can be seen only at high magnification. These cracks continue to grow under cycling loading

and eventually become visible to the unaided eye. The cracks tend to combine such that just a few major cracks grow. When these cracks reach a critical size, a sudden fracture occurs. The higher the stress magnitude, the sooner all processes occur. Cracks may also stop without further growth as a result of compressive residual stress fields or as a crack grows out of a high stress region such as a notch. Depending on the material and the stage of the fatigue process, crack growth can be proceeded by a number of mechanisms such as striation formation, micro void coalescence and cleavage formation which can be viewed under magnification (Stephens, 2001). Surface features include characteristics such as rachet marks, beach marks and river patterns.

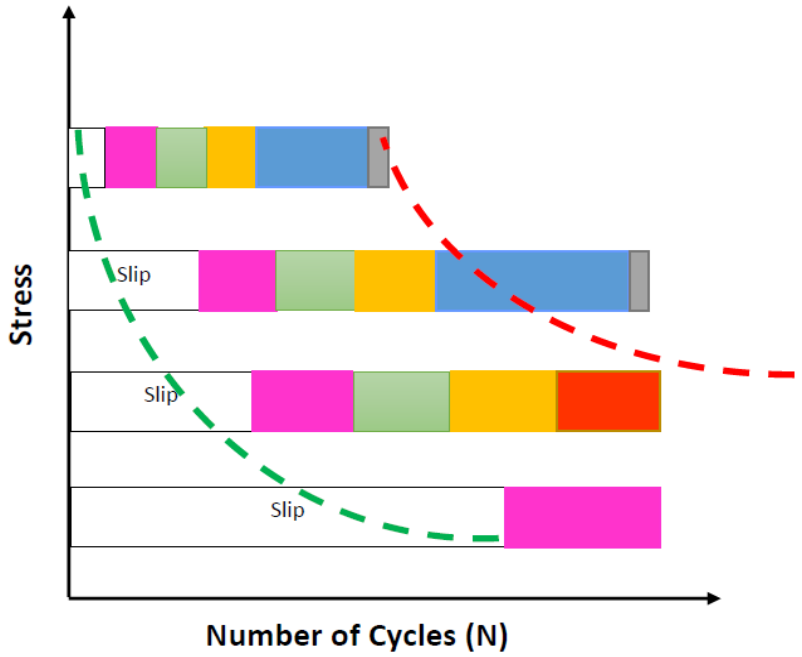

LEGEND

	Fracture		Cracks visible with naked eye	Fatigue crack initiation	
	Non-propagating crack		Cracks visible with dye pen	Final fracture	
	Very fine cracks		Visible growth and connections		

Figure 1: S-N Curve for typical material showing material microstructure evolution during fatigue testing at different stress levels. (Stephens, 2001).

The evolution of dislocation density in steels is an important aspect of the mechanical response. It could potentially be used as a fingerprint to relate the material state to the life-consumption fraction in materials subject to either creep and/or fatigue conditions. Methodologies exist for the evaluation of the full component life such as the S-N approaches, strain-life and stress-life models and Fracture Mechanics based fatigue methods (Binyan, 2013). The S-N approach is a global method used to characterise fatigue performance based on experimental results directly relating the stress range, $\Delta\sigma$, with total number of cycles to failure, N. An S-N curve was developed by a German scientist August Wöhler because of an investigation of a train crash in 1842 where the axle of the train locomotive failed under repeated low level cycle stress of everyday use on the railroad (Hertzberg, 1967). This curve is a plot of the magnitude of an alternating stress versus the number of cycles to failure for a given material. Typically, both the stress and number of cycles are displayed on logarithmic scales. These methods are often correlated with other developed techniques including numerous destructive, non-destructive and mathematical models that reasonably guarantee the extent of current damage in materials as well as the remnant lifetime assessment.

Even if the mechanisms developed in the early stages of fatigue have been established such as the addition of dislocations, establishment of slip bands, extrusions, intrusions, and microcracks, it is not always clear which microstructural changes, and to what degree, can be associated with fatigue damage (Haghshenans, 2018). Since damage evolution, at least at the onset of fatigue, is concerned with the movement, multiplication and rearrangement of dislocations, changes need to be detected at the microscopic scale. Dislocation density can be measured by numerous methods which are direct and indirect as well as a combination of the two (Garcia-Mateo, 2016). Direct methods provide an image of the dislocations in the structure such as transmission electron microscopy (TEM) and scanning electron microscopy (SEM). Also, there are optical methods that image etch pits on the surface which can be useful. While indirect methods, such as PXRD make some kind of X-Ray pattern, or hardness measurement and then extract information regarding the dislocation density indirectly from the sample. Electron Backscattered Diffraction (EBSD) is a combination of the two methods since the dislocation information is extracted from the orientation measurement indirectly, it can create maps of dislocations that agree with dislocation domain walls, hence outlining the dislocation structure directly. These experimental methods are complementary in the sense that the direct methods can reveal the

microstructural information in an extremely small area of the sample, whereas the indirect methods can reveal average data over a relatively large area exposed to irradiation.

The quantification of dislocation density via the PXRD method relies on this broadening of diffraction peaks that occurs when atoms in a crystal lattice are displaced from their ideal position due to the size and shape of the unit cell as a result of the abundance of lattice defects such as dislocations. The evaluation of dislocation density and the crystallite size using an analytical method for best fitting diffraction peaks is performed by measuring the normalised area under a peak or Full Width at Half Maximum (FWHM) using the Williamson–Hall (WH) approach to determine the dislocation density in polycrystalline materials (Borbely, 2022). This situation raises the question that if dislocation density can be correlated with the degree of fatigue damage, can the deployment of the non-destructive PXRD technique be used to monitor fatigue damage development in critical components? Whilst this is a highly relevant research question, it is understood that high strength power plants steels in general have very complex microstructures with inherent high dislocation densities arising from controlled quench and temper heat treatments. Dislocation density is a measure of the number of dislocations in a unit volume of a crystalline material. Consequently, in order to evaluate the baseline sensitivity of the PXRD technique to measure changing dislocation density (i.e., accumulated strain), the damage accumulation by fatigue must be separated from the inherent defects and microstructural features in power plant steels (Fiala, 2009). To do this, the situation can be simplified by selecting an ideal single phase polycrystalline microstructure that possesses very low dislocation density in the undeformed state.

1.2 Hypothesis

The hypothesis for this research is therefore:

“X-ray diffraction can be used to track the damage accumulation in a single-phase polycrystalline metal alloy as a function of the number of oscillating stress cycles.”

1.3 Research Questions

A number of research questions arise out of the hypothesis stated in 1.2:

a) How can a metal alloy such as AISI316L austenitic stainless steel serve as a model single phase polycrystalline alloy to attempt to track fatigue damage accumulation?
b) What is the influence of cyclic fatigue on the microstructure of AISI 316L?

c) What is the measurement and analysis protocol that must be followed for accurate micro-strain (deformation) measurement using PXRD?
d) How does the assessment of fatigue damage using microscopy techniques such as transmission electron microscopy (TEM) and scanning electron microscopy (SEM) based orientation imaging (using electron backscattered diffraction) correlate with PXRD strain measurements?
e) Is the PXRD measurement technique sufficiently sensitive to detect different levels of fatigue damage relative to the number of oscillating stress cycles?
f) What is the potential in using PXRD analysis as a technique in determining fatigue damage in turbine blade material such as X20Cr13?

1.4 Purpose and scope

The overall purpose of this study is to contribute towards the development and application of a non-destructive technique by assessing the fatigue initiation life in AISI 316L stainless steel that can be applied in a plant engineering environment for the purposes of quantifying the remaining life in an industrial turbine material by using X-Ray diffraction (PXRD). The scope will entail an understanding of the limitation and processing involved in the quantification of micro-strain in the material after subjecting it to a series of fatigue tests in comparison with the established methods. It is envisaged that the study will provide a baseline for the development of the PXRD inspection technique in evaluating the remaining life of low-pressure steam turbine last stage blades after known cycles of operation by investigating the viability of the technique to determine dislocation density.

The scope of the work includes an experimental set up of the fatigue testing, the characterization of the microstructure using various electron microscopy tools and the analysis of the results using a number of qualitative tools. Further, care is taken to standardise the sample preparation, instrument calibration, and data processing pipeline for reliable measurements.

1.5 Objectives

The specific objectives of this study are as follows:

- Design suitable fatigue test specimen geometry and fatigue testing method for developing controlled strain accumulation in a model alloy.

- Determine the fatigue limit diagram (S-N curve) to use as a guide for selecting appropriate fatigue damage levels.
- Perform PXRD standard analysis to calibrate machine sensitivity for actual PXRD data capture and interpretation.
- Rigorous analysis of PXRD data to assess micro-strain accumulation.
- Measurement of dislocation density at different levels of fatigue damage using direct TEM imaging.
- Evaluation of misorientation (fatigue damage) as function of different levels of fatigue damage using SEM orientation imaging.
- Correlate damage assessment from PXRD, TEM and SEM orientation imaging analysis.

1.6 Dissertation Overview

Chapter two begins by discussing the history of the inspection philosophy used in industry to assess component degradation. The chapter further expands into the literature available on the inspection techniques used in line with the study with the aim of selecting the viable technique for the proposed application in this study.

Chapter three describes the experimental setup of the fatigue specimen for the stress-controlled testing in an Instron equipment. The machine is a fully integrated dynamic and fatigue testing systems incorporating servo hydraulic, servo-electric and linear motor technologies for the purposes of performing a broad range of fatigue, dynamic, and static testing applications. The laboratory set-up and specimen preparation are investigated and detailed. This is done by characterising the chosen material by performing mechanical testing and understanding the chemical composition of the material. The test conditions to achieve the desired outcome are also finalised and documented. Next, a number of specimens are then tested at different stress levels until the point of fracture. This information is then used to draw an S-N curve of the material as a custom property. Finally, the fractured specimens are also evaluated using microscopy to further characterise the damage mechanism of the samples. The S-N curve provides the limits of evaluation for the amount of fatigue to be induced on different specimen prior to the onset of failure. This is explored further in the next chapter.

Chapter four entails the PXRD testing of the various unfractured specimen that have been tested to varying cycles at approximately the same stress levels. Thereafter, the results from the data are modelled using the WH plot to determine where the peak broadening occurs. At the different

2θ angles of peak broadening, the instrumental broadening is subtracted to achieve the actual broadening that the specimen has experienced as a result of the deformation experienced during fatigue testing. The chapter concludes by determining if there is a direct relationship between the level of fatigue in the specimen in comparison to the amount of strain that is achieved because of peak broadening.

Chapter five entails the quantitative dislocation density analysis using electron backscattering diffraction (EBSD) grain misorientation techniques for the same specimen category as discussed in chapter three. Analysis is done by evaluating the varying amount of deformation along the specimen grain boundaries through the visualisation of the grain misorientations angles and assigning the deviations to specific uniform colours. This analysis is done in *MATLAB* (Matrix Laboratory) using the open-source crystallographic toolbox *MTEX (MATLAB Texture Toolbox)*.

Chapter six discusses Transmission Electron Microscopy (TEM) conducted as part of the study. A semi-qualitative manner is utilised for the evaluation of dislocation density on specimen micrographs using visual analysis of dislocation counting. Thereafter, the results of the calculated dislocations are statistically analysed using the t-test method to evaluate if there are any significant differences between the different samples. The results and conclusions are then made.

The penultimate chapter (Chapter 7) is a write up that summarises the findings from the test and results shown by PXRD, EBSD and TEM and compares each microscopic application in line with its advantages and limitations based on the boundaries of the study. With the aim of drawing conclusions as discussed in chapter eight. The latter also provides recommendations for possible future work.

Chapter 2. Literature review

2.1 Component microstructural damage analysis – A historical overview

In actual operating conditions, materials that make up components/equipment are subjected to degradation of mechanical properties which from time to time will require an assessment of the remaining lifetime of components and structures (Rezaei, 2017). This assessment is commonly based on correlated procedures including several destructive, non-destructive, and mathematical techniques that give the equipment operator rational and accurate assurance of the extent of the operational damage of the materials in question as well as the remnant lifetime assessment (Endrenyi, 2001).

Equipment life can be shortened due to several damage mechanisms including fretting, cyclic fatigue or stress corrosion that result in the observation of cracks during material analysis and testing. In steam turbine plant blade design, crack initiation, location and propagation orientation can vary with blade design configuration. The damage mechanisms are consistent with highly stressed areas usually modelled by finite element analysis (FEA) amongst other techniques (Plesiutschnig, 2016). Once cracking has been observed, a risk based approached is adopted since in certain cases this is an early warning for imminent failure. It is this approach that must be balanced with early replacement of blades which increase the utility's operating costs.

The low cycle fatigue damage of steam turbine last stage blades is strongly associated with the operating conditions of the power system (Booysen, 2015). This damage mechanism is usually considered during the steam turbine design. However, if these cyclical operating conditions continue compounded by the operation of steam turbine blades in the presence of other damage mechanism drivers such as a corrosive environment and beyond the design operating life, the cumulative long-term lifetime may require constant assessment to avoid probable catastrophic failures.

Non-destructive examination (NDE) is an important tool for ensuring the safety and performance of power plant systems because of its ability to detect and characterize flaws and damage at an early stage and in a manner that does not affect the future usefulness of the component (EPRI, 2020). A variety of non-destructive testing methods are available, and there are also further

developments which are continuously explored in this field since each technique possesses unique capabilities and limitations. In the inspection of steam turbine last stage blades, the four common types of blade root inspection techniques are:

a) Ex-situ fluorescent Magnetic Particle Testing (MT) – This is a non-destructive test method for the detection of surface and sub-surface discontinuities in ferrous materials. The test method involves application of magnetic field externally or applying electric current through the material which in turn produces magnetic flux in the material.
b) Ex-situ fluorescent Penetrant Testing (PT) – This testing refers to the process of using a liquid to coat a material and then looking for breaks in the liquid to identify imperfections in the material.
c) Ex-situ Eddy Current Testing (ET) - Eddy Current Non-Destructive Testing is a type of electromagnetic testing that uses measurements of the strength of electrical currents (also called eddy currents) in a magnetic field surrounding a material in order to make determinations about the material, which may include the locations of defects.
d) In-situ Phased Array Ultrasonic Testing (PAUT) – this is an advanced non-destructive inspection technique that uses a set of ultrasonic testing (UT) probes made up of numerous small elements. Each of these is pulsed individually with computer-calculated timing to create the phased aspect of the process, while the array refers to the multiple elements that make up a PAUT system.

In most cases, an in-situ phase array inspection is executed first and when defects are found the subsequent de-blading of rotors enables the use of ex-situ techniques (fluorescent MT/PT and ET) is executed and provides evidence to support the intended detection threshold of PAUT and assumed detection threshold of MT and PT. The PAUT technique is limited on the size of defect that can be found or missed, typically 5mm long x 1mm deep. While fluorescent MT and PT would be capable of detecting >1-2mm long defects if applied carefully, provided surface condition of root is good. The detection limit of the florescent inspection has largely negated the need to develop the eddy current techniques which are more expensive based on the cost of high capital expenditure for array probes that require conformation to root grooves.

The execution of inspection techniques varies according to the capability of a flaw detection as well as the ease of use. However, none of the techniques involved guarantee a defect free component (i.e., blade). From industry applications, the MP/PT results are dependent on the technique application and specific competency of inspection personnel. While the ET technique

has been proven in an industrial study conducted by RWE (Rheinisch-Westfälische Elektrizitätswerk) power company to give the greatest confidence in finding small defects but requires blades to be removed from the rotor as similarly observed for the PT and MT technique. Where an in-situ inspection is desirable, a phased array inspection can give confidence that cracks above a certain size are not present.

X-ray diffraction (PXRD) is a non-destructive technique that can be used to quantify fatigue initiation damage (pre-crack damage) and to optimise turbine blade life (Binyan, 2013). The assessment of the remaining lifetime by X-ray diffraction technique is executed by line peak broadening which is caused by deviation from the ideal crystalline lattice. Many factors may contribute to the observed peak profile such as the instruments contribution to the observed peak profile, crystallite size, micro strain, solid solution inhomogeneity and temperature factors (Speakman, 2014). The peak profile is a convolution of the profiles from all these contributions. The microstructural characteristics of deformation-processed materials highly influence their mechanical properties (Vincentis, 2017)

2.2 Determining a suitable material and fatigue characterization

In 1884 the LP blade material comprised of materials such as cartridge brass (72 Cu, 28 Zn), nickel brass (50 Cu, 10 Ni, 40 Zn), and Monel (typically 66 Ni, 31 Cu, 1.3 Fe); when larger steam turbines were manufactured in the 1920s, 5% Ni steel was then routinely used. Thereafter, most LP turbine blades were manufactured from a 12% Cr stainless steel, designated as blading alloy X20Cr13 in Europe (Mccloskey, 1999).

X20Cr13 is a martensitic stainless steel, equivalent to AISI 420 and widely used blade manufacturing material due to its mitigation properties against the fatigue crack damage mechanism (Shojaati, 2020). Its chemical composition consists of 0.18%C, 0.39%Si, 0.56%Mn, 13.73%Cr, 0.711%Ni, 0.015Mo, 0.024%Cu and 0.019%Nb. A martensitic stainless steel is a type of stainless-steel alloy that has a very hard form of steel crystalline structure achieved by the process of hardening and tempering through aging and heat treatment (Peckner, 1977). The microstructure is developed by quenching the austenite form of iron at a rapid rate such that carbon atoms do not have time to diffuse out the crystal structure in large enough quantities (Fe_3C).

As a result of the quenching, the face-centred cubic (FCC) austenite transforms to a highly strained body-centred tetragonal form called martensite. The shear deformations that result produce dislocations, which is a primary strengthening mechanism of steels (Schwenk, 2014). When the martensitic reaction begins during fast cooling, the austenite reaches the martensite start temperature, and the parent austenite becomes mechanically unstable. The process produces dislocation densities up to $10^{13}/cm^2$. This process results in a thermally induced or stress induced martensite (L.C.F. Canale, 2014). Thus, martensite is generally not an equilibrium phase. For steel with 0–0.6% carbon, the martensite has the appearance of lath and is called lath martensite. For steel with greater than 1% carbon, it will form a plate-like structure called plate martensite. Between those two percentages, the physical appearance of the martensitic morphology is a mix of the two. Shojaati et al, investigated the evolution of the dislocation densities in martensite and in austenite during the quench of a low-carbon (0.215 wt% C) steel by means of a High Energy X-Ray Diffraction experiment on a synchrotron beamline and revealed that the mean density of dislocations in martensite increases as the transformation proceeds, confirming that dislocations are not homogeneously distributed between the laths. This is due to the size, the dislocation structure, the segregations, the residual stresses and thus the local strength of these laths at room temperature should strongly depend on their respective transformation temperatures.

Evidence showed that the higher the martensite phase fraction, the higher the mean dislocation densities in both phases (Christein, 2013). As mentioned in the paragraph above designing martensitic transformation; the process leads to the crystallographic transformation of face centred cubic (FCC) austenite into body centred cubic (BCC) martensite. During the transformation, the carbon atoms that are randomly distributed on the interstitial sites in FCC do not have time to migrate to the BCC in a random manner and hence move in a coordinated motion. This increases the tetragonality of the BCC lattice and thus the carbon containing martensite is of body centred tetragonal (BCT) structure. The tetragonality of martensite increases with increasing carbon content (Yeddu, 2012). In the study by Macchi, 2021, it is concluded that at the beginning of the martensite transformation, pre-existing body-centred cubic (BCC) phase shows already a high density of dislocations (2×10^{14} m/m^3) and during the first 20% of the martensitic transformation (mainly occurring below 365 °C), the dislocation density increases drastically to reach a value close to 9×10^{14} m/m^3 (Juan Macchi, 2021). During the rest of the transformation, down to room temperature, the density of dislocations continues to increase but at an apparent lower rate, to reach a final value of 2×10^{15} m/m^3.

The increase in the mean dislocation density in martensite during the transformation can be interpreted either by the fact that already formed laths undergo plastic deformation or by the fact that new laths present a higher dislocation density than the previous ones. Consequently, we assume that the increase in the mean dislocation density in martensite is due the progressive nucleation of new laths containing more dislocations than the previous ones. The quantification of blade material damage is thus reliant on the initial material state and the evaluation of changes throughout the operation of the component. However, the phase transformation encountered during the manufacture of a martensitic steel results in high initial dislocation component where baseline fatigue damage levels may give a distorted outcome for the determination of remaining life.

To effectively perform this study, a deviation from a normal blade material to a stable material will be required to form an adequate baseline of the dislocation density at a specified material state. The chosen material for this study is AISI 316L which is an austenitic stainless steel (ASS) alloy with a face-centred cubic crystalline structure. This material is also successfully used in the power generation industry. During manufacture, the final heat treatment applied to austenitic stainless steels before usage, is solution annealing. After solution annealing, the austenitic stainless-steel microstructure is constituted of insoluble particles or partially insoluble ones, dispersed in a solid solution that has a low stacking fault energy (SFE) that, in the case of wrought alloys, presents several annealing twins. SFE plays a very important role in the deformation substructure, i.e., in the nature, density and distribution of lattice defects and tendency towards martensite formation. In general, a lower SFE makes dislocation cross-slip more difficult, resulting in less dislocation mobility. This will favour more homogeneous dislocation distribution with less tendency towards the formation of dislocation cells. In its annealed state, the microstructure has little, or no dislocations present.

During the cold working process, there is extensive dislocation multiplication coupled with the formation of stacking faults, stacking faults bundles or faulted ε-martensite, deformation twins, deformation bands and α′ martensite may be formed. These are deformation mechanisms that form on crystallite surface structures. Stacking faults are crystallographic defects in which the proper order of stacking plans is interrupted. Similar to stacking faults formation, stacking fault bundles refers to bundles of intrinsic stacking faults forming and aggregating randomly to form thicker bundles (Koyama, 2021). The faulted ε-martensite and α′ martensite are fault bands that form during martensitic transformation (Xi, 2022). While a deformation twin has an atomic arrangement that is the mirror image of the parent crystal. During annealing, the cold worked

ASSs undergoes a martensite reversion process dependent on the annealing temperature that tends to transform the α′ martensite to austenite. Also, the steel tends to undergo recrystallization which occurs at temperatures about 100°C higher than the martensite reversion temperature and begins on deformation bands and in the vicinity of grain boundaries.

Pham et al 2013, highlighted the importance of developing a comprehensive relationship between internal stresses and the development of dislocation densities and dislocation microstructures during cyclic loading progress from an as-received condition, where there is no presence of dislocation walls and channels to a condition of a well-organised dislocation structures. This is largely because plastic deformation over a very wide range of loading conditions is driven by the movement of dislocations (Argon, 2007)

Considerable changes in the cyclic response of many polycrystalline materials are observed during early loading cycles (Feltner, 1967). Moreover, for cyclic loading of polycrystalline materials, deformation behaviour evolves differently to that for monotonic loading (Sauzay, 2011). The microstructural heterogeneities, which are either present before loading or formed during loading, possess different strengths with respect to loading direction, resulting in inhomogeneous deformation. Inhomogeneous plastic deformation is inherently present between grains and is the main constituent of plastic strain incompatibility for single phase polycrystalline materials. This grain-to-grain inhomogeneous plastic deformation is responsible for inter-granular back stress.

One of the most distinguishing features of crack initiation is that cracks are not initiated from all the grains and grain boundaries, but from only selected ones. Further, in a polycrystalline material, stress and strain are distributed inhomogeneously in the material volume at the microstructural level even under uniform cyclic testing conditions. Even if the damage induced in the material is uniform macroscopically, its spatial distribution is not homogeneous at the microscopic scale. Anisotropy of deformation properties of crystal grains and the random nature of the crystal orientation in polycrystalline material cause the inhomogeneity (Kamaya, 2012, Singh, 2001).

2.3 Damage development in polycrystalline metals during cyclic loading

For a fatigue crack to propagate, the stresses in the material must be sufficient, cyclic, and tensile. This means that the localized stress increases to a high tension, decreases, and increases again repeatedly. This could be due to a load of varying intensity, or even a load of constant magnitude but varying direction. Any source of sufficient stress can cause crack propagation, whether it is due to applied forces, pressures, impacts, transmitted vibration, thermal expansion, resistive heating from carrying electrical currents, etc. The stress can be applied in pure tension, bending, torsion, or in a combined load state.

To perform a proper fatigue characterization of a material for a given application, it is necessary to obtain data in a test whose loading mimics the expected cyclical loading that will be experienced by the material in the application. This means that if the part, specimen or component will experience cyclical uniaxial tension, then the test data should be generated in uniaxial tension. For expected bending or torsional stresses, the test data should be generated in bending or torsion, respectively. Unlike tensile testing, which can be routinely done on all production material, fatigue testing is a time-consuming test as testing can only be done on representative sample depicting the actual condition to be studied. (Gedeon, 2013) proposed that the starting point is the determination of the stress ratio for the test. This is depicted by Equation 1 and is the minimum stress (min stress (σ_{min})) experienced during a cycle divided by the maximum stress (max stress (σ_{max})) experienced during a cycle. For an example, a unidirectional where the ratio, R=0; the test scenario involves an unloaded specimen (i.e., zero stress) that is gradually loaded to the required maximum positive stress level, and thereafter unloaded to start the next cycle; the R ratio would be exactly zero. Also, depending on the cycling stress to be modelled, a ratio of R = -1 for a fully reversed test can also be proposed where the loading of the specimen at a specific stress level including an equal reverse level loading in the opposite direction is performed. This is considered, the most extreme case where the minimum stress would be the negative of the maximum stress. Figure 2 shows an example of a stress ratio R = 0.5. The min and max stress values need to be initially determined based on the material characteristics and the desired loading profile. The stress can be either tensile (positive) or compressive (negative). Equation 2 to serve to satisfy the stress range. The stress amplitude is the difference between the peak stress and the mean stress and is shown in Equation 3. It is also known as the alternating stress. Loading in a cyclical manner can be visualised as a fully reversed

alternating stress superimposed on a constant mean stress level. The mean stress is shown in Equation 4 and is defined as the arithmetic mean of the maximum stress and the minimum stress.

Stress Ratio	$R = \frac{\sigma_{min}}{\sigma_{max}}$	Equation 1
Stress Range	$\Delta\sigma = \sigma_{max} - \sigma_{min}$	Equation 2
Stress Amplitude	$\sigma_a = \frac{\sigma_{max} - \sigma_{min}}{2}$	Equation 3
Mean Stress	$\sigma_m = \frac{\sigma_{max} + \sigma_{min}}{2}$	Equation 4

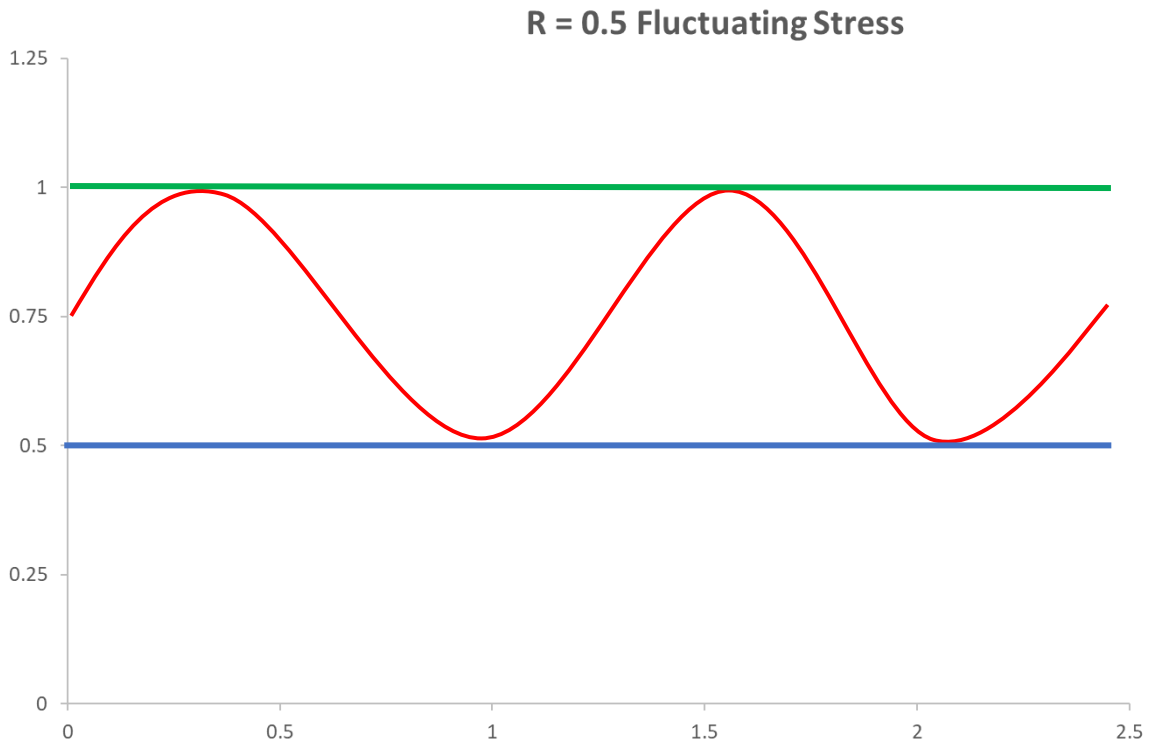

Figure 2: Example of fatigue test stress profile with a ratio of 0.5.

To completely characterize the fatigue behaviour, fatigue testing involves a minimum of 3 samples at each stress level of interest to obtain statistically meaningful data. The test results are plotted on an S-N curve which shows the number of cycles achieved per test specimen dependant on the testing stress level. If the sample does not fail after 10^8 (100 million) cycles, the tests are typically stopped, and the result is designated as a runout (Gedeon, 2013). Low cycle fatigue occurs below 10 000 cycles. In this region, the stresses are well below the yield strength of the material and there is usually a large amount of variation in the data, so there is no plastic deformation anywhere other than the tip of the fatigue crack. At cycles above 10 000, the stresses are below the yield strength of the material and no plastic deformation is evident anywhere other than the tip of the fatigue crack. A best fit trend line can be plotted through the centre of the scattered points to provide an estimate of when about half of your parts would be expected to fail.

2.4 Microstructure Characterization using microscopy analysis.

This section discusses some of the most relevant techniques used to measure dislocations in solid- compounds. The methods are based on the feature size that can be resolved depending on the magnitude of observation as seen in Figure 3.

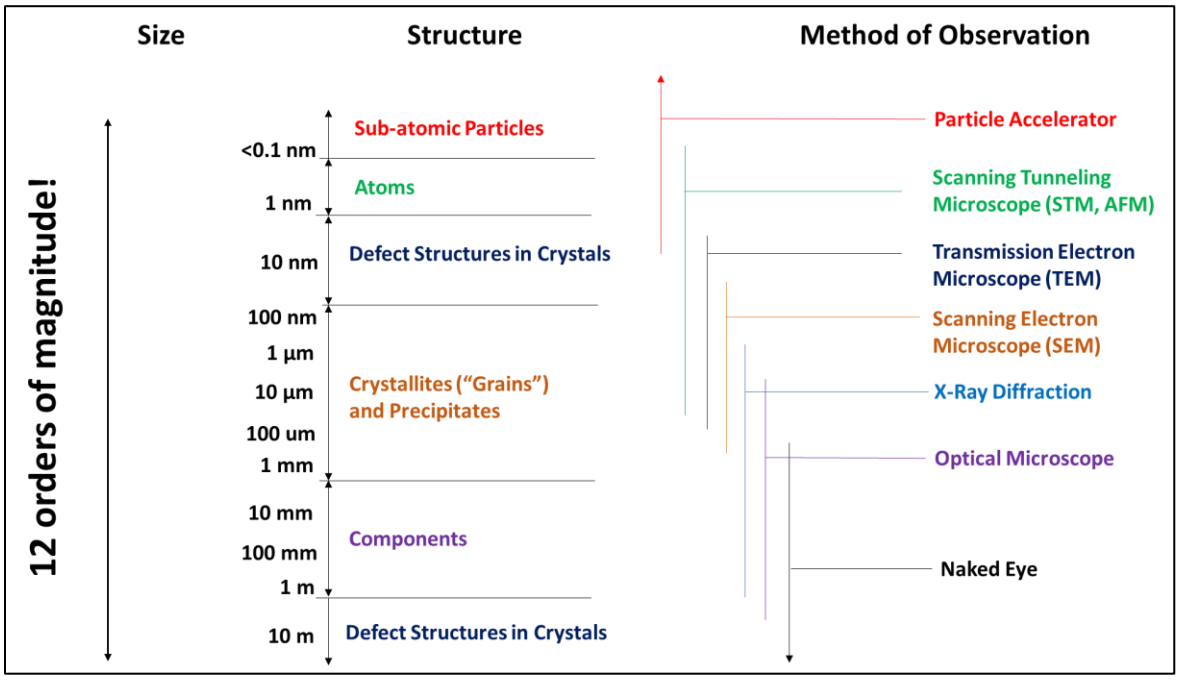

Figure 3: Diagram showing the electromagnetic spectrum with 12 orders of magnitude and possible method of observation for object side. Source: (Banerjee, 2007)

Since electrons are smaller than atoms, they were considered to resolve images better with an aim of understanding material properties. Electron diffraction is a useful tool for materials scientists and nanotechnologists for whom crystal structure (and particularly crystal defects) is an essential characteristic when it comes to controlling properties. When an incident beam hits a thin specimen as shown in Figure 4, a wide range of secondary signals are produced from the specimen. The signals can be used for analysis in electron microscopy. One of the resulting signals is characteristic X-Rays which is high-energy electromagnetic radiation with energies ranging from about 200 eV to 1 MeV; which puts them between x-rays and ultraviolet (UV) radiation in the electromagnetic spectrum in terms of energy.

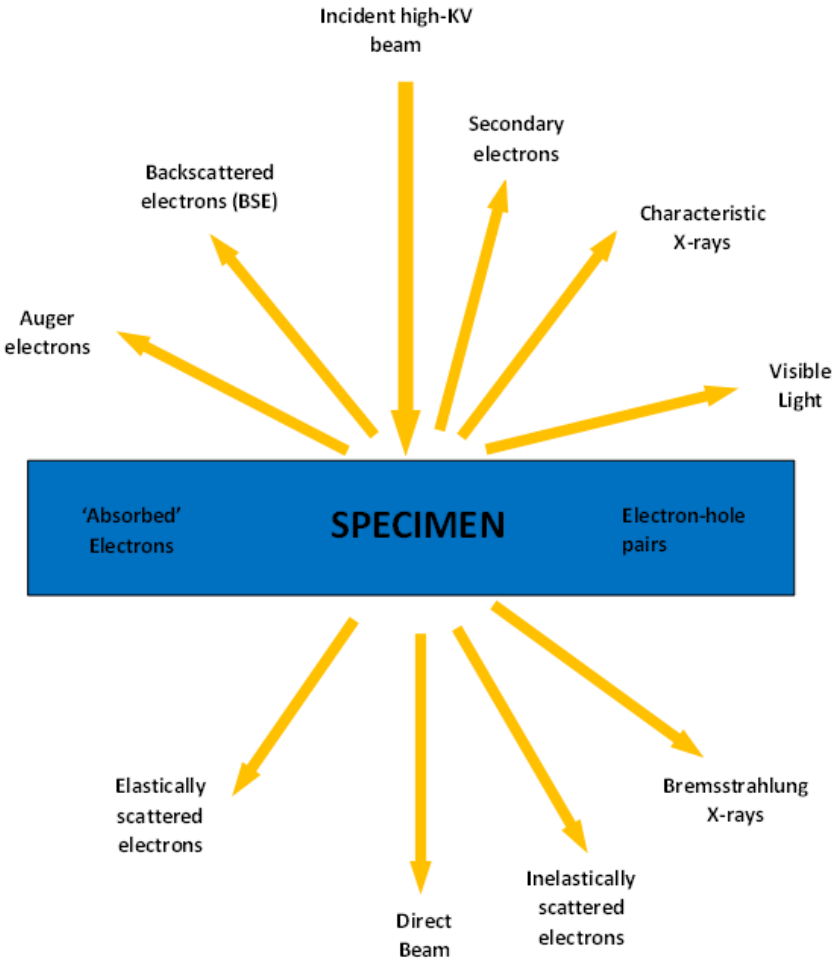

Figure 4: Signals generated when a high-energy beam of electrons interacts with a thin specimen. The directions shown for each signal do not always represent the physical direction of the signal, but indicate, in a relative manner, where the signal is strongest or where it is detected.

One of the most significant and practical applications of the study of diffraction is the evaluation of the resolving power of optical instruments, specifically in microscopes. Resolving power refers to the ability to distinguish between small angular separations, such as small distances between objects in a microscope. The following section discusses some of the available characterization techniques that can be used to analyse structural defects based on the principle of diffraction. These methods are mainly divided into two categories, namely bulk and surface characterization, based on the order of magnitude of resolving a defect. The diffraction theory is expanded upon in all techniques, and the section also explores the experimental techniques of each technique and their suitability in the current study.

2.4.1 Bulk characterization techniques

There are multiple techniques available for bulk characterization of materials. The selection of a particular technique depends on the desired analysis and results required. The selection of a bulk characterization technique is also dependent on its advantages and limitations. The paragraphs below describe some of the available techniques with outcomes that are in line with the objective of this study for the purposes of a fair analysis.

In the study by Xu Z, 2018, Raman spectroscopy was utilized to quantitatively determine the residual stress and the thickness of the subsurface damage layer of semiconductor materials by analysing the Raman band position shift and Raman intensity ratio. This technique has been applied in various fields of science, such as chemical industry, bio-sensing, archaeology, and material science, for various types of applications (Fernandez-Galiana A. 2023; Lohumi S. 2019 and Qin J. 2017). The technology is a light scattering technique often used as a non-destructive chemical analysis technique which provides detailed information about chemical structure, phase and polymorphy, crystallinity and molecular interactions and can be used to characterise defects (Dutta, 2013). The principle of the Raman effect is based on the inelastic light-scattering process between the incident light and the irradiated substance (Miedema, 2017). During this process, the incident light interacts with molecules and distorts the electron cloud to form a 'virtual level'. Since this 'virtual level' is not stable, the photons are scattered immediately to another state that is relatively stable. During Raman spectroscopy characterization, a Raman spectroscopy instrument collects Raman scattered light from the tested sample and generates a corresponding Raman spectrum that contains information on the molecular vibrations and crystal structure of the material (Gardiner, 1989). The spatial resolution of the technique is less than 1 µm, making it an important tool for studying local stress (Vogel, 2013). It has been widely

used to detect and quantify residual stress by analysing the shift in Raman band positions (Xu Z., 2018). Raman microscopy is a powerful technique for characterizing defects and subsurface damage, but it has limitations in its application, such as the difficulty in measuring weak Raman scattering signals at low damage levels.

X-ray imaging is another technique that has significantly advanced, becoming more powerful, precise, and computer-driven (Ou, 2021). It can be categorized into two main components: the generation of X-rays and the methods used to capture and produce X-ray images. The technique enhances the ability to detect subtle defects in materials, especially soft tissues and low-density materials using high-resolution X-ray phase-contrast imaging. These defects would otherwise be invisible using traditional absorption-based X-ray techniques. The technique has been widely applied in NDT for various applications, including biomedical research, materials science, and industrial inspections. High-speed imaging and advanced data reconstruction methods enhance the capabilities of X-ray technology. X-ray imaging is also a reliable tool for material characterization and NDT (Hanke, 2008).

This section of the literature review would not be complete without the inclusion of the Synchrotron radiation. This is a type of electromagnetic radiation that is emitted when charged particles, such as electrons, move at nearly the speed of light through magnetic fields. This radiation occurs in synchrotron accelerators, where particles are accelerated to high speeds and forced to travel in circular or spiral paths by strong magnetic fields. The resulting radiation is highly intense, bright, and spans a broad spectrum, ranging from infrared to X-rays. Synchrotron radiation is commonly used in various fields such as materials science, chemistry, biology, and physics for techniques like X-ray diffraction, spectroscopy, and imaging due to its high brightness, tunability, and ability to provide detailed information about the atomic and molecular structure of materials (Ren Y, 2017; Song Z, 2022; Catlow, 2017). Synchrotron radiation has significantly advanced the analysis and development of materials used in power utilities. In the study by Catlow, XRD was used to track phase changes in the material as it was exposed to high-temperature cycling suing the application of synchrotron radiation in the study of metal alloys used in power plants, such as steels, superalloys, and other critical components. These materials are exposed to extreme conditions of temperature, pressure, and mechanical stress. Synchrotron X-ray diffraction was used to examine phase transitions, stress-strain behaviours, and microstructural evolutions in these materials during operation. This is important for improving the reliability and lifespan of components like turbine blades, heat exchangers, and boiler tubes. The results provided insights into improving the alloy's resistance to high-temperature fatigue.

The article concludes with a discussion on the future directions of synchrotron radiation in materials science, particularly in power utilities. Challenges experienced included the need for more advanced synchrotron sources and the integration of different analytical techniques to provide a more comprehensive understanding of materials in operational environments. The potential to use synchrotron radiation for in situ studies, where real-time observations are made during the operation of power utility systems, is identified as a significant advancement

2.4.1.1 Single-crystal and polycrystalline X-ray diffraction

In relation to EBSD, PXRD is one of the most common bulk material characterization techniques that uses diffraction profile line shape (Mittemeijer E.T., 2004). The diffraction patterns contain information about imperfections in crystalline phases. These imperfections often reveal subtle details of the microstructural changes induced by fatigue. (Leoni, 2012). This information is necessary to perform an evaluation of the remaining lifetime due to crystallite size and orientation of constituents as critical factors in the resolution of the prediction of residual lifetime of the components (Pesicka, J., 2010; Brown M., 2022; Bahadu, A., 1999). Diffraction peaks are affected by changes in the microstructure of a material, peak intensity changes with the presence of sampling texturing. Peak repositioning can be observed if the material presents residual stresses and peak broadening can indicate the presence of defects (mainly dislocations) and grain size decrease (Cao, L., 2017; Vincentis 2017; Prevėy, 2003, Fitzpatrick, M.E., 2005). The diffraction pattern is affected by both the material itself and the characteristics of the instrument (Hammond, C., 2009; Suryanarayana, C., 1989).

2.4.1.1.1 Basics of PXRD

X-rays are generated in a cathode in an X-ray tube by heating a filament to produce electrons, which are then concentrated and directed toward the sample, where characteristic X-rays specific to the material are produced (Bunaciu, 2015). X-ray diffraction is carried out with an instrument called an X-ray diffractometer. It consists of three main elements such as the X-ray cathode tube, the sample holder and the X-ray detector (Connolly, 2007) as shown in Figure 5. As the atom scatter x-rays, numerous atoms are then consolidated, the scattered waves from all the atoms can collaborate. If the scattered waves are coherent, they work together in a constructive manner and produce diffracted beams in specific directions (Cullity, 2014). These directions are determined by the wavelength (λ) of the incoming radiation and the crystal structure of the sample. Bragg's law, formulated by W. L. Bragg in 1913, connects the wavelength

of the x-rays to the spacing of the atomic planes. The derivation of Bragg's law assumes that each plane of atoms partially reflects (mirrors) the incident wave (Chandrasekhar, 2000).

The interaction of the incident rays with the sample produces constructive interference (and a diffracted ray) when conditions satisfy Bragg's law as shown in Equation 5:

$$n\lambda = 2dsin\theta \qquad \text{Equation 5}$$

Where n is an integer, λ is the wavelength of the X-rays, d is the interplanar spacing generating the diffraction, and θ is the diffraction angle.

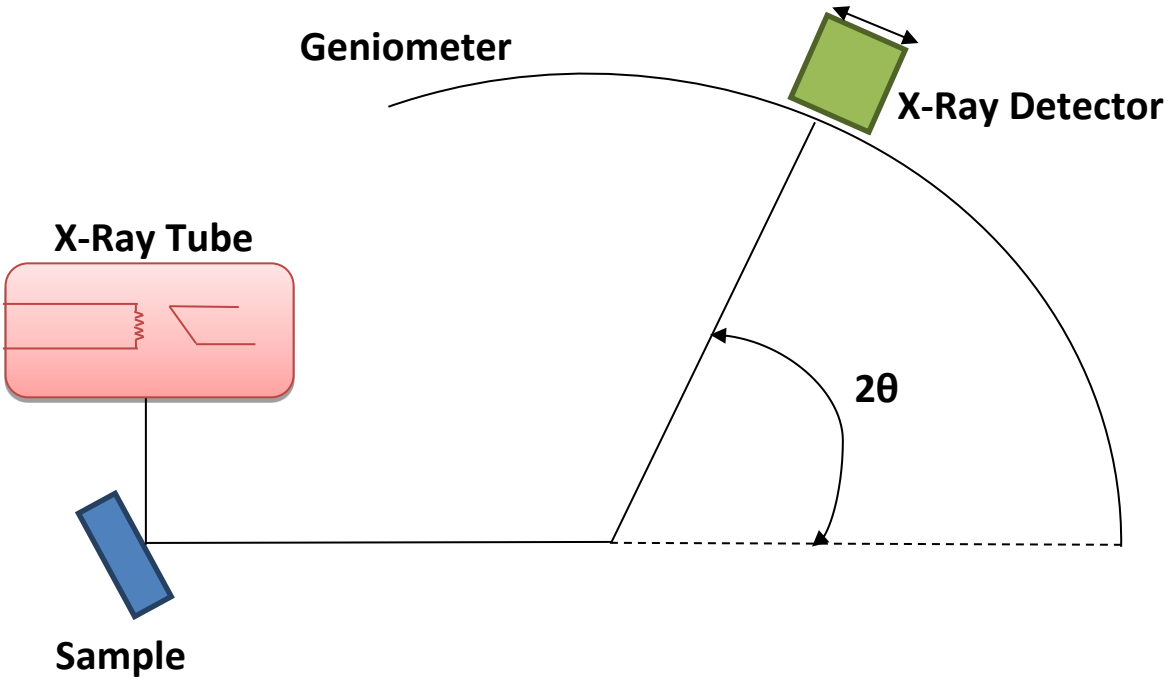

Figure 5: A schematic diagram illustrating the operation of a diffractometer system.

In a Bragg scattering geometry scheme as shown in Figure 6; when a collimated beam of X-rays strikes a pair of parallel lattice planes in a crystal, each atom acts as a scattering centre and emits a secondary wave, and a diffracted beam is produced as the secondary waves interfere with each other. The incident plane waves of X-rays are scattered from different planes with a path length difference of $2d_{hkl}sin(\theta)$, where 2θ is the angle between the incident and the exit wave (Ameh, 2019, Sardela, 2014). The only way to observe constructive interferences between the two

scattered spherical waves is when the path length difference is equal to a multiple of λ (Girard, 2020, Radamson, 2023). Every 2θ angle at which interference occurs is called a Bragg peak. However, Bragg's Law expressed in equation 5 only contains scalar information and nothing about directional components.

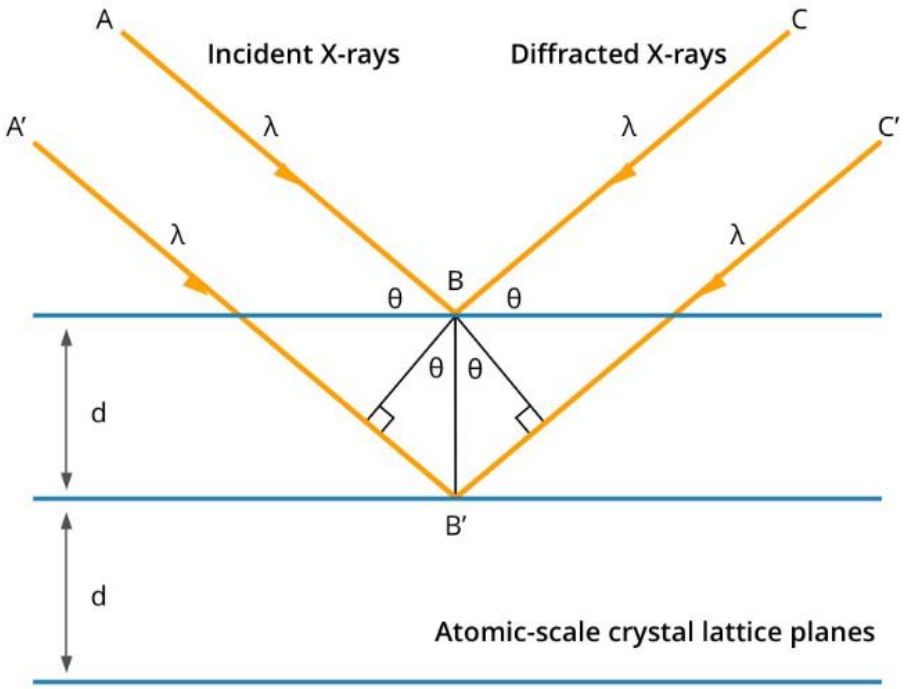

Figure 6: Image depicting Bragg Scattering Geometry for a symmetric diffraction experiment. Constructive interference between X-rays incident on a set of parallel (hkl) planes only occurs when the path length difference $2d_{hkl}\sin\theta$ is equal to the incident wavelength λ, see equation 5.

Source: (Bunaciua, 2015)

2.4.1.1.2 Diffraction pattern broadening

During the geometric movement of the goniometer, once the conditions for Bragg's law for the sample being analysed is satisfied, constructive interference occurs, causing a peak in intensity (Ali, 2022). The detector records and processes this signal, converting it into a count rate for output to a computer. The peak intensities are determined by the atomic positions within the lattice planes (Hart, 1981). Consequently, the PXRD pattern is the fingerprint of a crystalline structure in a given material (Bunaciu, 2015). Thus, for each sample, there will be a different pattern. In a polycrystalline sample, there are multiple planes with different (d) spacings between

planes that are parallel to the surfaces. Multiple planes parallel to the surface are also determined by Bragg's law. The angle between the incident beam and the lattice planes, as well as the angle between the diffracted beam and the lattice planes, is equal to the Bragg angle (2θ). As a result, the observed diffraction angle (in relation to the projected extension of the incident beam) is double the Bragg angle, or 2θ (Welze, 2004). For a strained polycrystalline the local lattice parameters varies in different places in the sample; the resultant peak is the summation of all the contributions from all the crystallites and thus broaden out the X-ray diffraction peak from the sample (Dolabella, 2022). This broadening covers all peaks that may have been compressed, stretched, or remain unchanged as a result of the strain effect in the polycrystal. The peaks will be broadening out due to 1) crystallite size; 2) micro-strain and 3) instrument broadening (Borzi, 2020, Maksimov, 2020). Both grain size and micro strain cause peak broadening, therefore, it is usually necessary to distinguish between the two when characterizing a sample. These contributions can be distinguished (Harrington, 2021).

- Peak broadening due to crystallite size

Scherrer has derived an expression for broadening of x-ray diffraction peaks due only to small crystallite sizes as shown in Equation 6 (Muniz, 2016; Valero, 2019, Scherrer, 1918, Hargreaves, 2016). The derivation of the equation is based on the assumptions of Gaussian line profiles and small cubic crystals of uniform size for which k = 0.94 (Langford, 1978). Diffraction lines from perfect crystals are very narrow. Line broadening from crystalline size and broadening from micro-strain are two properties used to determine the crystal size and calculate the amount of strain (Speakman, 2014, Balzar, 2004 and Saadi, 2022). This information can be sourced from an X-Ray diffraction pattern that results when X-Rays come into contact with a material specimen and scattering results.

$$\beta_{size} = \frac{K\lambda}{D\cos\theta} \qquad \text{Equation 6}$$

Where K is the shape factor; λ is the wavelength of the x-rays used; θ is the Bragg angle and D is the average crystallite size measured in a direction perpendicular to the surface of the specimen. To perform this exercise, one must look at a particular peak, measure the broadening, then apply the shape factor and using the angle, calculate the size of the angle.

- Peak broadening due to micro strain

The lattice strain in the material also causes broadening of the diffraction peaks, which can be represented by the relationship shown in Equation 7, where ε is the strain value.

$$B_{strain} = 4\varepsilon \frac{\sin\theta}{\cos\theta} \qquad \text{Equation 7}$$

- Peak broadening due to instrumentation

To determine the individual contributions of small crystallite sizes and lattice strains to the peak broadening in accordance with the Williamson-Hall method entails an initial step which includes the subtraction of the instrumental broadening effect from the experimentally observed peaks (Mishra, 2015, Jahil, 2022). Contributing effects resulting in instrumentation broadening are due to either imperfect focusing, unresolved α_1 and α_2 peaks, or the finite widths of the α_1 and α_2 peaks in cases where the peaks are resolved. The size of the Instrumental broadening effect is sourced from a standard powder whose very large uniform crystallite size so as not to cause any broadening (Cheary, 1992). Cline, 2010 used data from SRM 660a as the standard powder to model contributions due to instrumentation broadening. An x-ray diffraction pattern of the standard powder is recorded under instrumental conditions identical to those of the unknown specimen, so the peak broadening of the standard material due to instrumental effects is exactly the same as instrumental broadening in the diffraction pattern of the unknown specimen.

- Total peak broadening

The total broadening is the sum of the broadening due to the crystallite size and broadening due to micro-strain (Rabiei, 2020). This is after the instrumentational broadening has been subtracted as follows (Warren, 1969);

$$B_T = B_{size} + B_{strain} \qquad \text{Equation 8}$$

$$B_T = \frac{K\lambda}{D\cos\theta} + 4\varepsilon \frac{\sin\theta}{\cos\theta} \qquad \text{Equation 9}$$

Simplifying by multiplying by cos θ results in the equation:

$$B_T \cos\theta = \frac{K\lambda}{D} + 4\,\varepsilon \sin\theta \qquad \text{Equation 10}$$

This equation represents the formula for a straight-line equation where $y = mx + c$. The intercept (c) of the straight line being $\frac{K\lambda}{D}$; while the gradient (m) of the line given by $4\,\varepsilon$. Therefore, the size (D) of the crystal can then be calculated.

2.4.1.1.3 Sample preparation for PXRD

The process involved in sample preparation for PXRD measurements includes not only the right sample surface polishing, however, consistent polishing to ensure surface treatment is uniformly performed. In addition, polishing ensures the removal of deformations created during sample preparation as well as to ensure that a correct sample height alignment is maintained (Harrington, 2021). This is done to ensure accurate characterization in the analysis of samples. Samples were ground using successively smaller diamond grid slurries followed by colloidal silica polishing and then electrolytic polishing prior to performing PXRD. In the study by Elstad in 2016, it was concluded that electropolishing is the suitable preparation technique since 40 % retained austenite, in contrast there was obtained 14 % using ion sputtering and 25 % with chemical mechanical polishing (Elstad, 2016).

2.4.1.1.4 PXRD data analysis

PXRD is a technique often used to determine the underlying crystal structure of a material by verifying the crystallinity and structure of a sample. The technique is non-destructive and can be conducted at room temperature and pressure. The assessment of the underlying crystal structure is performed by fitting PXRD patterns to allow calculations of the material lattice parameters, the orientation of a crystal, stress in crystalline regions in the sample. XRD is generally a bulk characterization technique and produces an average diffraction pattern for the area measured. The diffraction pattern (see Figure 7) contains various metrics such as position, intensity, width, and shape which can be used to derive a calculated diffraction pattern.

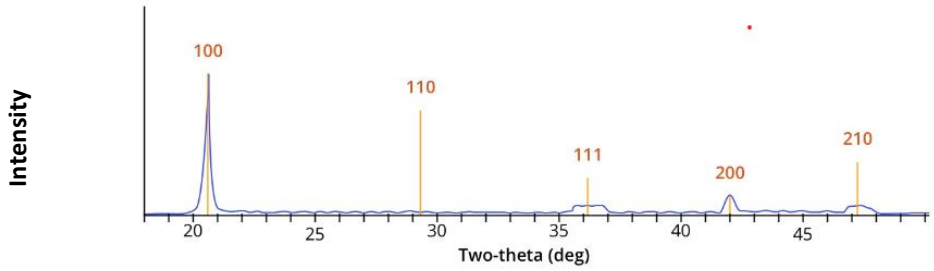

Figure 7: A typical example of a diffraction pattern XRD data plotted as a line trace with the angle in degrees on the x-axis, and X-ray intensity on the vertical axis. Source: (Bunaciua, 2015).

There are multiple methods available for quantifying line-broadening effects thus determining microstructural effects such as crystallite size, microstrain and dislocation parameters. Paul Scherrer, 1918 made use of X-ray patterns and crystallography is a simple way to calculate the size of nanocrystallites, especially for bulk nanocrystalline materials (Scherrer, 1918). The study surmised that broadening of diffraction peaks was as a result of the effect of grain size (Soleimanian, 2015). In the latter study, it is evident that XRD peak broadening is due to crystallite size and lattice microstrain and evidently several methods have been developed for the evaluation of size and microstrain. Below, is a brief discussion of the techniques used:

1. A commonly used methodology, Rietveld refinement (Rietveld, 1967) was initially presented as a refinement and extraction technique for structural parameters such as lattice constants, position of atoms in lattice and the fractions of phases. During Rietveld refinement, each of the variables that describe the diffraction pattern are adjusted to perform a pattern fit. Thus, the method is relatively intensive, and requires minimizing the sum of the weighted, squared differences between observed and calculated intensities at every step in a digital powder pattern. The Rietveld method requires knowledge of the approximate crystal structure of all phases present in the specimen (Misture, 2001). Conversely, the developed Rietveld software packages are provided to simultaneously evaluate the structural and microstructural parameters.
2. In all likelihood, the Williamson Hall (WH) (Williamson, 1953) plot is probably the most widely used method. This is attributable to the technique's ease of application. Originally, the method assumed the separation of size and strain broadenings in each peak via two Lorentzian functions. Thus, the methodology is amenable to errors hence the modified Williamson–Hall (MWH) and modified Warren–Averbach (MWA) methods are used to diminish inaccuracies. However, this method is still essential for understanding the qualitative behaviour of line broadening (Soleimanian, 2015).
3. The Warren-Averbach (Warren, 1950) method uses the deconvolution Fourier-transform method for determining the intrinsic physical line profile, followed by the Fourier method for evaluation of lattice imperfections (Marinkovic, 2001). The intrinsic line parameters are then extracted, such as 2θ diffraction line positions, full width at a half maximum (FWHM), integral breadths and others, that define diffraction line shapes, are further used to calculate the Fourier transforms of intrinsic diffraction lines. This methodology is thus time-consuming.

4. Another encouraging technique for the X-ray diffraction line profile analysis is the fundamental parameters approach (FPA) also known as the whole powder pattern modelling (Paolo, 2002). During this technique, fitting is done by convolution and corrections for instrument broadening and peak shift are built-in to the refinement. When an instrument is well characterised, line broadening can be analysed without a reference sample. Also, when a reference standard is used, which has different properties from the specimen with line broadening, some adjustments can be made for these differences (Cheary, 1992). The leading justification of this new method is based on the absence of requirements for analytical peak shape function like Voigt or pseudo-Voigt is needed. Thus, microstructural parameters in terms of crystallite size, size distribution and characteristics of linear and planar defects can be directly extracted from diffraction pattern.

All methods have limitations and advantages, and while a model based on an accurate physical description of the sample is always preferred, it has to apply to at least a majority of grains in a polycrystalline aggregate. The Rietveld analysis method showed that the scatter of strain values appears more significant which may indicate a possible link with other reasonable parameters. The Warren-Averbach analysis is the least-biased phenomenological approach, however, it is prone to limitations where there is significant peak overlap or large strains that do not follow a Gaussian distribution. Therefore, Rietveld refinement or a similar full-powder pattern method may be the only alternative approach for an arbitrary sample. However, it should be mentioned that these primary XRD analysis approaches are based on the assumption of isotropic peak broadening.

The FPA method offers a number of benefits as a method of profile analysis. It is based on a physical model of the diffractometer and its refined parameters should be self-consistent with physical dimensions of the diffractometer and the physical properties of the sample. As the profile shape is known, the FPA technique also provides greater certainty in the identification of weak peaks or impurity lines embedded in the tails of stronger line. In Rietveld analysis or quantitative analysis, FPA allows the profile shapes across the whole 2θ range to be fitted without any instrument-based parameters in the refinement. The focus of the refinement is therefore on the diffraction effects of the specimen and not the instrument.

Based on this analysis, this study will use the WH and the whole pattern fitting methodology for reasons descried above. The former, will be used as a basis of understanding the XRD technique

by performing manual pattern fitting. While the latter will be utilised as the qualitative method of calculation dislocation densities in the material specimens.

2.4.1.2 Dislocation Density Quantification

While Soleimanian et al, 2015 used Equation *11* to determine the dislocation density using the diffraction data of Ni, Cu and Al were fitted to the pseudo-Voigt function, applying the convolutional method and using the size and strain from WH method, the dislocation density is calculated using the equation proposed by (G.K. Williamson, 1956) where $\boldsymbol{\rho}_S$ and $\boldsymbol{\rho}_D$ are dislocation densities due to the crystallite size and microstrain, respectively.

Dislocation Density $$\rho = (\rho_D \rho_S)^{1/2} = \frac{2\sqrt{3}\langle \varepsilon^2 \rangle^{1/2}}{b\langle D_{vol} \rangle}$$ Equation 11

Where $\langle \varepsilon^2 \rangle$ is the mean square strain, b the Burgers vector and D_{vol} is the volume weighted average size.

2.4.2 Surface characterization technique

For a complete characterization of a microstructure both local and global information must be gathered, which requires the combination of different analysis techniques. PXRD is a bulk characterization technique and like the literature survey conducted in 2.4.1, there equally exists a number of local techniques termed as surface characterization techniques in this section.

To determine crystal orientation of metallic microstructures, polarized light may be used during phase-contrast imaging to increase image contrast by highlighting small details of differing refractive index. This technique is a derivative of the optical microscope modified to improve resolution and sample contrast (Kim, 2023); however, basic optical microscopes can be very simple. The sample can also be observed in a variety of ways depending on the information required. The maximum magnification power of optical microscopes is approximately limited to around 1000x because of the limited resolving power of visible light. While larger magnifications are possible no additional details of the object are resolved which is a major limitation of the technique.

There exist alternatives to optical microscopy which do not use visible light and can achieve much greater magnifications using electron imaging. These include the scanning electron microscope

(SEM) and the transmission electron microscope (TEM). Although the wavelength of electrons are ca. 100,000 times smaller than visible light, the resolving power of electron microscopes are only on the order of 1,000 times greater than light microscopes, due to lens aberrations. In the transmission mode, the intensity from an electron source is measured after it has passed through a transparent sample. In contrast, SEM features the scanning of an electron beam over selected regions of an opaque sample. The basic principles that govern electron microscopy are analogous to optical microscopy (Williams, 2003). Whereas optical microscopes use light and optical lenses to illuminate and magnify the sample, electron microscopes utilize high-energy electrons and electromagnetic lenses. For the increasingly greater resolution capabilities of modern SEM and TEM instruments, the sample must be magnified by approximately 100–300K and 1.5–2M times, respectively (Fahlman, 2011). Therefore, SEM is less sensitive than TEM and during dislocation density investigations, it is imperative to start with SEM and migrate to TEM where more resolution is required (Nicolas Brodusch, 2021).

2.4.2.1 Orientation imaging using SEM-EBSD

Electron backscatter diffraction (EBSD) used together with SEM is a powerful technique for measuring local crystal orientation changes. Commercially available EBSD equipment can identify crystal orientations by scanning samples. EBSD is a technique that involves acquiring and analysing Kikuchi diffraction patterns from the surface of a specimen using a SEM (refer to Figure 8).

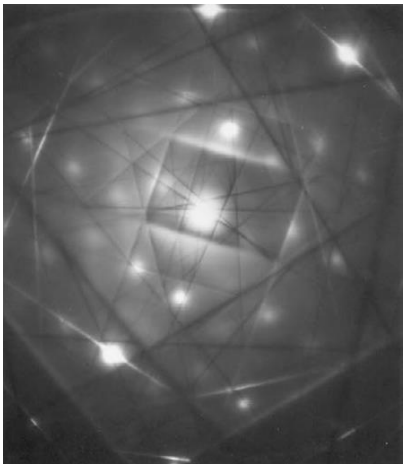

Figure 8: An electron diffraction pattern of an austenitic stainless steel (FCC) showing diffraction spots and Kikuchi lines. (Photograph by courtesy of Dr P.M. Champness and Professor G.W. Lorimer.) Source: (Hammond, 2009).

In this technique, a stationary beam of electrons is positioned on the specimen surface. Backscattered electrons are then diffracted at the crystal lattice planes within the probe volume, according to Bragg's law. To maximize the fraction of diffracted backscattered electrons that can escape from the specimen surface, the specimen is tilted such that it forms a small angle, typically 20 degrees, with the incoming electron beam. As a result, the diffraction patterns arose from a depth of up to 50 nm from the specimen surface. The diffracted signal is then collected and viewed through a low-light video camera interfaced with a phosphor screen (Randle, 2009).

The diffraction patterns obtained from EBSD provide crystallographic information that can be linked back to their position of origin on the specimen. Automated evaluation and indexing of the diffraction patterns are typically carried out, with the resulting data outputted in a variety of both statistical and pictorial formats such as orientation map providing a quantitative depiction of a microstructure area in terms of its crystallographic make up.

2.4.2.1.1 Local Misorientation Process

User-defined boundary maps can be created from misorientation angle data, allowing for the identification of areas with high concentrations of low angle boundaries, which are indicative of high concentrations of geometrically necessary dislocation density. Characterization of local misorientations can be performed using several methods, including assigning the same local misorientation value to each measurement contained within a grain, assigning each scan its own individual local misorientation value, or using a hybrid approach where each point in the scan has its own individual value based on the grain to which it belongs (Wright S.I., 2011).

The EBSD parameters utilized in this study by (Shao-Shi Rui, 2018) for misorientation analysis are Kernel Average Misorientation (KAM) and Grain Reference Orientation Deviation (GROD). As depicted in Figure 9, KAM is calculated as the average value of the misorientation between the kernel point and its eight closest neighbouring points, while GROD quantifies the misorientation between an arbitrary point and the reference point r, by considering the average orientation of the sub grain that encompasses the individual point. An example of the misorientation maps from the same study for the KAM and GROD values of each pixel are

shown in Figure 10 where KAM shows the local variations in orientations, while GROD shows the variations relative to the grain average.

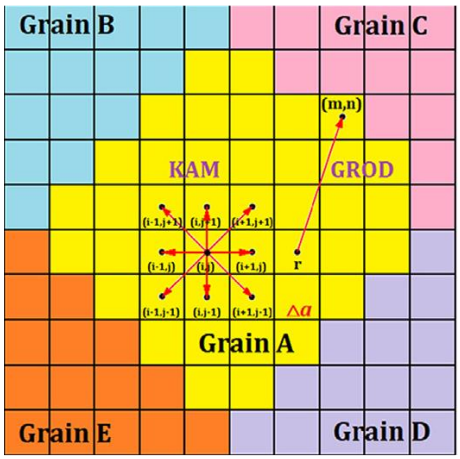

Figure 9: Definitions of KAM & GROD based on the square data structure (Shao-Shi Rui, 2018).

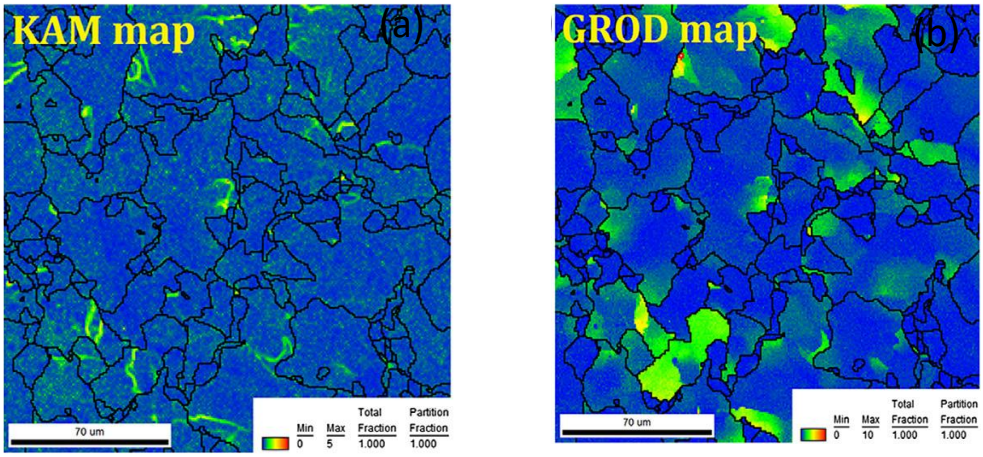

Figure 10: Examples of (a) KAM and (b) GROD map (Shao-Shi Rui, 2018).

KAM has a linear relationship with the geometrically necessary dislocation (GND) density (M. Calcagnotto, 2010) and was used as an average value in a high chromium heat-resistant steel to evaluate creep damage ratio by tracking the evolution of GND density with a high initial GND density ρ_0. The microstructure analysis using KAM for the 316LN austenitic stainless steel subjected to high cycle loading showed that there was high local misorientation near the grain boundaries, suggesting that the dominant deformation was mainly due to dislocations motion during the cyclic loading test (Xina, 2023). Godfrey in 2005 concluded that the Kernel Average

Misorientation (KAM) allows quantitative evaluation of the local plastic strain gradients and is usually used if plastic deformation results from dislocation slip and crystal lattice rotation (Godfrey, 2005).

Gussev, 2009 also used a two-prong approach analysis in the study of crystal orientation measurement using EBSD for damage assessment in irradiated material where KAM values were used to characterize changes in the local misorientation caused by geometrically necessary dislocations (Gussev, 2019). While at small strain levels applied to the specimen, the increased KAM values usually coincide with a GROD hot spot which was included in the analysis. However, increased KAM values are often observed along grain boundaries, indicating the formation of fine channels or slip lines at different locations. It was established that irradiation had a strong impact on KAM and GROD EBSD misorientation parameters. Thus, GROD maps revealed the formation of specific "hot spots" in the small strain area, in which the GROD value increased much more quickly in the irradiated steel than in the nonirradiated steel. In contrast, average KAM values showed very little overall changes (but strong localized increase inside the hot spots) in the small strain range. KAM and GROD approaches appear to be complementary Nzongang, 2018. KAM approach shows the magnitude of the gradient, which can be seen as the first derivative of the orientation field. While the latter shows the orientation field referenced to a fixed point.

2.4.2.1.2 Local Misorientation Quantification

The extent of macroscopic plastic strain due to cyclic loading in the material can be estimated from EBSD crystal orientations using scalar parameters, an example of misorientation angle EBSD maps is shown in Figure 11. In this study, a histogram illustrating the distribution of the misorientation angle results for AISI304 stainless steel subjected to deformation using the laser shock peening was investigated. The misorientation angle is calculated as the total number of pixels along all grain boundaries within the analysis area divided by the number of pixels along the boundaries within this misorientation angle. Also, the magnitude of local plastic strain can be confirmed by evaluating the misorientation angle between neighbouring points using EBSD analysis. In the study by (Kamaya, 2009), where nominal strain measured by the image correlation technique was compared to the spatial distribution of the local misorientation; the outcomes revealed that the local misorientation was consistent with the density of the geometrically necessary dislocations rather than with the magnitude of nominal strain.

In the orientation mapping study of microstructures of experimentally deformed bridgmanite and ferropericlase aggregates were strong misorientations which challenge the automatic

detection of grains; therefore, it was suggested that a standard limit criterion for the limitation of misorientation of 15° as a to discriminate sub-grains and grain boundaries. GROD was a useful consideration to highlight the strong strains undergone by the ferropericlase grains, but not well adapted to further quantification and preference was given to the KAM approach since more information regarding deformation was sought from the KAM map. (Kamaya, 2009), confirmed that the selected threshold value of 5° worked well for the type 316 stainless steel material and the measurement conditions.

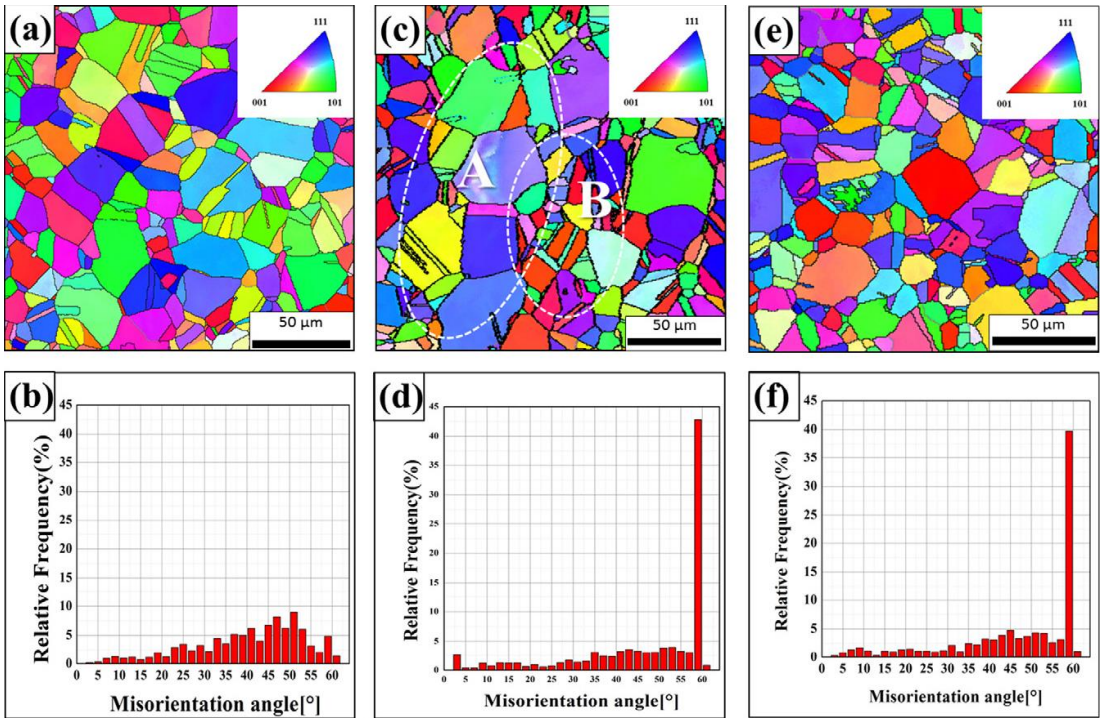

Figure 11: EBSD inverse pole figures of AISI 304SS for three different samples showing grain orientation corresponding to the phase orientation triangle per colour for sample 1 (a); sample 2 (b) and sample 3 (c) and corresponding histograms of number present versus misorientation angle between neighbouring grains for sample 1 (c); sample 2 (d) and sample 3 (f) (Lu, 2017).

Characterization of grain boundary misorientation distributions have been typically classified according to low/high angle type (Randle, 2009) using available software packages to provide information on the possible properties of the boundary. (Fukuya, 2013), studied the local strain distribution near grain boundaries under tensile stress using EBSD for cold worked irradiated SUS316 stainless steel where an increase in local strain was detected near grain boundaries by performing a detailed analysis of misorientation changes. The study confirmed that the increase

in local misorientation obtained by EBSD measurements can be attributed to local plastic deformation with an increase in dislocation density in plastically deformed stainless steel.

Research has shown that several EBSD misorientation quantities are calculated from the orientation maps for the evaluation and quantification of strain-induced changes in the structure such as the kernel average misorientation (KAM), grain average misorientation (GAM), and grain reference orientation deviation (GROD), to name a few. These parameters, being averaged for some area, correlate well with the degree of plastic strain, fatigue life fraction, and creep with the aid of a correlation curve connecting the selected EBSD misorientation parameter and thus leading to an accurate quantification of the degree of strain level.

2.4.2.1.3 Viability of the EBSD technique

An EBSD diffraction pattern quality is very sensitive to perfect crystallinity as the pattern is realised from the top few nanometres of specimen surface. The emphasis on the surface preparation is to ensure the EBSD data collection is accurate. Literature revealed the three most common sample preparation techniques for EBSD analysis namely, electropolishing, ion sputtering and chemical mechanical polishing or a combination of these. There is no preferred methodology in literature bearing in mind that the goal is to ensure a mirror surface finish for analysis. Electropolishing uses an electrolyte and induced current. Where diamond polishing is used, it is not a suitable final step in some materials because of the surface deformation introduced. Inadequate specimen preparation will result in variations from true data in diffraction pattern results which feed through to loss of data quality. (Kamaya, 2009) used this methodology followed by colloidal silica to achieve relatively flat surfaces free from damage. Chemical-mechanical polishing removes the surface by mechanical polishing with a suspension with different chemical properties. (Guo, 2014) also used this method in the slip band and grain boundary interactions in commercial purity titanium where the polish process was repeated until a crisp grain boundary structure was visible in optical microscope with polarized illumination. EBSD maps are generated at very shallow depths within the sample, so appropriate samples must be free of damage to the crystal lattices at the surface of the sample. Mechanical grinding and polishing in routine preparation of polished samples (such as microprobe samples) results in significant damage to crystal lattices near the surface of most materials. Therefore, it is necessary to perform additional chemical polishing on samples after they have been polished using abrasives. This is a labour-intensive and time-consuming process that requires experience with the materials of interest for optimal results.

The literature review highlighted the following advantages for the EBSD technique:

a) It is the quickest and most dependable method for gathering data on crystalline structure and orientation in a solid crystalline phase. Unlike optical techniques, it can be used to gather data for all types of symmetries (including isotropic phases) and opaque phases. The data provides accurate 3-dimensional orientations for individual crystals, which is more detailed than the 2-dimensional orientations provided by x-ray pole figures (Swapp, 2022). The spatial resolution can be on the order of several microns, which is much superior to resolution attainable using selected area channeling (SAC) techniques. EBSD data acquired using either a scanned electron beam, or (better) an automated stage and a stationary electron beam can include analyses of thousands of individual grains in a run accomplished in hours; acquisition of data for tens of thousands of individual spots in a single one-day run is routine in most laboratories.
b) Data are best acquired with a stationary beam, or with the beam scanning over a small area of the sample (high magnification). At lower magnifications, the angle of incidence of the beam on the periphery of the area of interest creates artifacts in the EBSP and the data become difficult to index accurately. The best solution is to use a stationary beam (scanning mode off) and acquire data over the area of interest by moving the sample. The procedure requires an automated specimen stage, and data acquisition is considerably slower than acquisition using beam scanning.

Kamaya, 2009 showed that the misorientation calculated from crystal orientations contains substantial error when the measured misorientation is relatively small. Some of the error contributions are due to the surface condition of samples, the number of pixels of the camera used to acquire EBSD patterns and parameters for identification of crystal orientation from obtained EBSD patterns. The deterioration of the diffraction pattern reduces the accuracy of crystal orientation identification. Even with optimum surface preparation, plastic strain deteriorates the EBSD pattern. This is the limitation encountered when utilising this technique.

2.4.2.2 Transmission Electron Microscopy (TEM)

TEM is a commonly used technique for the investigation of the deformation microstructure on the nano and/or microscale (refer to Figure 3) as it allows the direct investigation of lattice defects such as dislocations, stacking faults and micro twins in individual grains (Weidner, 2013). This technique captures electrons that pass through a sample; therefore, the sample should be

very thin and uniform per area of analysis (i.e., electron transparent). Some Bragg diffraction of the electron beam will occur in the localised region around the core due to the lattice distortion of the dislocation nucleus. Therefore, dislocations will appear as dark lines in bright field TEM images since the intensity is shifted away from the 'straight through' beam (Anon., 2008).

Figure 12 shows a schematic Kikuchi pattern of a single crystal indicating the contrast conditions and tilt positions during TEM analysis in identifying the character of dislocations and crystallographic planes of elongated dislocation loops and to obtain three-dimensional information on dislocation configurations using stereo microscopy (Simon, 2010).

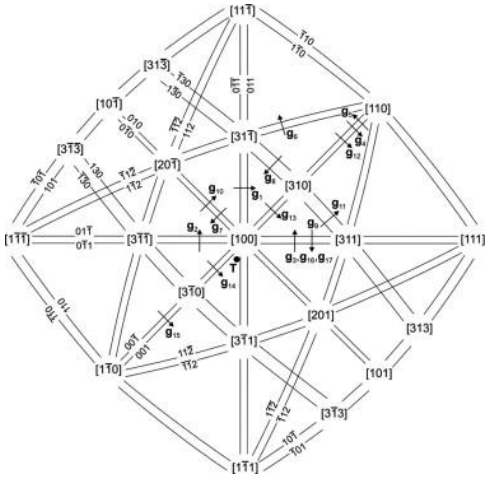

Figure 12: Schematic Kikuchi map of the single crystal with tilt angles and contrast conditions (Simon, 2010).

Pesicka, 2010, demonstrated the potential of using scanning transmission electron microscopy (STEM) imaging in combination with a high-angle annular dark-field (HAADF) detector for measuring dislocation densities in a complex engineering material. This is because in earlier work, shortcomings were observed in sourcing good TEM micrographs from dislocations. The shortcomings included the effect of small changes in tilt angle, objective lens defocus and specimen thickness amongst other issues. Representative dislocation micrographs are generally obtained from thin foils, which are strongly affected by the sourcing of TEM bright-field images. Generally, inelastic scattering of the electrons within the specimen results when thin foils are sourced from thicker regions of specimens thus yielding chromatic aberrations of imaging lenses. This is avoided in the resolution of STEM images which are not limited in the same way and is thus favourable for imaging thicker samples. Earlier research (JM Cowley, 1992) reported that dislocations can show bright contrast in STEM mode due to channeling contrast and the diffusion of scattering produced from the static displacement of the atoms around the dislocation cores.

Kostka, 2007 studied TEM micrographs to understand the heterogeneity of recrystallisation process and its dependency on local dislocation densities and local misorientations between micro grains amongst other microstructural features as shown Figure 13.

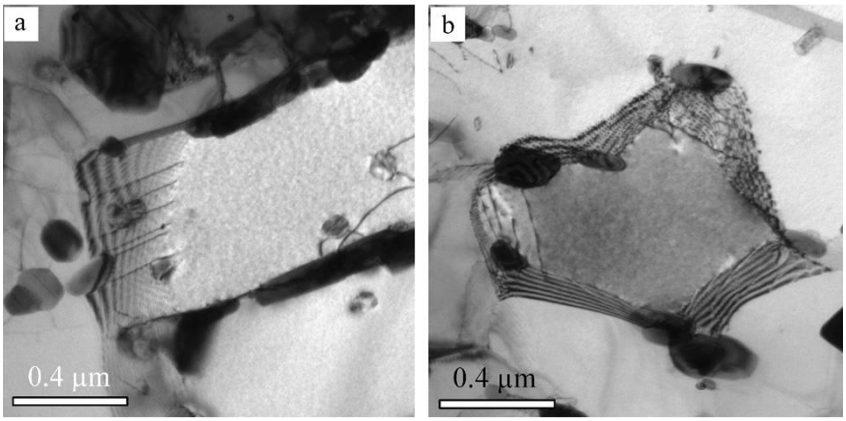

Figure 13: TEM micrographs (Kostka, 2007) providing microstructural evidence for a direct effect of micro grain boundary carbides on dislocation processes at boundaries and on boundary migration.

In another study, single crystal aluminium in-situ tensile experiments were used to understand dislocation interactions and microstructural evolution sequence during deformation using TEM. The findings showed that dislocation cross slip is essential for the transition between microstructural stage evolution and the processes observed conform to the common knowledge of dislocation pattern formation and evolution in bulk samples. However, there are key limitations to in-situ TEM experiments that question the reflection reflect bulk behaviour due to the thickness of the sample and surface effects (Landau, 2010).

2.4.2.2.1 Dislocation quantification using TEM.

Literature has revealed two equations for quantitative dislocation measurements in TEM micrographs. The first, Equation 12 is a liner intercept methodology used in the dislocation density within lath martensite in Fe–C and Fe–Ni Alloys (Morito, 2003) study.

Dislocation Density $$\rho = \frac{2N}{Lt}$$ Equation 12

Where *N* is the number of intersections with dislocations made by randomly drawn lines of length *L* and *t* is the thickness of TEM foil.

The formula is similar to utilised in Equation 13 by Pesicka, 2003 in the evaluation of X20 thin foils and in the 12%Cr tempered martensite ferritic steel (Pesicka, 2010).

Dislocation Density $$\rho = \frac{1}{t}\left(\frac{\sum n_v}{\sum L_v} + \frac{\sum n_h}{\sum L_h}\right)$$ Equation 13

This measurement allows for micrograph counting of two sets of horizontal (L_h) and vertical (L_v) reference lines which intersect the dislocations (n_v times in vertical and n_h times in horizontal direction). This sum is divided by the foil thickness t.

Literature also shows that dislocation density quantification is enabled by image processing techniques have been implemented on TEM images. Higher magnifications from atomic resolution images using morphological illustrations can enhance dislocations. This technique includes the segmenting the images into foreground and background pixels; thresholding method or edge detection of the images to determine the average dislocation size discussed by (Hindson, 2011). The original images required separations of the particles from the substrate background, and this was accomplished by the multilevel segmentation. The proposed method offered the scale invariant feature applied to images with different magnifications, yielding comparable average size. This multilevel image segmentation is demonstrated as a rapid and accurate method of quantitative analysis for dislocation networks in TEM images. This technique is however not suitable for this current study as the only suitable for high contrast images but less effective in the case of dislocation amassed in one area without clear boundaries (Viswanathan, 1989).

2.4.2.2.2 Thin foil preparation techniques

Sample preparation of TEM specimen to transparent thinness is a delicate and time-consuming task where care must be taken to ensure that no external strain and/or contamination affects the microstructure of the specimen in its original form. The following section discuss available methods from literature to ensure workable sample preparation for the benefit of accurate results. Available methods for the measurement of the thickness of thin-foil specimens used in TEM are either laborious or have limitations (Pan, 1994) as discussed in the section below.

a) Method 1 utilises available crystallographic features, such as slip plane traces by tilting the foil to align the defect plane parallel with the electron beam. This method results in accurate values of the foil thickness measured in the beam direction. If the foil surface

orientation is not precisely known, no errors are foreseen in the measurement of the sample thickness.

b) Method 2 uses electron irradiation to deposit contamination spots on top and bottom surfaces of the foil. The foil is tilted through a known angle to cause separation of the spots in the image plane from which the foil thickness may be calculated. The technique is shown to overestimate true metal thickness because of surface film presence since the area of fast changing contrast marking the apparent edge of the spot is not on the foil surface but is on a broad contamination deposit whose thickness is changing much more slowly. This limitation is overcome by utilising one of the condenser lenses to aim the electron beam in a thin line on the foil during displacement. The method allows for several measurements of thickness covering a relatively large area of foil to be made per contamination experiment including the joining of the foil edge to measure thickness profile of the foil right up to the edge.
c) For method 3 a convergent beam diffraction technique has demonstrated that multiple beam diffraction and absorption effects can limit the accuracy of the method. Such effects are most pronounced for low order planes. The above techniques are compared, and it is shown that the crystallographic and convergent beam technique measure the thickness of metal in the beam direction.
d) Method 4 utilises x-ray measurements where the x-ray intensity is a function of beam current and foil thickness. The former dependency makes it difficult to correlate x-ray intensities with a particular value of foil thickness.
e) The electron energy loss spectroscopy method using the log ratio of the inelastically scattered electrons to the elastically scattered electrons gives the mean free path of an electron in a particular material. (Malis, 1988)

After performing polishing, the sample specimen will be amenable to corrosion or oxidation, and it requires cleaning before inserting in a TEM column. Plasma cleaning is often used where energetic electrons and ions that bombard the surface and break the carbon-hydrogen bonds while maintaining the specimen surface microstructure. The hydrocarbon compound is thus gradually reduced in molecular weight and is pumped away in the vacuum of the cleaner. After the finalisation of the steps, the specimen is ready to be inserted into the TEM column for analysis. Several polishing methods can be utilised as follows:

a) Electro-polishing is called the final thinning of the sample and can only be used for electrically conducting materials without any mechanical damage.

b) Jet polishing has also been used where a single jet of gravity led electrolyte to a thin disk supported specimen on a positively charged gauze. (Simon, 2010) used this method and cut out and mechanically ground 3mm cylindrical samples to a thickness of 120 µm discs. Thereafter, electrochemical double jet thinning was performed in a Struers Tenupol 5 at 293 K using an electrolyte consisting of 20% sulfuric acid and 80% methanol at a voltage of 19.5 V.
c) Ion milling is often performed for non-metallic samples; therefore, it will not be discussed any further in this study.
d) Preparation of TEM samples by Focused Ion Beam (FIB) milling using Ga FIB technology are one of the most precise techniques now routinely used for example in failure analysis or material science. FIB columns are commonly combined with the Scanning Electron Microscopy (SEM) technique for observation during the preparation process and for the enhanced navigation, end-pointing and analytical capabilities. This FIB-SEM combination makes TEM sample preparation process much easier than before. However, when TEM sample size increases to several tens of µm, the preparation time increases considerably due to low Ga FIB milling speed (Delobbe, 2014).

2.4.2.2.3 Viability of TEM technique

It is evident from research that successful application of the technique exists, however, there remain challenges with TEM imaging that limits its application as discussed below:

a) The variability of dislocation densities between different micro grains but also within one micro grain also adds to the limitations of the technique, although, it is possible to account for this microstructural heterogeneity leading to the scatter of the TEM data and tends to increase as the average dislocation density of the material decreases. TEM results are averaged through the thickness of the specimen; there is thus projection-limitation which may result in the incorrect interpretation of the artefacts that are often realised when imaging. TEM specimens need to be electron transparent such that enough intensity falls on the screen, to give an interpretable image in a reasonable time. This essentially means that the specimen needs to be thin.
b) TEM can yield excellent diffraction data with exceptionally high spatial resolution for individual crystals, but sample preparation is considerably more involved than it is for EBSD studies, and most TEM specimens can only be examined over an area that is relatively small compared with areas accessible using EBSD.

c) Since this is a high-resolution imaging technique, only a small part of the specimen is viewed at any one time. Thus, the higher the resolution, the worse the sampling abilities of the instrument. This limits the user to an investigation with techniques that offer poorer resolution but better sampling, such as the SEM.

2.5 Chapter summary

The literature survey shows that several approaches can be considered for the investigation of dislocation densities in a material. Each investigation technique has advantages as well as limitations. This prompts the use of a combined inspection technique approach as a safeguarding and/or confirmation element into the project study.

To perform this exercise, the starting point should entail for the characterization of the material specimen before and after dislocation movement as well as the understanding of effect of material microstructure performance during dislocation movement. A design test case depicting the applicable material damage mechanism leading to deformation characteristics is mimicked/simulated. For this project, fatigue testing methods were reviewed, and the application of the S-N curve was investigated. The general approach in literature is to characterise the fatigue in the material with a testing regime that is representative of the material fatigue behaviour as well as the design of the specimen to ensure the distribution of the load to the test region.

Post damage induction in material specimen, the microstructure evaluation of dislocation densities in the materials can be investigated by viable bulk and/or surface inspection electron microscopy techniques which have inherent properties as follows:

- For PXRD, the research review conducted on a diffraction peak profile analysis, PXRD, has become a powerful tool for the investigation of microstructures in bulk or granulated materials due to its extraordinary development in the last two decades (Ungár, 2001). It therefore lends itself as an extended method complementary to direct methods, such as SEM or TEM. Modelling procedures have been developed to obtain microstructure parameters, which can be directly related to the quantities obtained by more direct microscopy surface characterization techniques. The basic objective of the whole pattern fitting technique is to be able to fit any powder diffraction profile using a physically based model to describe both the instrument profile and any diffraction broadening generated by the specimen. One of the intrinsic benefits of the fundamental parameters approach

is its adaptability to any laboratory diffractometer. Good fits can normally be obtained over the whole 2θ range without refinement using the known properties of the diffractometer, such as the slit sizes and diffractometer radius, and the emission profile. To accommodate a monochromator or to compensate for the fact that certain aberrations are not completely independent, fine tuning is sometimes necessary to accommodate (Cheary, 2004).

- EBSD carried through in an SEM on the other hand has become functional in combining local and global data through the analysis of Kikuchi patterns. The SEM technique focuses on obtaining the orientation of crystals point by point in a scanned area, allowing to observe the grain structure and to quantify the length and character of misorientation boundaries (Schwartz, 2000). While PXRD, allows for the characterization, including the estimation of average diffraction domain sizes and dislocation and stacking fault densities. In this study, PXRD investigation will be limited to strain and crystallite size measurements only. No phase analysis of the material of interest will be undertaken due to the interest being limited to the crystallographic examinations during material deformation.
- TEM allows direct observation of microstructural features of a material at the local level. Qualitative and quantitative analysis of dislocation density analysis has been implemented by various researchers. However, the technique is onerous in the execution of sample specimen preparation.

Below is a brief methodology (approach) that will be undertaken in this study based on this literature study discussed in this section.

- The quantification of fatigue damage is related to the initial material state and the evaluation of changes occurring throughout the operation. Thus, baseline fatigue damage levels are required for the determination of remaining life. To enable effective characterization of fatigue damage, samples with differing levels of fatigue using the model material will be beneficial. To ensure statistically meaningful data, 3 samples at each stress level of interest has been recommended. This same specimen configuration will be implemented throughout the study.
- Microstructural evolution as a result of cycling loading will be evaluated using diffraction peak broadening analysis. Based on the literature review the following approach will be adopted.

- Polishing of sample specimen for PXRD testing the study will be done with 5% Perchloric acid methanol solution.
- X-ray diffraction profile analysis where the instrumental line contributions and sample contributions are fitted with a convolution of different physics-based equations. Two analysis methods for extraction of microstructure size/micro-strain will be used. The first, WH plot method where plot strain and crystalline size can be read off the graph. Although this method is time-consuming, a comparison a whole pattern fitting methodology will be adopted. The second method applies fitting by convolution and corrections for instrument broadening and peak shift are built-in to the refinement.

5. The same samples will be characterised using TEM and EBSD for additional qualitative methods to compare the trends with the results obtained from PXRD peak profile analysis. Fore EBDS, local misorientation using user-defined boundary maps will be created from misorientation angle data, allowing for the identification of areas with high concentrations of low angle boundaries, which are indicative of high concentrations of geometrically necessary dislocation density. Same as (Shao-Shi Rui, 2018), misorientation analysis using Kernel Average Misorientation (KAM) and Grain Reference Orientation Deviation (GROD). While TEM will used ADF STEM since it suppresses background diffraction effects and provides a better resolution of the dislocations in the sample.

Chapter 3. AISI 316L stainless steel fatigue testing and characterization

3.1 Material Characterization

Newly manufactured AISI316L bars with 12 mm diameter were sourced for this study. The material certificate for the bar supply indicated that the material was supplied in the cold drawn and polished condition. The chemical composition of the material was in line with the literature specification of AISI316L stainless steel (Padilha, 2003).

A further confirmation of the mechanical properties was performed by subjecting a portion of the as-received material to a tensile test according to ***ASTM E 8: Standard Test Methods for Tension Testing of Metallic Materials.*** The results of the test are shown in Table 1. To lower the yield and tensile strengths of the extruded material, the specimens were then annealed in the furnace for 15 minutes at 1050^{o}C and quenched in oil for approximately one minute. The yield and ultimate tensile strength showed alignment to values found in literature. In its annealed state, the AISI316L stainless steel presented a microstructure that is fully recrystallised with low dislocation density.

Table 1: Mechanical Properties of AISI316L stainless steel

AISI 316L	Ultimate Tensile Strength (MPa)	0.2% Proof Strength (MPa)
Annealed	515	227
Cold drawn	716	605

3.2 Fatigue Characterization

For proper fatigue characterization of a material for a given application, it is necessary to obtain test data whose loading represents the expected loading that will be experienced by the material in the application. To mimic the characteristics of fatigue as a result of stress cycling, a test plan was developed defining the minimum and the maximum force each specimen would be subjected to. The determination of these limits was based on the ultimate tensile strength (UTS) and the yield strength (YS) of the steel. If the stress amplitude is equal to the UTS then the specimen should fail at the first cycle as the limit of endurance would have been reached. This is

therefore not desirable to fulfil the requirements of the study as there will not be any fatigue initiation in the specimens. However, if the stress amplitude is set to a value equal to the yield strength, it is believed that the specimen will initially elastically deform and thereafter operate for a number of cycles prior to failure.

The formulae used to calculate the testing parameters have been discussed in 2.3 with Equation 1 to Equation 4. It should be noted that even though these are represented in stress, the final inputs into the test matrix are done based on equivalent forces by multiplying the stress with the area of the gauge section of the specimens.

Initially, a stress ratio (R) was chosen, and this is defined as the ratio of the minimum stress and the maximum stress for the given cycle as shown in Equation 1. The two reference conditions for obtaining fatigue properties are R = -1 and R = 0. The former is for the unidirectional stress, while the latter, R = 0, is known as the fully reversed stress. R = 0.1 was chosen for this test which means that the specimen will be loaded to 90% of the stress applied as the maximum stress level and then released back to the preload. Thereafter, the remaining test parameters as per Equation 2 to Equation 4 were calculated as discussed in Section 2.3.

3.2.1 Specimen Geometry

The specimen was intentionally designed to fail in the test section, so a smaller gauge area was included in the design for the test section. The grip section of the specimen was based on the testing machine used, but an acceptable ratio was incorporated between the test section and grip section to ensure that the failure of the test section was not affected by the specimen's gripping method. To avoid failure due to sharp edges in the specimen design, a circular cross-section specimen was selected in this study. The chosen specimen dimensions were as follows:

a) Test section diameter – 6.35 mm
b) Grip section diameters – 12.00 mm
c) Test section length – 25.40 mm
d) Overall specimen length – 170 mm
e) Radius – 50.80 mm
f) Surface finish – 0.3 µm

In line with the requirements of the standard, the grip cross sectional area was designed to be approximately two times the test section area. While the blending fillet radius was designed to be at least eight times the test section diameter to minimise the stress concentration factor of

the specimen. The test section length was designed to be four times the test section diameter. The specimens were machined at the UCT mechanical workshop according to the drawing shown in Figure 14.

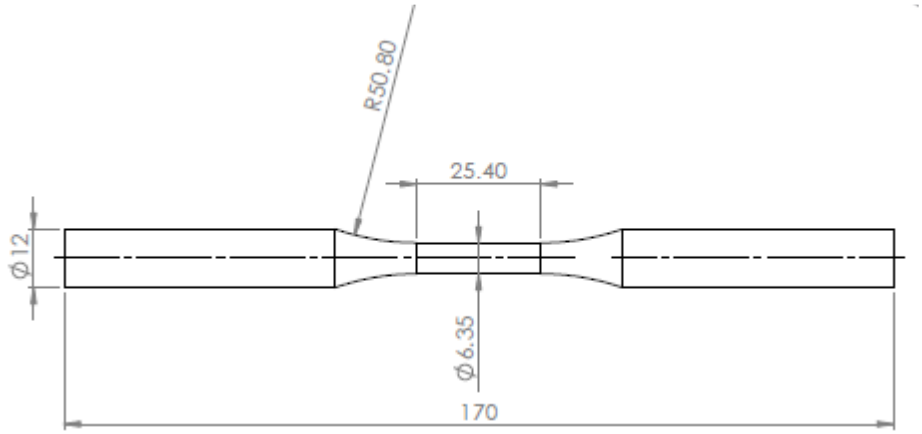

Figure 14: Stress Controlled Testing Specimen Configuration

Post the machining, polishing of the specimen was done to the desired surface finish. Visual inspections with the naked eye as well as low power magnification were conducted on all specimens prior to fatigue testing to check for any abnormalities or defects. The specimens were cleaned to remove any surface oil films and fingerprints and thereafter a dimensional analysis was performed. Thereafter, a series of polishing of the gauge error with increasing grit of silicon carbide paper was cautiously executed. This was followed by polishing using a cloth laden with diamond paste particle size to achieve a mirror finish surface.

3.2.2 Force Controlled Fatigue Testing

The fatigue testing of all specimens was conducted on an Instron fatigue testing machine which is a high stiffness servo hydraulic testing system rated at 250kN. The design of the fatigue testing in this project was based on the ***ASTM E466-15: Standard Practice for conducting force controlled constant amplitude axial fatigue tests of metallic materials***. The test was performed in a uniaxial direction at stress levels of interest at room temperature.

Two types of tests were performed, the initial test was to characterise the fatigue limits of the stainless steel by performing a number of fatigue tests at a determined peak stress level for each sample. The number of cycles where fracture occurs are then recorded and potted on an S-N curve. An additional number of specimen was also added to Table 2 below to sumplement the plot for the S-N curve.

Table 2: Fatigue Testing Matrix

No	Testing stress	Force (kN)	F max (kN)	F min (kN)	Fa (kN)	Fm (kN)	Specimen Marking
1	480	15,164	15,164	7,582	3,791	11,373	T1-1
2	480	15,164	15,164	7,582	3,791	11,373	T1-2
3	380	12,005	12,005	6,003	3,001	9,004	T1-3
4	380	12,005	12,005	6,003	3,001	9,004	T1-4
5	280	8,846	8,846	4,423	2,211	6,634	T1-5
6	280	8,846	8,846	4,423	2,211	6,634	T1-6
7	180	5,687	5,687	2,843	1,422	4,265	T1-7
8	180	5,687	5,687	2,843	1,422	4,265	T1-8
9	150	4,739	4,739	2,369	1,185	3,554	T1-9
10	150	4,739	4,739	2,369	1,185	3,554	T1-10

The second batch of fatigue testing comprised of specimen where the fatigue test was stopped at a predetermined number of cycles prior to material fracture at a determined peak stress level as discussed in Section 3.4, which translates to the material microstructure states for each specimen.

3.3 Force Controlled Fatigue Testing Results

3.3.1 S-N Curve

Data from the forced controlled testing discussed in 3.2.2 was plotted on an S-N curve shown in Figure 15. A best fit curve plotted through the centre of the scattered points indicates that some points are above the line representing longer life while others fall below the trend line predicting shorter life. The shape of the line is a continuous sloping curve. The failure points on the S-N curve indicate that specimens mainly failed in the high cycle fatigue region which occurs at cycles above 1.00E+04. In high cycle fatigue, the macro-stresses are typically well below the yield strength of the material, so there is no plastic deformation anywhere other than the tip of the fatigue crack. Since the uniaxial test specimen is not pre-cracked, the applied macro-stress is greater than the yield stress and thus represents a stress situation where the entire diameter cross-section acts as the stress raiser. The last point on the graph is for a specimen that did not fail and is denoted by an arrow to the right. This shows that the stainless steel has nominally infinite fatigue life at lower stress levels.

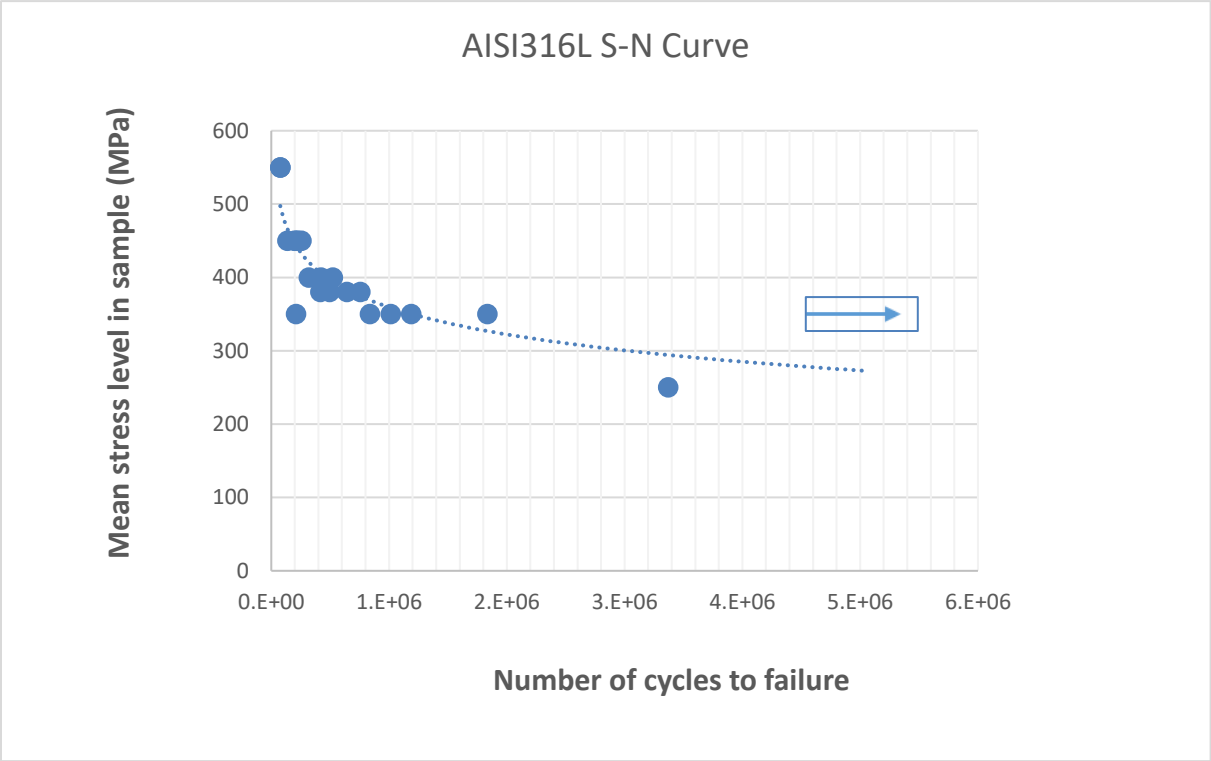

Figure 15: S-N curve for AISI 316L stainless steel

3.3.2 Fracture surface visual examination

The fractured specimens from the fatigue test carried out were analysed visually. The fracture surface was generally flat indicating the absence of an appreciable amount of gross plastic deformation. The initiation zone was at the surface of the specimen. The crack growth region was represented by clam shell marks which ran perpendicular to the initiation site. The fracture surfaces at lower stress levels showed a larger area of crack growth prior to fracture in relation to specimens subjected to a high nominal stress.

3.3.3 SEM evaluation

For a microstructural analysis, the specimens were imaged on the TESCAN MIRA3 SEM; the overview image of the fractured surface represents three distinct areas of the specimen denoted as areas **I**, **II** and **III** in Figure 16. Area, **I** viewed with magnifications of less than 500x, shows the crack initiation site as characterized by the uneven cleavages as seen in Figure 17 (a). The surface represents a typical stage **I** fatigue crack fracture that principally occurs by slip plane cracking.

Stage **I** fatigue is normally observed on high-cycle, low stress fractures and is frequently absent in low-cycle, high stress fatigue Figure 17.

The crack is then propagated through the material and the area II is characterised by the presence of fatigue striations on the fracture surface. This is the largest portion of the fracture surface and is influenced by the magnitude of the alternating stress. The fatigue striations as shown in Figure 17 (b) are in the direction of crack growth and often propagate on multiple plateaus.

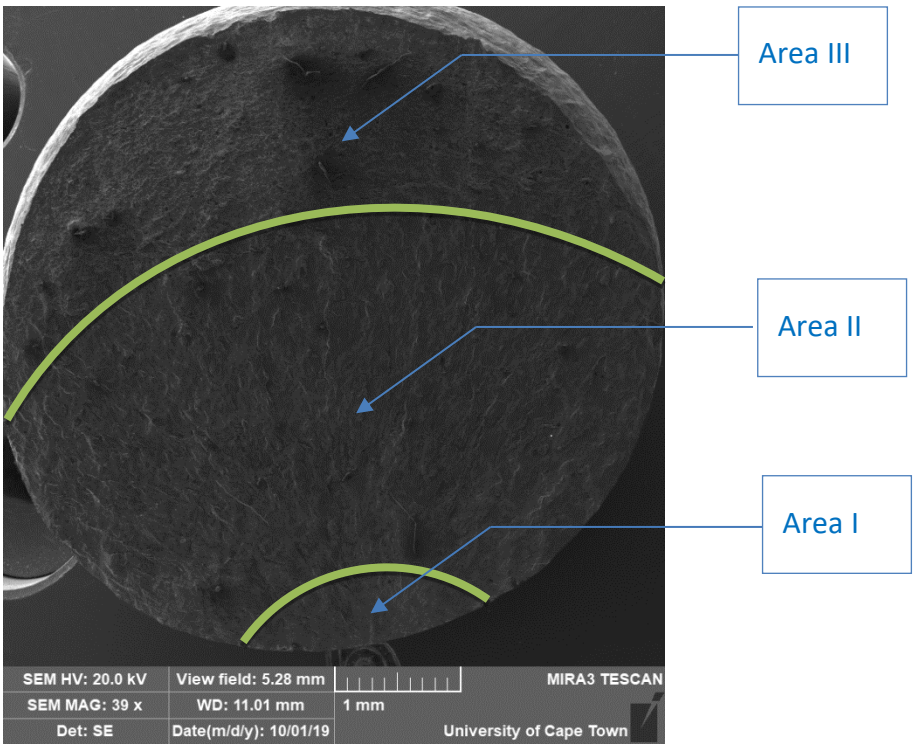

Figure 16: Overview of fractured surface on AISI316L observed using SEM showing three distinct fracture surface areas.

The final part of the surface clearly depicts dimpled morphology where the striations are progressively replaced by the static fracture mode and the SEM clearly depicts the presence of a dimpled rupture. This part represents the stage **III** crack growth as seen in Figure 17 (c). This represents the final fracture phase where the fatigue cracks become unstable, and the part ultimately fails.

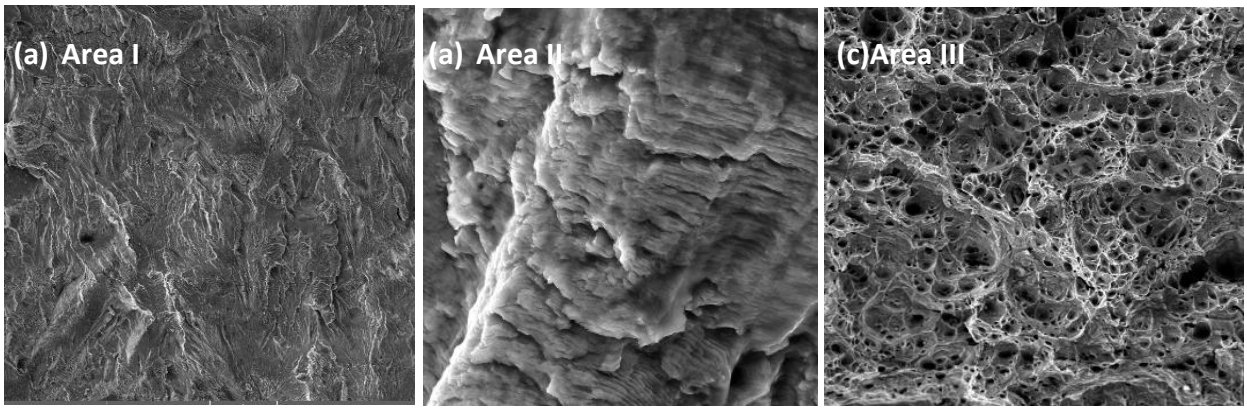

Figure 17: SEM image of fractured surface for (a) Area I, (b) Area II and (c) Area III

3.4 Chosen Material States

The section above shows the significance of gathering sufficient data to generate an accurate S-N curve in order to fully depict the true fatigue resistance of the part. Different methods can be used to generate an S-N curve. In this dissertation, the gathered data was fitted using a best fit trendline. An analysis of the data shows that specimen tested below the 350 MPa experience no failure. Using this safe stress limit and lower, a few material states were chosen as discussed below.

3.4.1 Extruded specimen

The specimen is prepared from an extruded axis-symmetric round-bar of AISI 316L stainless steel thus it is in the same orientation as all the other specimens in this study.

3.4.2 Annealed specimen

This specimen is sourced from the as-received (extruded) specimen and annealed as discussed in Section 3.1 and no deformation was induced in the material specimen. It is expected therefore that the material will be relatively dislocation free. After annealing, other material states were introduced to varying degrees of cyclic deformation as detailed in items 3.4.3 to 3.4.6.

3.4.3 Specimen cycled to 500 000 cycles.

This specimen was likely to coincide with a period of crack initiation or pre-crack-initiation where very fine cracks may be evident. It was cycled to half a million cycles at a stress level of 320 MPa.

3.4.4 Specimen cycled to 1 million cycles.

This specimen was subjected to double the number of cycles as compared with the previous specimen at the same stress level. The level of damage will be investigated further and compared to the previous specimen. However, the expectation is that more deformation than the previous specimen should be expected.

3.4.5 Specimen cycled to 3 million cycles.

This specimen was cycled to three million cycles at 320 MPa. It should also show increasing deformation in the material sample. However, the cycles should still in low cycle fatigue region of the material.

3.4.6 Specimen cycled to 11 million cycles.

This specimen represented maximum fatigue deformation to be induced on the specimen reaching 11 million cycles at a stress level of 350 MPa. It is expected that higher level of fatigue damage will be evident in the specimen microstructure.

3.5 Discussion

The discussion section will focus on the microscopical evolution of the material during load cycling. This is used to inform the dynamics of material changes prior to the onset on crack initiation. Based on the material states chosen in this study, this section aims to highlight the complexity of the dislocation movement which will inform the sensitiveness of the microstructure evaluation technique once microscopy is performed in the sections to follow.

3.5.1 Effecting of dislocation movement during fatigue testing

The complex process of dislocation microstructure evolution during cyclic loading involves multiple deformation mechanisms that operate across multiple length and time scales and interact strongly. Both in situ and post-mortem experiments are limited in providing information on the evolution of the dislocation microstructure under highly controlled and often idealized loading conditions. Both the crystal size and the initial dislocation density play an important role in the subsequent evolution of the dislocation microstructure. Dislocations glide, collide, then cross-slip in a repeated manner, which leads to storing more dislocations within the crystal rather than their escape. They also showed that the build-up of dislocation microstructures, particularly

dislocation cell structures, goes hand in hand with cyclic hardening. Plastic deformation in metals results from the motion of interacting dislocations developing heterogeneous structures with dislocation depleted and dislocation rich zones.

The presence of initial mobile/immobile dislocations can affect the microstructural evolution, as they may act as pinning points or dislocation sources and contribute to the formation of dislocation groups. However, it is expected that the alignment of dislocation groups in other regions will continue to evolve during more cycles and reach a saturation stage.

3.5.2 Initiation of stage I fatigue cracks

Early fatigue damage has been studied in several model and structural polycrystalline materials using modern experimental techniques. Early initiation of fatigue cracks was found to be related to the localization of the cyclic plastic strain into persistent slip bands during cyclic loading. Internal dislocation structure of the persistent slip bands and the evolution of the surface relief as surface persistent slip markings are documented. The model of the surface relief formation describing the formation of extrusions and intrusions is briefly described. In many austenitic stainless steels, such as the one investigated in this study, it has been discovered that cracks nucleate at various interfaces such as twin boundaries, grain boundaries, extrusion/intrusion slip bands and inclusions. The deformation behaviour of face centred cubic metals is greatly affected by slip dislocations and stacking fault probability. Further, literature has shown proved that at an early stage of deformation, fine deformation twins develop, often observed under reasonably high-resolution microscope. However, these deformation features like dislocation substructures and twins arising due to the activity of perfect and partial dislocation depend highly on the orientation of slip direction with respect to the loading direction.

Cyclic loading of material, either single crystals or polycrystals, results in appearance of cyclic strains in a particular location, usually in the area of stress concentration. Plastic strain and cyclic plastic strain in a material is facilitated by the presence of dislocations. Dislocation segments expand under external stress in a crystallographic slip plane and produce dislocation loops. Dislocation multiplication results in formation of slip lines on the specimen surface. Slip lines in uniaxial straining represent slip steps having small height. Therefore, already in uniaxial straining plastic strain is not distributed homogeneously. Inhomogeneity of cyclic plastic strain is even more pronounced. In cyclic loading dislocations in active slip planes formed during initial tensile or compressive quarter cycle facilitate slip in opposite direction.

The intrusions are thin and often covered by an extrusion. Since intrusions represent very sharp surface defects situated in the area of high local plastic strain amplitude fatigue cracks starts to initiate from the tip of the intrusion. Stage I crack is thus initiated and starts to grow, initially along the PSB. Formation of the PSMs which contain intrusions provides the appearance of numerous sharp defects (crack-like defects) on the originally smooth surface of the material in areas with high local strain amplitude. The number of PSMs containing intrusions increases with the applied plastic strain amplitude. The depth of the intrusions increases linearly with the number of cycles. The whole defect could be considered as initiated fatigue crack when the increase of the depth of the defect due to local slip irreversibility is higher than due to the deepening of the intrusion.

3.6 Chapter summary

This chapter mainly focused on characterizing the AISI 316L stainless steel. The initial step was to macroscopically analyse the material's properties through data from literature, as well as by conducting a tensile test on three specimens from the procured set. The information from this test was then used to create a testing matrix for the fatigue characterization of the material of interest, which resulted in the S-N curve showing the fatigue life of the material. The final stage of characterization was to analyse the fracture surface of the fractured specimen using SEM to confirm the damage mechanism initiation as part of the fatigue testing. It was confirmed that fatigue damage was the active mechanism that caused the fracture of the material specimen. Moreover, it was observed that room temperature fatigue testing increases dislocation density in annealed AISI316L stainless steels. This testing set the precedence for the identification of material states to be used in the microscopy analysis.

Chapter 4. Quantification of strain and crystal size per material state using powder X-Ray diffraction

4.1 Introduction

In this section, powder x-ray diffraction analysis is conducted in the form of experimental samples of the diffracted intensity as a function of 2-theta are analysis for the differing materials states as discussed in Section 3.4. Microstructural aspects, such as crystallite size, microstrain, dislocation parameters and probability of planar faults used to calculate dislocation densities in the material states.

4.2 Experimental details

Powder x-ray diffraction (PXRD) data was collected on a Bruker D2 Phaser diffractometer at the Nelson Mandela University. This diffractometer uses a flat plate sample geometry and was equipped with a Co $K\alpha_{1/2}$ radiation source and Lynxeye PSD detector operating in a pseudo-Bragg Brenano geometry mode. PXRD data were collected over a scan range from 10-140^o ($2\boldsymbol{\theta}$) with 0.01087^o step size. The instrument was operated at 30 kV and 10 mA. A brief description of the experimental details undertaken in the study is discussed in the following sections. To meet the study objectives for the extraction of microstructure parameters such as micro-strain, a profile fitting-based software, TOPAS, is utilized for microstructure analysis and crystal structure analysis. The software has supports capabilities for whole pattern fitting such as Rietveld refinement.

4.2.1 Sample Preparation and Specimen Details

PXRD data collection method ties in from the specimen preparation steps described in Section 3.4.2. To ensure the reliability and accuracy of the PXRD data, a meticulous sample preparation process was followed. Six distinct material states were selected for this study: extruded specimens, annealed specimens, and fatigue-tested specimens subjected to different cycle counts (500k, 1 million, 3 million, and 11 million cycles), as shown in Table 3.

Each material state was sectioned to obtain three 2 mm thick discs from the cross-section of the specimen. The sectioning was performed using a precision low-deformation diamond saw to minimize residual stresses and mechanical damage, which could affect the integrity of the crystallographic measurements.

Table 3: PXRD Specimen Details

Sample Designation	Sample Description	PXRD Testing
RAM280_5	Annealed	3x 2mm discs
RAM280_2	500k	3x 2mm discs
RAM280_3	1 million	3x 2mm discs
RAM280_4	3 million	3x 2mm discs
RAM280_1	11 million	3x 2mm discs
RAM280_6	Extruded	3x 2mm discs

Following sectioning, the specimens were subjected to electro-polishing to remove any mechanically induced strain and surface defects that could influence the PXRD results.

4.2.1.1 Electro-Polishing Technique and Its Impact on PXRD Accuracy

Electro-polishing was conducted using a 5% perchloric acid in ethanol electrolyte solution at -20°C for 30 seconds under controlled conditions. This method was chosen to ensure a uniform, deformation-free surface that enhances the accuracy of PXRD measurements. The key aspects of this technique and their effects on the results are detailed below:

Minimization of Surface Stresses and Strain Artifacts

- Conventional mechanical polishing can introduce residual stresses and plastic deformation, which can lead to broadening or shifting of diffraction peaks in PXRD data.
- Electro-polishing selectively removes material from the surface through anodic dissolution, ensuring that any strain introduced during cutting is completely eliminated. This results in well-defined peak positions in the PXRD pattern, enhancing phase identification accuracy.

Enhanced Surface Smoothness and Reduced Peak Broadening

- PXRD is highly sensitive to surface quality, as rough surfaces can cause diffuse scattering and peak broadening.
- Electro-polishing produces an atomically smooth surface, reducing peak broadening effects and improving the resolution of the diffraction pattern.

Prevention of Preferential Phase Removal

- Unlike mechanical polishing, which can lead to differential material removal and preferential phase exposure, electro-polishing ensures a chemically uniform removal of surface layers.
- This guarantees that the PXRD results are representative of the bulk microstructure and not influenced by surface modifications.

Reproducibility and Consistency

The use of controlled electro-polishing parameters (fixed voltage, electrolyte composition, and temperature) ensures that all specimens undergo the same surface treatment, leading to consistent and reproducible PXRD data across different samples.

To further ensure accuracy, a LaB_6 standard was included in every batch of PXRD scans. The LaB_6 standard provides a reference for instrument calibration, accounting for any systematic instrumental broadening and peak shifts. This additional step helps in quantifying the true crystallographic changes in the studied materials, rather than attributing them to instrumental errors.

By incorporating precision sectioning, electro-polishing, and instrument calibration, the sample preparation method ensures that the PXRD results accurately reflect the material's true phase composition, residual stress state, and microstructural changes due to fatigue cycling.

4.2.2 Determination of the instrumental resolution function IRF(X)

In the literature review section, section 2.4.1.1.2 raised the need for the accounting of broadening due to the instrumentation. This is typically performed by using the SRM to calculate instrument settings. To manually account for the instrument broadening, a standard sample is also analysed using the diffractometer that has zero strain or crystalline broadening. However, when using the FPA approach fitting, it should be noted that corrections for instrument broadening and peak shift are intrinsic to the refinement. There is no need for a reference specimen when an instrument is well characterised, thus line broadening can be analysed without a reference specimen (Cheary, 2004). The difference between the fatigue tested sample peaks and the peak from the standard is only due to the fatigued sample broadening. The standard should therefore contain no micro-strain broadening in accordance with the certification from NIST. For this study, Lanthanum Hexaboride Powder (LaB_6) was used as standard for instrumentation calibration. Commercial software packages such as TOPAS allows

for any user defined profile that accurately describes the physical broadening can be readily convoluted into the refinement.

There are numerous ways to account for instrumentation broadening. Ungar, 2001, did not perform any corrections in the study since the PXRD measurements were carried out by a special double-crystal diffractometer with negligible instrumental broadening. However, it is clear that in the event the instrumental effect could not be neglected, the observed line profile would be the convolution of the physical and the instrumental profiles thus the function fitted to the Fourier transform of the observed profiles would be the product of the size, the strain and the instrumental Fourier coefficients, as in a usual Stokes correction (Stokes, 1948).

Various methods were investigated to determine the instrumental resolution function IRF(X) by fitting the instrument on the LaB_6 strain-free standard with a crystallite size of 800 nm using different approaches in TOPAS. However, two widely used methods were compared in the study. The widely used method is the WH simpler method and more accurate whole pattern method based on Fundamental Parameters. In summary, method 1 fitting is performed within several variables and uses a Williamson-Hall plot technique which is prone to error in data fitting. While the second method uses the physical instrumentation and detector setting to account for the instrumentation broadening with an added quality check step as a confirmation for the accurate results verification.

4.2.2.1 Method 1 - Instrumentation Broadening Peak profiling.

In this analysis, the instrument is fitted first using the LaB_6 standard and a Pseudo-Voight (PV) number 2 (II) function. Thereafter the peak data is fitted using the same PV-II function. PVII is a Pearson function made of a combination of the Gaussian and a Lorentzian function.

The resulting instrumentation broadening from the LaB_6 standard, which is a contribution from the instrumentation broadening, is then fitted to the data and subtracted from the broadening achieved from the sample. This method was used in the study for WH plots analysis.

Instrumentation broadening peak profiling using an SRM (Standard Reference Material) LaB_6 (Lanthanum Hexaboride) standard is commonly performed in X-ray diffraction (XRD) analysis to characterize the instrumental contribution to peak broadening. This is crucial for accurate phase identification, microstructural analysis, and strain or crystallite size determination using the Scherrer equation or Williamson-Hall method. It was performed by following the steps below:

- Perform XRD measurements on the LaB_6 standard using the same instrument settings (wavelength, scan speed, divergence slit, and detector) as the sample analysis.
- Use a high-quality diffractometer with a well-aligned optical path to minimize instrumental artifacts.
- Scan over a broad 2θ range to cover multiple diffraction peaks

Perform peak profiling and instrumental broadening by:

- Fit the measured peaks of LaB_6 using profile functions such as Gaussian, Lorentzian, or Voigt.
- Determine the Full Width at Half Maximum (FWHM) for each diffraction peak.
- Generate an instrumental broadening function by plotting FWHM vs. 2θ.
- This function represents the broadening effect caused solely by the instrument.

Thereafter, a deconvolution of the sample analysis is performed by comparing the FWHM of the sample peaks with the instrumental broadening function. For advanced peak profiling, the instrumental broadening data is inputted into the Rietveld refinement software, TOPAS to refine crystal structure parameters, peak shapes, and microstructural properties.

4.2.2.2 Method 2 – Instrumentation refinement

The Fundamental Parameters as described in Section 2.4.1.1.4 was used to fit the instrument contributions. This was then fixed. Thereafter, the steel experimental data was imported into the model. Thereafter individual peaks were fitted by allowing the peak position and intensity to vary. This allows for relative lattice parameter movements and possible texturing. The next step was to refine over sample height, absorption but constrain the microstrain (isotropic broadening) and crystallite size for all the peaks.

In Bruker TOPAS, advanced peak profiling was performed using an SRM LaB_6. This process involved defining the instrumental broadening function accurately and refining peak shapes to account for physical and instrumental effects. This is critical for accurate microstructural analysis, including crystallite size and strain determination. The following steps were undertaken.

1. Collecting Data for SRM LaB_6 - Prior to peak profiling, an XRD pattern of the LaB_6 standard must be collected by using the same scan parameters as the sample (step size, scan range, slit settings,

wavelength, etc.). It was verified that the diffractometer was well-calibrated for accurate peak position and intensity measurement. Data was then collected over a broad 2θ range (e.g., 10°–150°) to capture multiple diffraction peaks.

2. Thereafter, the Instrumental Broadening Function was defined in TOPAS by modelling using a fundamental parameters approach (FPA) or an empirical function. The LaB_6 standard is used to determine:

- Gaussian and Lorentzian contributions to peak broadening.
- Instrumental resolution function (IRF), which accounts for source divergence, receiving optics, and detector effects.

The refined LaB_6 peak profile model is saved for application to unknown samples.

3. The next steps involves applying the Instrumental broadening model to sample data by using the previously determined instrumental broadening function as a fixed input. The peak profiles are refined.

4. The final steps includes a Rietveld Refinement with the SRM-Based Peak Model by performing full-profile fitting of the sample data using the LaB_6-defined instrumental function and refining microstructural parameters. Convergence by minimizing weighted R-factor (R_wp) and checking fit quality must be ensured.

5. The final steps ensures a verification by comparing the refined peak broadening with expected values. From the NIST certificate these values should be 800 nm for crystallite size and zero for microstrain as a verification of the peak phase in the software which gives confidence that the instrument has been modelled accurately, this is a form of a quality check.

This method for advanced peak profiling with LaB_6 ensures highly accurate modelling of instrumental broadening. This enhances the reliability of crystallite size and strain measurements in Rietveld refinement.

4.2.3 Determination of the micro-strain and crystallite size using WH plots

Determination of the micro-strain and crystallite size using WH-plots is performed by calculating the corrected FWHM for each material sample at each peak position. The corrected data is the FWHM after the subtraction of the instrumentation broadening. Using Equation 10, the straight-line functions for slope and intercept are used each sample to plot strain and crystallite size respectively. This section describes how the FWHM is calculated using TOPAS and thereafter, the

methodology undertaken for the Williamson-Hall (WH) plot is also discussed. The results of the two methods are compared and discussed in this chapter.

4.2.4 Determination of dislocation density per material state from the WH data

The Rietveld refinement method involves the simulation of the diffraction pattern, including the peak profiles and the background using software, see TOPAS script in Appendix A. The process of refining the pattern is computationally intensive and uses input parameters such as the lattice constants and the space group. The location and the intensity of all Miller indices *(hkl)* reflections are calculated. Thereafter, the simulated pattern is fitted to the experimental data. A refinement of the structural and the microstructural parameters is performed to a point where an accurate fit between the two patterns is made. In this study, the determination of the micro-strain (e_0 from strain) and crystallite size (D_{vol}) using whole pattern fitting, by fixing the instrumental resolution function determined by the 3rd method in Section 4.2.2 is performed. In this method, the crystallite size and micro-strain comprises of a Lorentzian and Gaussian component convolutions of diffraction peaks varying in the diffraction angle 2θ as a function of 1/cos θ and tan θ, respectively. The approach yields volume weighted mean crystallite sizes D_{Vol}-IB and a mean strain value $e_{0.}$

Initially, the emission profile for the PVII type function is modelled to determine the position of the peaks and the quantity and shape of the peaks per crystallographic plane. In this study, the emission profile utilised is specified by using pre-defined values from the software where seven parameters as shown in Table 4. These refined values are called into the software using predefined wavelengths.

The experimental pattern will always have some background, where there are no peaks in the graph, there is always some signal that needs to be modelled as part of the simulation by interpolating a straight line. In this study, the background is simulated by using the fitting functions within the software where a Chebychev polynomial to the order of 3, since the original scan raw data shows a background that is relatively smooth.

The TOPAS software makes defining the peak positions as a relatively easy process as it automatically inserts the peaks in the software. However, filtering of the peaks can be eliminated by filtering on the noise and changing the threshold and height. This is because the reflections for this steel are known, i.e. (111) (200) (220) (311); thus, adjustments on the noise levels are performed until the applicable reflections are selected. Fitting can also be done by filtering out

the $K\alpha_2$ although the software can also take into this wavelength contribution due to the emission profile assigned in step 1 discussed above by using the intensity ratio for both wavelengths.

Table 4: Analytical x-ray emission source profile for a Co node.

No.	Area	Wavelength (Å)	Lorentzian fit	Gaussian fit
1.	0.378	1.788985	0.4633522	0
2.	0.144	1.789252	0.6958819	0
3.	0.127	1.789695	1.176738	0
4.	0.088	1.788852	0.208542	0
5.	0.197	1.792791	0.4127551	0
6.	0.095	1.793064	0.7190761	0
7.	0.05	1.793474	1.157845	0

Finally, PXRD data refinement is performed using three parameters, namely, the peak shift, the Intensity (peak height) and the FWHM (peak width) for each peak. The peak shift can be because of the sample height (zero off-set). In TOPAS, once peaks have been inserted, a peak phase, defining a list for each of the peak positions relative to the peaks that have been sourced from the scanned raw data is available. Each of the peaks identified are not dependent on each other and they are essentially free to move. A TOPAS script has been included in Appendix A of this dissertation based on the analysis that has been performed. The final steps entail the calculation of the dislocation density using the formula that takes the micro-strain and crystallite size into account.

4.3 PXRD Measurement Results

4.3.1 Instrumentation broadening results.

The diffracted raw data from the LaB_6 phase is shown in **Error! Reference source not found.**. The FWHM observed in the diffraction pattern of LaB_6 was assumed to be as a result of the instrumentation contribution only because there is no intrinsic broadening for this phase.

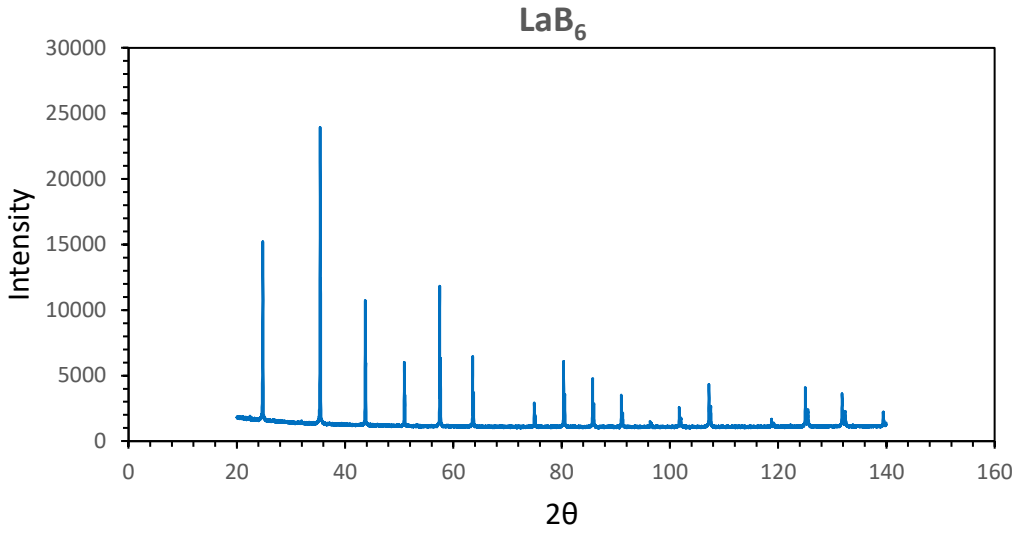

Figure 18: Graph of LaB6 TOPAS Refinement showing the raw diffracted data from the LaB_6 standard.

The raw diffraction data from Table 5 was plotted as a function of peak position (2θ) and shown in Figure 19. A second order parabola is fitted through the data points and the resulting equation of the plotted line was used to calculate the FWHM at the crystalline peak positions. Table 6 shows the calculated FHWM.

From the graph, it was observed that the experimental data is comparable to the fitted data and typically, of x-ray diffraction diffractometers, it was evident that broadening due to the instrument increases with increasing 2 theta positions. This may be due to a number of factors which are not part of the scope for this study.

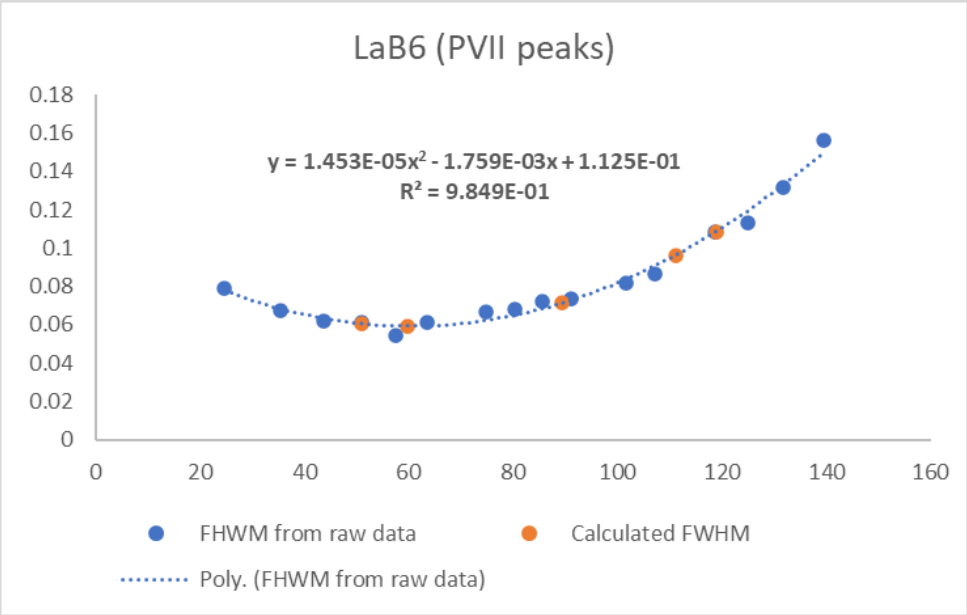

Figure 19: Graph showing the calculated FWHM from the LaB_6 raw data peak positions as a function of 2-theta value.

A comparison of the calculated FWHM values with the experimental data, as shown in Figure 19, demonstrated a close correlation, which was accepted. Furthermore, from the graph, it was observed that the broadening of the instrument increased with the 2-theta peak position.

Table 5: Calculated FWHM from raw diffraction in relation to 2 theta peak position

Item	Position	FWHM
1	24.79216	0.07882
2	35.38206	0.06717
3	43.71873	0.06193
4	50.93759	0.06092
5	57.4807	0.05424
6	63.57746	0.06102
7	74.94379	0.06681
8	80.3784	0.06785
9	85.72707	0.07243
10	91.03942	0.07345
11	101.7383	0.08173
12	107.2245	0.08641
13	118.7831	0.10828
14	125.0402	0.11342
15	131.8252	0.13162
16	139.4272	0.15623

Table 6: Instrumentation broadening values at AISI 316L stainless steel peak positions.

Angle	Instrument
51.1	0.0604776
59.7	0.059167
89.5	0.0712181
111.1	0.0960516
119	0.1085135

4.3.2 Williamson-Hall (WH) plot analysis

Crystal imperfections gave a broadening effect on the diffraction peak. Size and strain had different contributions to line broadening. Using a WH plot, the crystallite size and micro-strain values for each of the peaks were shown in Appendix B, while Figure 20 showed the resulting combined WH plot.

The WH plot translated the results from the straight-line equation displayed in Figure 20. The slope depicted the micro-strain component, while the y-intercept depicted the crystallite size. It was observed that the data points did not lie on a straight line, which showed that the different peaks did not broaden to the same extent. Thus, there was anisotropic broadening in the sample. The annealed specimen had the lowest micro-strain, while the extruded specimen showed the highest strain. This was in good agreement with the material state, as there should have been no deformation in the material sample. The fatigued specimen, however, showed inconsistent micro-strain results that did not align with the sample material state.

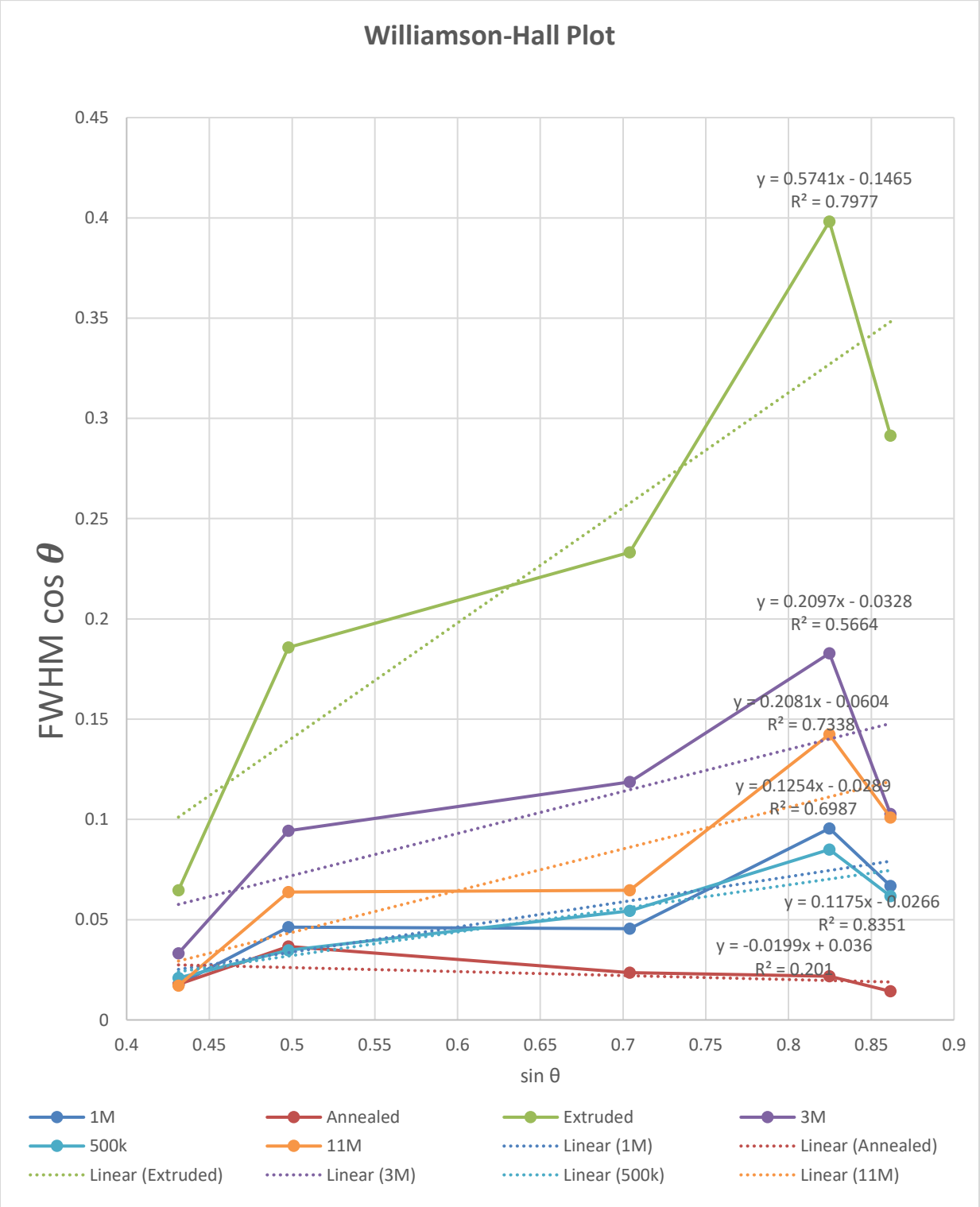

Figure 20: WH Plot for all material states with averages FHWM cosθ.

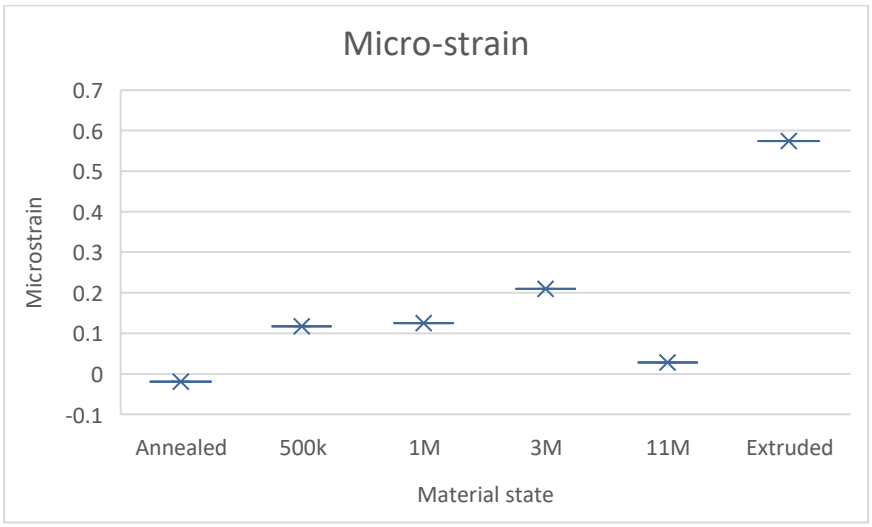

Figure 21: Micro-strain data for each material state calculated using WH method.

The overall results per material state were summarised in box plots shown in Figure 21 for the micro-strain. In general, the micro-strains for the annealed and as-received specimens were vastly different. As discussed above, the micro-strains for the lower fatigued specimens, i.e., 500k and 1 million cycles, on average, showed marginal increases between specimens in line with the levels of fatigue cycles.

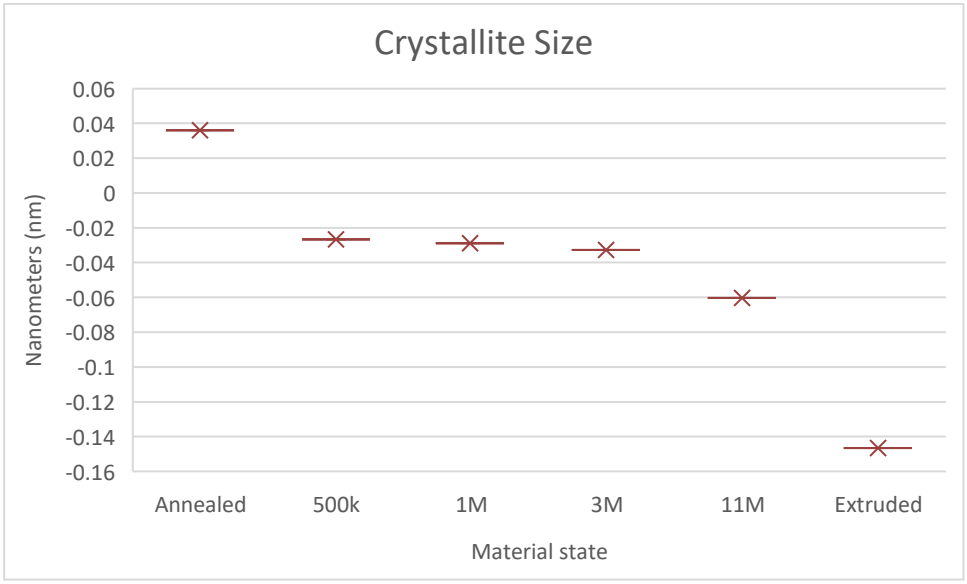

Figure 22: Crystal size data for each material state calculated using WH method.

However, overlaps between various samples were evident. The 11-million-cycled specimen showed results that were very low in comparison to the other fatigued specimens. This finding was discussed in Section 4.4.2. However, in brief, the 11-million-cycled, specimen yielded micro-strain results much lower than the 500k, 1M and 3M fatigue-cycled specimens due to the crystallite size distribution as well as anisotropic broadening.

Figure 22 showed the crystallite size data for each material state calculated using the WH method. It was observed that the annealed specimen contained large crystallites, while the rest of the crystallite sizes were small and overlapped. A qualitative evaluation showed that the lower cycled specimens had smaller crystallite sizes. However, the crystallite sizes of these specimens were comparable.

Table 7 provided a summary of the WH plot analysis for the micro-strain and crystallite sizes of the different specimens, sourced from the averages of the FWHM data. It was clearly evident that there was an overlap between the minimum and maximum values for strain between the material states. Similarly, an overlap between the crystallite sizes was also observed.

In the WH method, there were a number of approximations:

- Limitations in representing the instrument contributions in the WH method resulted in errors.
- These samples all had relatively large (>150 nm) crystallite sizes, so the broadening contribution from crystallite size was very small.
- Small contributions—values with a large error—resulted in negative values.
- If the material had been nano-sized (<50 nm), then the peaks would have broadened out more due to crystallite size, but this was not the case for our samples.

Table 7: PXRD refinement results using WH plot analysis.

Sample	Straight Line Formula	Slope (Strain)	Y-intercept (Crystallite size in nm)
Annealed	y =-0.0199x+0.036	-0.0199	0.036
500k	y = 0.1175x-0.0266	0.1175	-0.0266
1M	y = 0.1254x-0.0289	0.1254	-0.0289
3M	y = 0.2097x-0.0328	0.2097	-0.0328
11M	y = 0.2081x-0.0604	0.02081	-0.0604
Extruded	y = 0.5741x-0.1465	0.5741	-0.1465

4.3.3 Raw results analysis – Broadening of peaks

Figure 23 shows an PXRD plot of all material states with peaks broadened at the relevant Bragg angles of 51.1°; 59.7°; 89,5°; 111.1° and 119° with the corresponding miller indices (*hkl*) shown in the spectrum. The intensity was strong for the first peak (111), and decreased with Bragg angle due to the atomic scattering factor of x-rays.

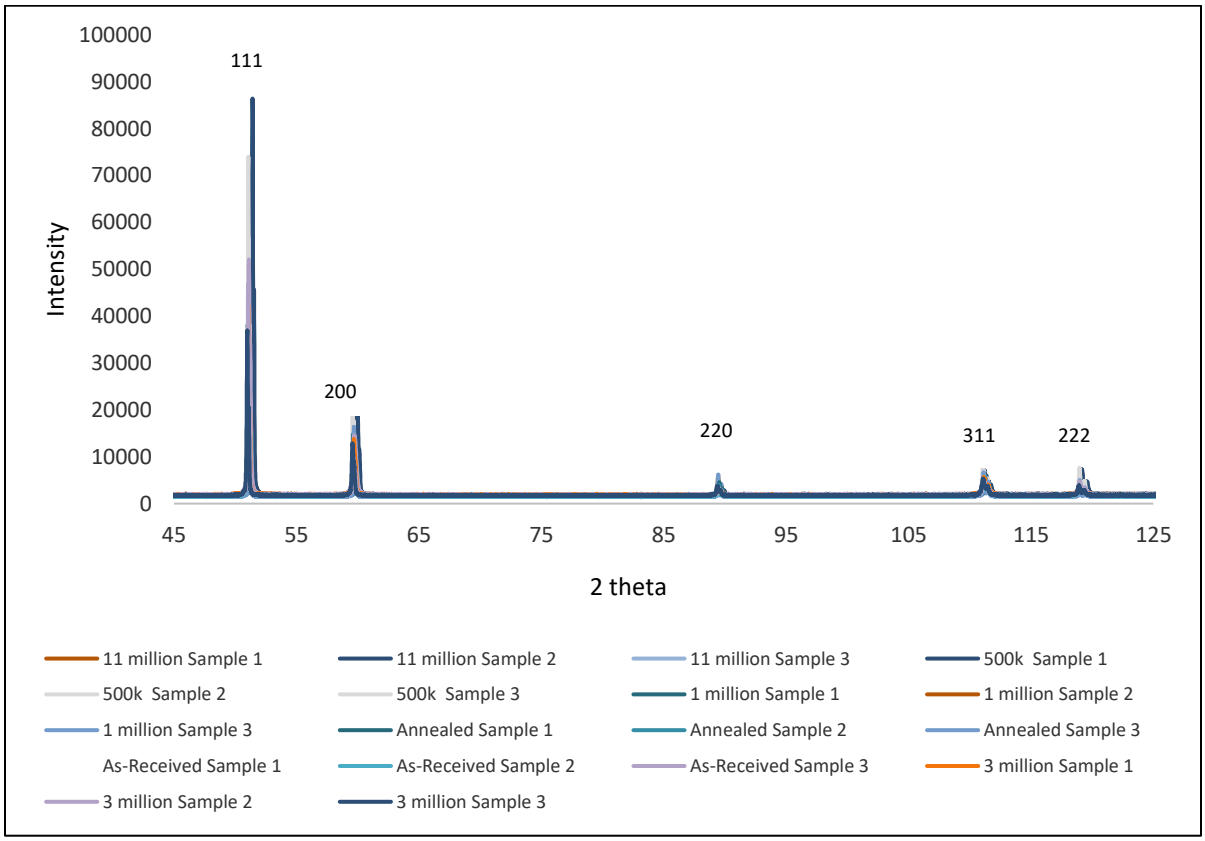

Figure 23: PXRD plot of all material states

4.3.3.1 Overall sample analysis for plane (111)

The raw data results of the material states at a Bragg angle of approximately 51° were shown in Figure 24. All peaks exhibited a characteristic profile with Kα1 and Kα2 overlapping each other. The intensity of each peak also differed, even for samples fatigued to the same level of stress. Although the profile shape was a common peak doublet with a combination of a Gaussian and a Lorentzian profile shape for all peaks, it was apparent that the peak widths and peak positions were different for the various samples. This was also true for samples with the same fatigue level. Additionally, each sample in the group had a varying intensity level.

The anomalies observed were attributed to operator error, such as differences in sample height. To eliminate this issue, Section 7.2 discussed the measurement protocol based on these observations. Furthermore, this was corrected in the Rietveld analysis.

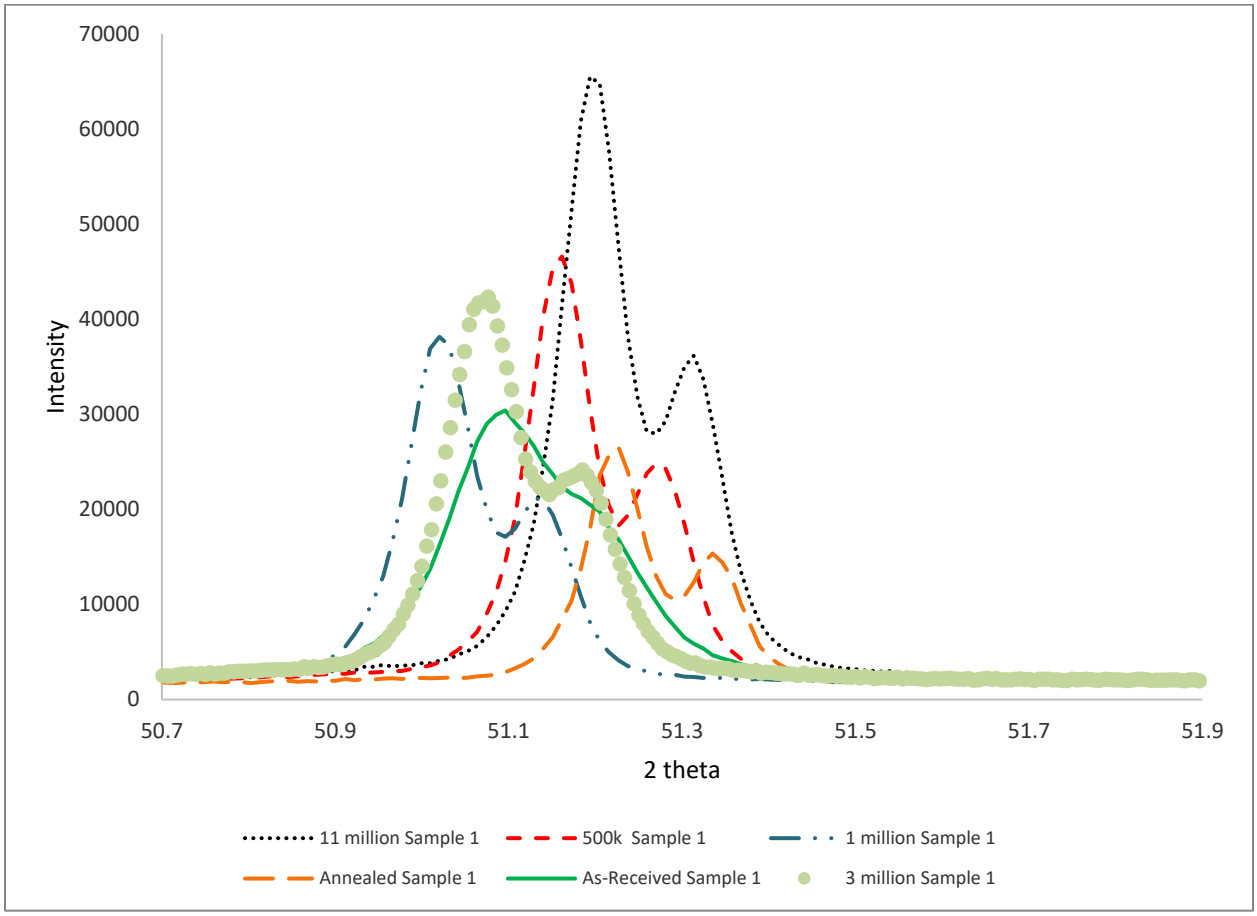

Figure 24: Image showing (111) peak broadening for all material states.

This observation was attributed to size and strain broadening, which could be differentiated by their different dependencies on the diffraction angle. The differences in peak positions were primarily due to non-homogeneous deformation. Isotropic broadening was assumed; however, the deviations in the WH plots for the different samples clearly demonstrated that the different peaks did not broaden isotropically. This meant that the different planes had varying amounts of broadening, which altered the peak intensities. Depending on the original texturing and the loading directions, some grains might have been favourably oriented for deformation and experienced higher levels of dislocation formation. The relative peak positions observed changed for the different samples, with the effect being more pronounced in the highly deformed samples.

In size broadening, the crystallites within a sample generally did not all have the same size, even if they should have had the same geometric shape. Instead, they typically exhibited a size distribution, which could be narrow or broad, symmetric or asymmetric, and monomodal or polymodal.

PXRD thus provided a mean value for size properties as a result of the size distribution characteristic. Size broadening analysis was most effective in the range of several tens to several hundreds of Å. In the upper size range, the total peak width became dominated by instrumental broadening, making the precise extraction of sample-related broadening increasingly difficult. In the lower size range, the contribution of the instrument function was negligible. The broadness of the peaks caused strong baseline ambiguity, which, in combination with the flat slope of the peak flanks, made peak width determination increasingly imprecise. Crystallite size broadening was proportional to $1/\cos\theta$ (Girgsdies, 2006).

For strain broadening, the micro-strain was a local deviation of d-spacings from the average value, caused by local defects. These defects, such as dislocations, had a size differing from that of the regular atoms in the lattice, resulting in the contraction or expansion of d-spacings around the defect. Typically, the forces of compression and expansion balanced out, leading to diffraction peak broadening instead of a peak shift. This contrasted with macro-strain, or stress, which was directional and thus caused peak shifts depending on the relationship between the diffraction vector and the strain vector.

An image showing the lower cycled specimens (i.e., 500k, 1 million, and 3 million cycles) was presented in Figure 25. The shape of the 3-million-cycled specimen was more broadened out and consistent across all three samples; however, samples 1 and 2 were shifted towards the right. The 500k specimens were narrower, with sample 2 exhibiting the highest intensity. The 1-million-cycled specimens were positioned between the 500k and 3-million-cycled specimens. However, there was a general overlap (noise) in the broadening among all the material specimens.

Figure 26 showed the PXRD results for the (111) peak, comparing the as-received, annealed, and 11-million-cycled specimens. The annealed specimen profile was generally flat with very low intensity. The extruded specimen profile had the Kα1 and Kα2 overlapping to form a single peak profile, while the 11-million-cycled specimens were sufficiently broadened out, with the Kα1 and Kα2 wavelength profiles clearly distinguishable. Sample 2 of the 11-million-cycled specimen was shifted further to the right in comparison to all the other material specimens. The difference in behaviour between samples of the same type of specimen (i.e., the 11M material state) was once

again attributed to anisotropic broadening. It was possible that there were variances within the same sample of a specimen. Additionally, peak positions could have been shifted due to variations in sample height, which were influenced by how the sample was loaded into the diffractometer.

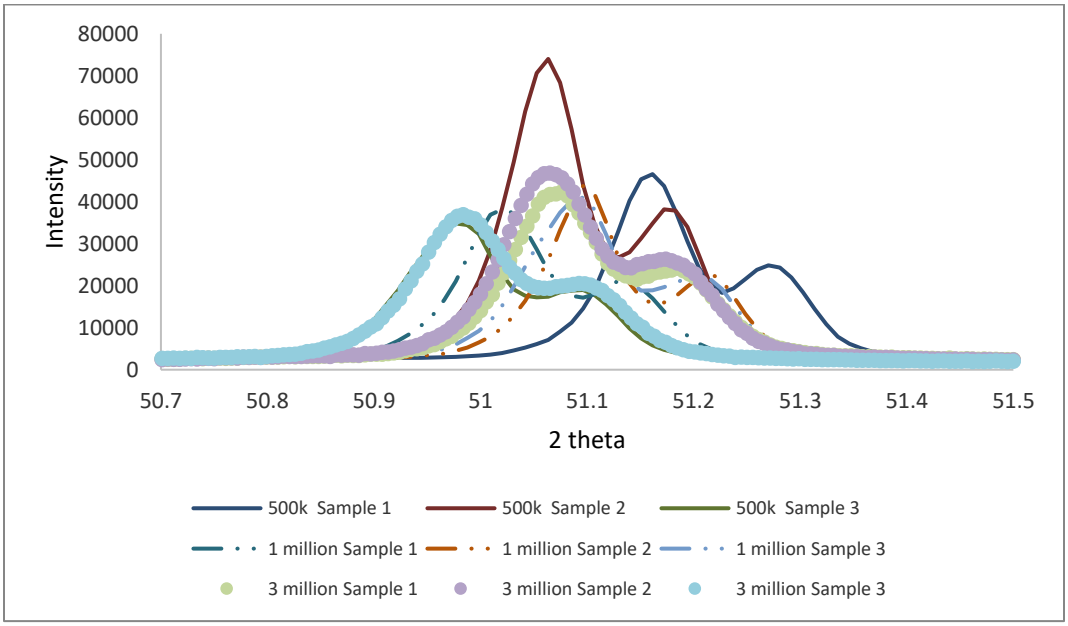

Figure 25: Lower cycled specimen at (111) peak spacing.

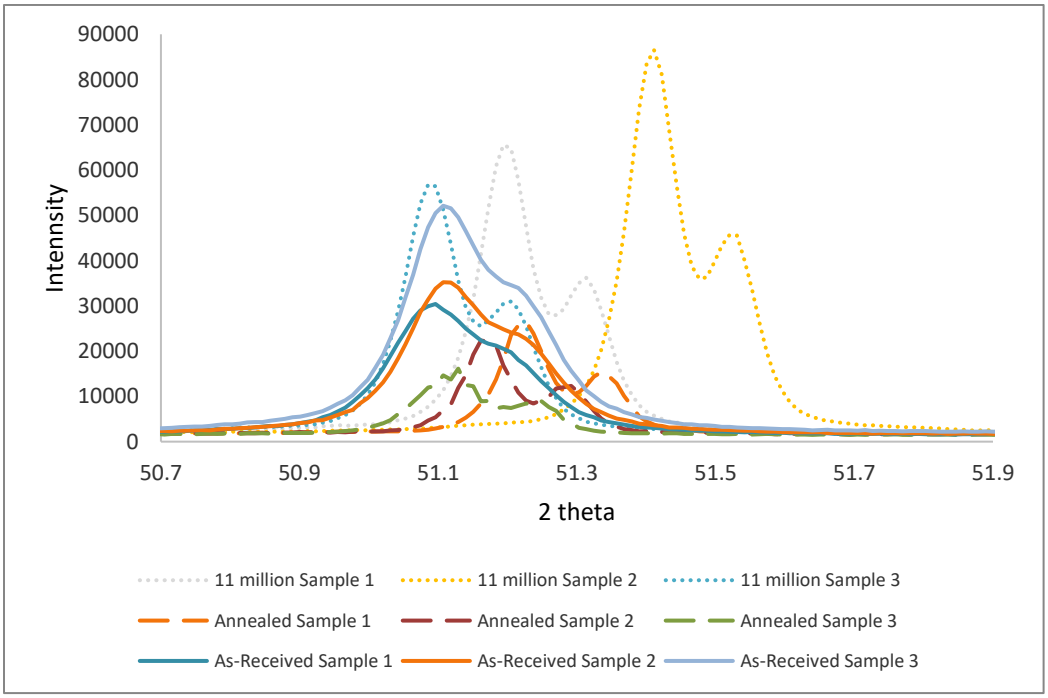

Figure 26: Annealed, extruded and 11 million cycled specimen at (111) peak spacing.

4.3.4 Rietveld Refinement using TOPAS fitting analysis.

4.3.4.1 Micro-strain Results

Table 8 presented the microstrain (e_0 from strain), the crystallite size (Dvol-IB), and the associated residual weighted profile (RWP) for all samples per material state. This data was calculated using method 3, as described in Section 4.2.2.3. The data was graphically represented in Figures 27 and 28 to illustrate the distribution of the parameters per material state. The RWP value indicated the accuracy of the fit. This measure was used as a weighting function to place more emphasis on a good fit between high-intensity data points, such as intense peaks, and less emphasis on low-intensity data points, such as background. In a good fit, RWP was expected to be less than 10. The factors shown in the table below depicted relatively low fit values for all samples.

Table 8: Method 3 PXRD refinement results showing e_0 from strain for the micro-strain and D_{vol}-IB for crystallite size in nm after electro-polishing of all material state samples.

Description	e_0_from_strain	D_{vol}-IB (nm)	RWP
Extruded – Sample 1	0.00043± 0.0001	87.89±10	4.06377638
Extruded – Sample 2	0.00039± 0.0001	90.42±10	4.19578481
Extruded – Sample 3	0.00039± 0.0001	95.11±10	4.13565639
Annealed – Sample 1	0.00010± 0.0001	279.26±10	2.90070586
Annealed – Sample 2	0.00009± 0.0001	294.49±10	2.75200777
Annealed – Sample 3	0.00002± 0.0001	228.76±10	3.06412574
500 000 cycles – Sample 1	0.00016± 0.0001	272.79±10	2.77238787
500 000 cycles – Sample 2	0.00014± 0.0001	315.13±10	2.7549345
500 000 cycles – Sample 3	0.00016± 0.0001	250.58±10	2.52808046
1 million cycles – Sample 1	0.00015± 0.0001	250.37±10	2.89046873
1 million cycles – Sample 2	0.00016± 0.0001	305.39±10	2.92241245
1 million cycles – Sample 3	0.00014± 0.0001	297.03±10	2.76353846
3 million cycles – Sample 1	0.00028± 0.0001	210.77±10	3.15771811
3 million cycles – Sample 2	0.00025± 0.0001	200.08±10	2.93168553
3 million cycles – Sample 3	0.00025± 0.0001	216.64±10	3.22397708
11 million cycles – Sample 1	0.00020± 0.0001	231.02±10	3.7162596
11 million cycles – Sample 2	0.00018± 0.0001	247.35±10	4.08307793
11 million cycles – Sample 3	0.00021± 0.0001	237.83±10	3.27272627

Figure 27 plotted the microstrain values per material state in a box plot. There were notable differences between the microstrains of the annealed and the extruded specimens. This result was expected since the as-received specimen had higher levels of deformation within the

microstructure. The microstrain in the annealed condition was very low and close to zero. This was well within the characteristic of the material state, as the annealing process stress-relieved the microstructure to a point where there should have been very little or no deformation. The fatigued specimens, however, showed an increase in microstrain within the microstructure.

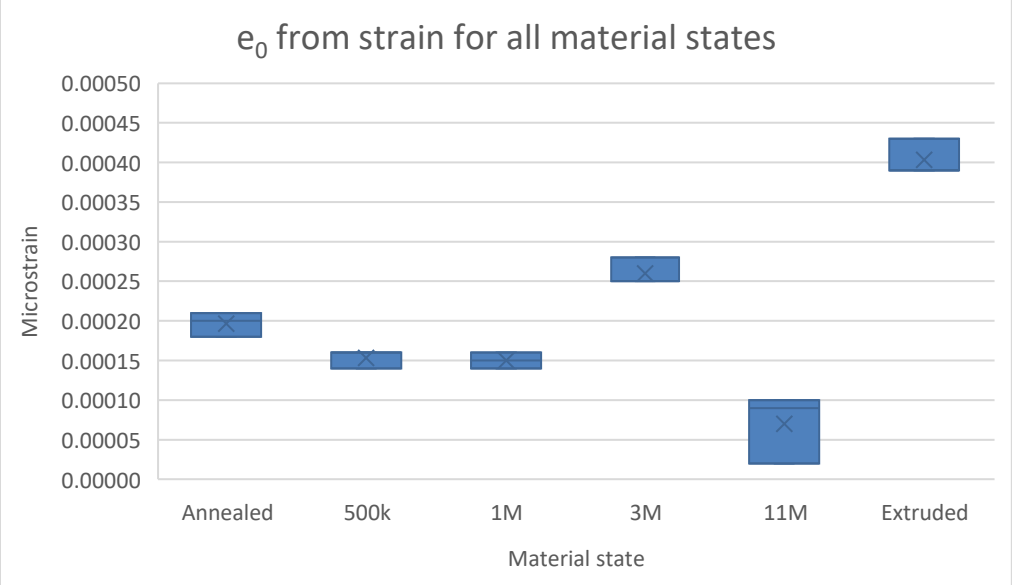

Figure 27: Micro-strain data for each material state

The level of deformation within each family of material states increased steadily from the lower cycled specimen to the higher cycled specimen. Furthermore, an overlap was evident between the 500k and the 1 million cycled specimens. The 3 million cycled specimen exhibited a higher level of deformation than the 11 million cycled specimen. This was contradictory to the level of damage expected in the sample in comparison to the 3 million cycled specimen.

4.3.4.2 Crystallite Size Results

Figure 28 showed the software-calculated Dvol-IB, which represented the crystal size per material state. All results indicated that the higher the microstrain in the sample, the lower the crystalline size. The extruded specimen exhibited lower crystal sizes in comparison to all the material states. Additionally, the overall crystal sizes for the annealed and fatigued specimens increased according to the level of damage in the material, with the 3 million cycled specimen being an exception. However, there was a very large variation in the data for the annealed specimen and the very low-cycled specimen.

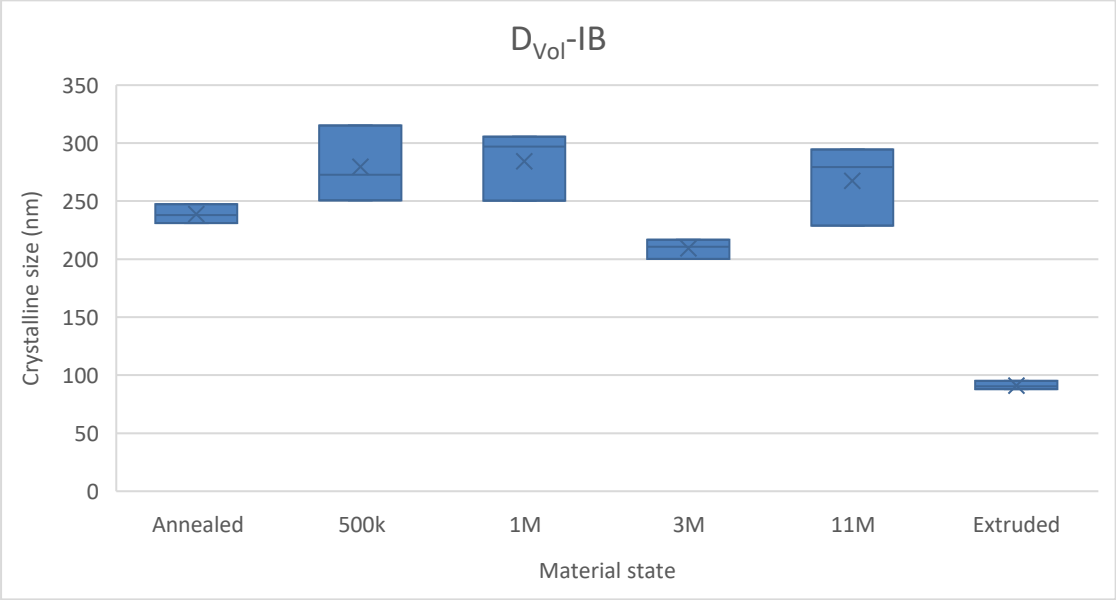

Figure 27: Crystal size data for each material strain

4.3.5 Dislocation Density Calculation

Dislocation density measurements can be performed using computational and modelling procedures developed in order to obtain microstructure parameters. This can be directly related to the quantities obtained by more direct methods, especially SEM and TEM. As previously discussed, the evaluation can either be carried out by using characteristic parameters of individual peak profiles, the FWHM, the integral breadths and the Fourier coefficients, or all measured profiles can be described by two ab initio fundamental functions: the size and the strain functions. Ungar, 2015 used a set of equations to calculate the dislocation density from the ab initio size and strain functions which can be scaled by the dislocation contrast factors using the Burgers vector and good correlation with microstructure parameters obtained by SEM and TEM was established.

Using this equation, the results shown in Figure 29 indicated that the extruded specimen had the highest dislocation density in its microstructure in comparison to all the material states. The other material states' dislocation densities followed the level of strain within the microstructure,

except for the 3 million specimen, which showed dislocation density levels higher than the 11 million cycled specimen.

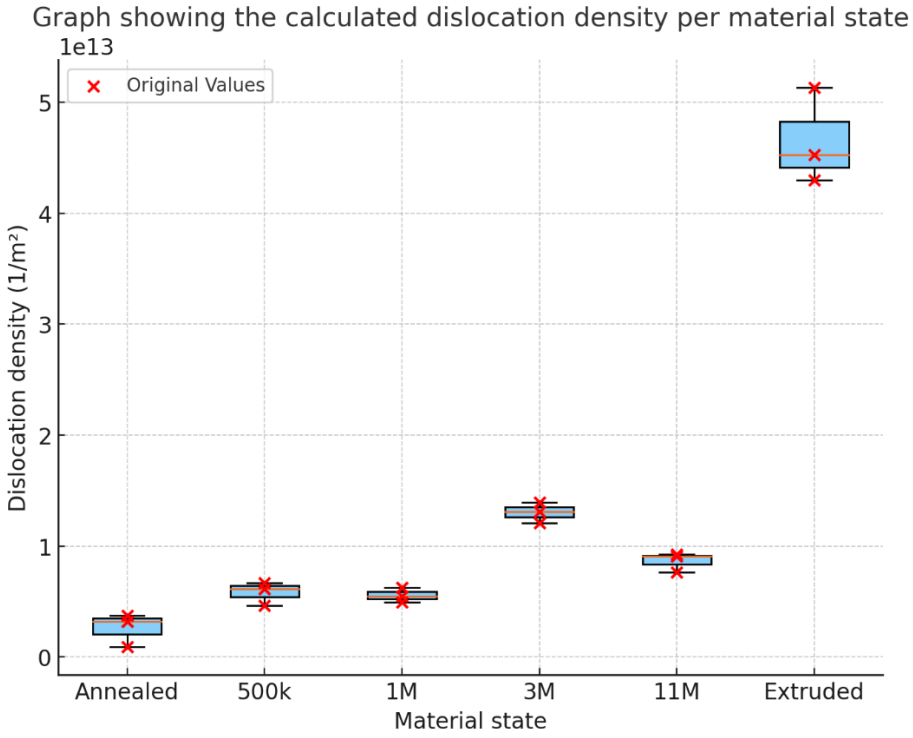

Figure 28: Dislocation density results per material state using Equation 11.

4.4 Discussion

A common feature in the diffraction patterns presented above shows that as the angle of diffraction increases, there is a decrease in the intensity of the diffraction peaks. This is mainly due to some of the x-rays being absorbed by the sample when x-rays are diffracted by atoms that are deeper within the crystal. The difference between the scattered and incident wave momentum, location, and the perturbation potential brought on by the X-ray determine the square of the structural factor, which determines the strength of the peaks. It is necessary for the difference between the incident and dispersed waves to equal a reciprocal lattice vector, which is sometimes referred to as the "Bragg condition" or "Laue condition." Consequently, the amplitude of the peaks will be less as theta grows because the d-spacing will decrease and there will be fewer spaced planes, which will reduce perturbation. The next sections discuss the results based on the methodology followed and material states comparison.

4.4.1 Instrumentation modelling analysis

Method 1 is the least constrained method. The second method assumes isotropic broadening of all peaks and uses empirical fitting. A level of parameter constraint is applied for crystalline size and Gaussian strain. The software then calculates the resulting crystal size and strain. Conversely, Method 3 allows for some flexibility in the positioning of the peaks where Gaussian functions are fitted to the experimental data, and more flexibility is permitted in the previous method. However, isotropic broadening is still assumed. In method 4, there is no flexibility to model the experimental data as the input is a crystal structure with definite lattice parameters, leading to predetermined peak broadening. Hence, it is assumed that there is an isotropic broadening of the peaks; however, this is not the actual cause. If this assumption is incorporated in the modelling, a good fit of the data will remain elusive. This is on the basis that well tried out methods such as the WH-plots and whole pattern fitting were applied to measure dislocation density each with its own limitations discussed in Section 2.4.1.1.4.

4.4.2 Qualitative evaluation of the micro strain for the material states

Figure 29 shows a box plot of the micro strain values obtained using the WH plot analysis as well as those obtained using the Rietveld refinement software, TOPAS. Qualitatively, there is good agreement between the two methods in ranking of material states according to the level of micro strain. The extruded specimen contains higher micro strain, however, there is more scatter between samples in using the WH plot analysis. In fact, this is more common across all material states where is a variation between the minimum and maximum values of micro-strain. Conversely, there is lesser micro strain in the annealed material specimen with more scatter observed in the WH plot data. For the fatigued specimens, there exists consistency between the two methodologies undertaken with the exception of the 3 million cycled specimen. In this scenario, the micro strain in this specimen ranks higher that the micro strain in the 11 million cycled specimen only in the TOPAS analysis whereas in general, there tends to be noise between the cycled specimen and thus it is difficult to qualitatively rank the level of fatigue using either method. The reasons for differences in this observation is attributed to the anisotropic of the fatigue specimen as well as the crystallite size distribution.

During fatigue testing, certain areas in the microstructure will tend to deform more than other areas. This is due to the non-identical volumes in the microstructure with different propensities towards dislocation generation and dislocation movement. With increasing fatigue testing, there will be more dislocation densities and pileups. Therefore, depending on the area of section that

is analysed, different views may be evident. This fatigued microstructure will always yield a heterogenous view of deformation within specific samples, especially in the early stages. This effect is known as strain anisotropy. Strain anisotropy has been realised where in the PXRD analysis methods including the Williamson–Hall plot method, it was noted that in a significant number of experiments when FWHM data plotted versus $K = 2 \sin \theta/\lambda$, where θ is the diffraction angle and λ is the wavelength of X-rays with the aim of giving the crystallite size parameters do not follow smooth curves (Ungar, 2001). To counter strain anisotropy scaling, the FWHM to ensure reliable determination of the size parameters by the dislocation model was performed.

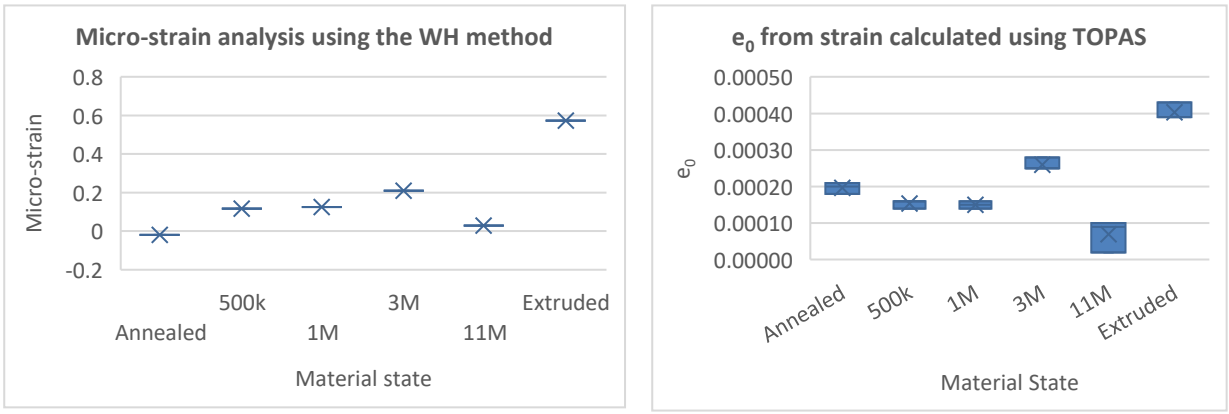

Figure 29: A qualitative comparison of micro-strain data using the WH plot analysis method versus a whole pattern fitting method in TOPAS software.

Even though the micro strain results for the annealed specimen are different using the WH plot method in comparison to the Rietveld method, the value of micro strain is close to zero. This is because the dislocations in annealed metals are arranged in a fairly random fashion, each dislocation forming the edge of a mosaic block and producing the tilt necessary to make them reflect incoherently. In case of undeformed materials with low level of strain, the grain sizes resultant from different PXRD analysis methods can be near the same.

In the study for nanocrystalline FCC metals, it was evident that the ability of available X-Ray diffraction analysis methods to consider the effects of various lattice defects on the shape and broadening of the diffraction peaks are different which impacts the resultant crystallite size and dislocation density. The accuracy of the results was largely based on the accuracy with which the microstructural characteristics are calculated.

4.4.3 Crystallite size distribution

The crystallite size results obtained using TOPAS and using WH plot analysis are shown in Figure 30. The TOPAS results indicate that the extruded specimen has the smallest crystallite size, followed by the 3 million and the 11 million cycled specimens. The remaining specimen crystalline size are in the same ballpark. In the WH analysis method, the annealed specimen shows larger crystalline while, while the lower cycled specimen (i.e., 500k, 1 mil and 3 mil) are in the same ballpark and the extruded specimen contains the lowest crystallite sizes.

These results, particularly the WH plot analysis indicate the magnitude of the crystallite size is dependent on the micro-strain level. In the range of nanoparticles, less than the 100nm, appreciable broadening of PXRD the peak is observed. In such instances, it is observed that as the peaks are broadened, and the crystallite sizes can be extracted easily from the peaks. In fact, the peaks are so dominant such that one can use the Scherrer equation to calculate the crystallite size. As the crystallite sizes increases to above 100nm, there is little size contribution in terms of broadening the peaks out. Between 200-700nm, there is very little difference in the broadening and there exists a degree of difficulty in measuring the FWHM, thus the results are sensitive to how the peaks are fitted. AISI 316L, has crystallite sizes in the order of 200nm, in this range, the contribution to the FHWM for crystallite sizes is quite low. These values attained in this analysis are false due to the rudimentary way the instrumental contribution is subtracted. However, in a TOPAS fitting which is more sensitive in the way it accounts for instrumental broadening and the crystallite size contributions, then the values may be believable.

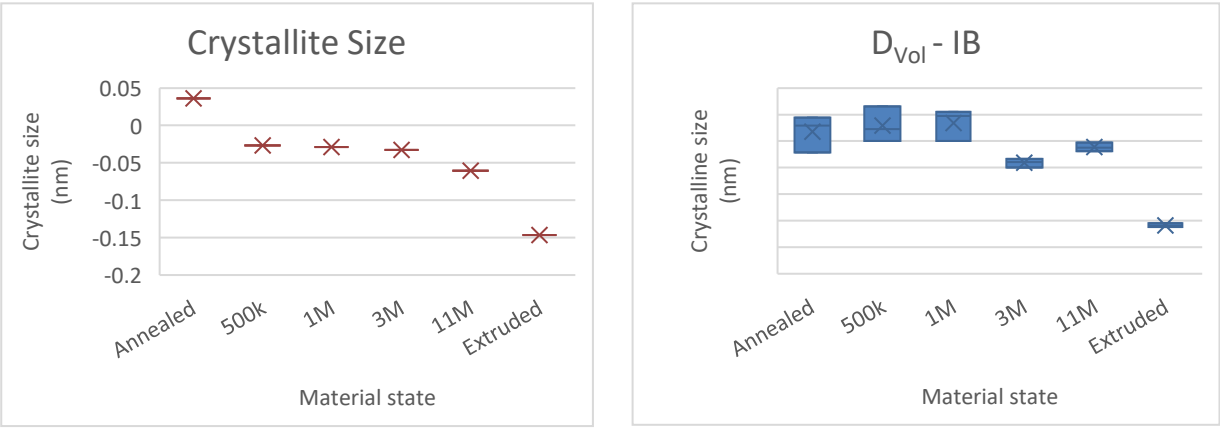

Figure 30: A qualitative comparison of crystal size data using the WH plot analysis method and whole pitting method using TOPAS software

The principle of modelling powder patterns by means of pattern simulation was based on theoretical considerations and the assumption that the crystallites had a particular shape, and on average, the distribution of size could be expressed analytically (J. I. Langford, 2000). Crystallite shapes could be narrow or broad, symmetric (i.e., normal distribution) or asymmetric (i.e., lognormal distribution), and could be monomodal or polymodal. The presence of a size distribution implied that integral methods like PXRD would usually provide some mean value of size. During analysis, a weighting scheme was applied, and most methods of PXRD size analysis yielded volume-weighted average values, while some provided area-weighted means.

Ungar (2001) applied different methodologies to determine size parameters using FWHM (WH plot) and the Fourier transform (Rietveld refinement). In the former, crystallite size distribution was determined either from the apparent size parameters, corresponding to the FWHM. However, this method assumed a spherical shape and log-normal size distribution of the crystallites. Although the apparent size parameter had no direct physical meaning, its inclusion in the determination of the crystallite size distribution reduced the sensitivity of the procedure to the accuracy of background determination. The Fourier transform of the theoretical size profiles was derived in a closed form, enabling a convenient and fast fitting procedure. The procedure was dependent on the shape of crystallites and the absence of stacking faults, where the microstructures were characterized by a number of fitting parameters.

4.4.4 Dislocation density accuracy

Two parameters, micro-strain and crystalline volume, derived from the whole pattern fitting analysis, were used in the Williamson-Smallman equation (Equation 11) to calculate dislocation densities for different material states. The limitations and approximations of the physical models for peak profile fitting and instrument constraints may influence the calculated dislocation density values. Using this equation, the box plot below (Figure 29) presents the distribution of dislocation density for different fatigue states (Annealed, 500k, 1M, 3M, 11M, and Extruded). The box plot effectively visualizes the distribution and variability of dislocation densities across different fatigue states. The trend suggests an increase in dislocation density with higher fatigue cycles, particularly in the Extruded material, which exhibits the highest overall values. This reinforces the understanding that fatigue-induced microstructural evolution plays a crucial role in material performance. Each box represents the interquartile range (IQR) (the middle 50% of the data), with whiskers indicating the overall spread. The red markers overlaying the boxes

represent the original data points. The key observations that can be derived from this data is that there is variation across fatigue states as follows:

- The annealed and 11M states exhibit relatively lower dislocation densities compared to the extruded state, which has the highest density.
- As fatigue cycles increase (e.g., from 500k to 3M), the dislocation density generally increases, indicating strain hardening effects.

In addition, the spread of data is evident as can be summarised below:

- The extruded state has the largest spread, reflecting significant variation in dislocation density.
- The 3M and 1M states show more compact distributions, indicating relatively stable dislocation densities within these fatigue cycles.
- The annealed state exhibits a noticeable spread, likely due to structural changes during fatigue exposure.

The medians (represented by the horizontal lines inside the boxes) vary across fatigue states, suggesting progressive structural changes in the material. In some states (500k and 3M), the data points are relatively close, indicating consistency in dislocation density within these conditions. No extreme outliers are observed, suggesting that all values fall within reasonable expected variations for each fatigue condition.

It can therefore be concluded that the box plot effectively visualises the distribution and variability of dislocation densities across different fatigue states. The trend suggests an increase in dislocation density with higher fatigue cycles, particularly in the extruded material, which exhibits the highest overall values. This reinforces the understanding that fatigue-induced microstructural evolution plays a crucial role in material performance.

4.5 Chapter summary

The main aim of this chapter was the quantification of deformation for the chosen material states in this study, as defined in Section 3.4, using the X-ray diffraction technique. The differing material states were made from AISI 316L stainless steel. In this instance, the specimens at differing material states were subjected to the same technique; the differences in the diffracted X-ray intensities were then compared to quantify the amount of deformation as well as the

crystallite size that resulted from the initial material state. Two X-ray diffraction analysis methods were developed to study the microstructural aspects, such as crystallite size, micro-strain, and dislocation density. The Williamson-Hall (WH) method was one of the most extensively used methods, where the size and strain broadenings in each peak could be separated. Another widely used method, named Rietveld refinement, refined and extracted structural parameters like lattice constants and the positions of atoms in the lattice using a software package, TOPAS, which simultaneously evaluated the structural and microstructural parameters.

Prior to calculating the micro-strain for all specimens, an important evaluation of the instrumentation broadening was required. The determination of the instrumental resolution function IRF(X) was performed by fitting the instrument on the LaB6 strain-free standard using different approaches, as detailed in Section 4.2.2.

The results analysis indicated that although both methods could sufficiently differentiate the level of deformation as well as calculate the crystallite sizes in the material specimens, they were not without limitations. This was because the accuracy of the results was sensitive to the fitting and sample preparation methods applied. The methods assumed that there was isotropic broadening in the microstructure of the material. However, important variables that determined the spread of values (crystallite size and micro-strain) of the results were as follows:

1. Sample preparation had to result in defect-free specimens of the same sizes.
2. Instrument setup had to remain the same and be tested with LaB6 each time a new batch of samples was scanned as an experimental calibration for each batch of runs. This experimental calibration check was then refined using the instrument resolution function defined previously and verified to ensure that the micro-strain (0.0000) and crystallite size (800 nm) corresponded to the calibration certificate.
3. The TOPAS refinement was scripted to ensure each refinement started with the same initial values. Different starting values could result in different local minima during least-squares fitting. The scripting also minimized operator error, making the process faster and more reproducible.

Finally, dislocation density calculations were performed based on the mathematical averages of crystallite size and micro-strain, as applied in the Williamson-Smallman (WS) equation. In general, observations made in this study suggested that this technique was not dependable for detecting small increments in accumulated fatigue damage to monitor damage over a period of operating life.

Chapter 5. Quantitative dislocation density analysis using EBSD grain misorientation techniques.

5.1 Introduction

The ability to identify and understand the deformation occurring around high strain gradient microstructural features is crucial in studying damage mechanisms such as fatigue damage. (Brewer LN, 2006). In this study, electron back-scattered diffraction is the selected technique is utilised to visualise plastic deformation. This technique is only used for qualitative analysis in this study to compare with PXRD. The latter being the main topic for this dissertation. Thus, the discussion presented in this chapter will not consider the advantages and disadvantages of the EBSD technique. The analysis of the technique involves using algorithm maps sourced from METX to quantify the scalar misorientation between a local minimum misorientation reference pixel and every other pixel within an individual grain. Multiple EBSD mapping algorithms were then applied to deformation distributions on montage data and broken-down fields that form a montage, to perform a comprehensive analysis. Several algorithms for EBSD mapping were then applied to the deformation distributions on montage data and broken-down fields that form a montage for an in-depth analysis.

Post the fatigue testing, selected specimen regions of interest were analysed to quantify the extent of deformation in relation to increasing levels of fatigue. This was done by tracking and investigating strain-induced misorientation evolution, lattice rotation, twinning and phase instability. The resulting images qualitatively compare the deformation in the sample. Quantitative evaluation of the deformation has not been performed. Misorientation is an orientation defined with another crystal orientation frame as reference instead of the sample reference frame. Thus, a misorientation is the axis transformation from one point (crystal orientation) in the dataset to another point. Deformation-induced changes in EBSD misorientation parameters, such as kernel average misorientation (KAM) and grain reference orientation deviation (GROD), were analysed as a function of the cycles incurred. EBSD settings

(e.g., working distance, binning, magnification) were kept as consistent as possible for the irradiated and reference specimens through the test.

5.2 Experimental details

Bulk specimen discs from the gauge section of each material state were sectioned (5 mm thick specimen in axial direction, wire cut in gauge section) for EBSD analysis. The specimen was mounted in a Bakelite resin and polished using successively finer diamond suspensions (6um, 3um, 1um and 0.25um), followed by polishing using an oxide polishing solution (OPS 50nm – SiO_2) for SEM investigations. For these investigations, the loading direction is axial (from left to right).

It is challenging to distinguish between different grain boundaries while using imaging techniques alone, the boundary character of micro-grains is also studied through EBSD using a Nordlys HKL system of a JEOL JSM 7001F Field Emission Gun (FEG) SEM (JEOL Ltd., Tokyo, Japan) using settings of 15 keV, beam of 3nA, a magnification of 507 to get a 500X500 microns field of view and 0.5 µm step size using 8X16 binning.

5.3 Methodology to characterise intragranular strain distribution.

Prior to the processing of EBSD data, grain orientation analysis was initially done by first calculating the grains in the different specimen and indexing the grains. Further processing included noise removal through a half quadratic optimization filter with a smoothing parameter of 5. No noise removal was performed for misorientation analysis to prevent smoothing over sub grain boundaries. The post-processing performed on the EBSD data was with the use of the MTEX 5.2. The toolbox was operated using MATLAB version R2020a. See Appendix C for the MATLAB script used.

In the literature review, it was shown that several dislocation density analysis methods utilising user-defined boundary maps can be created from misorientation angle data to indicate areas a high concentrations of dislocation density. This analysis reveals a qualitative assessment of the degree of deformation in specific samples. To perform a qualitative assessment as a function of misorientation angle, a comparison of the varying misorientation analysis parameters will be performed using histograms. The following section details the assessment methods chosen in this study.

5.3.1 Average Misorientation to mean orientation.

This method performs a quantitative analysis by taking the mean orientation of each grain and for each pixel it plots the deviation from the mean, which is a number, thus the misorientation relative to the mean orientation in a particular grain is plotted. The critical misorientation applied to all material states is 5°. The histogram of this plot has the advantage of showing even slight variations between samples in a semi-qualitative manner.

5.3.2 Grain Reference Orientation Deviation (GROD)

The GROD misorientation is defined as the difference between the orientation of a coordinate and the mean orientation of the grain position. This parameter quantifies the misalignment between the orientation at a specific coordinate and the reference (or average) orientation of the grain. In the current study, the GROD value was calculated by determining the average orientation of the grain, and then calculating the GROD for each point within the grain as the difference between the point orientation and the average grain orientation. The GROD misorientation metric provides a map of misorientation referenced to the mean orientation of all points in a grain. GROD maps are particularly useful for highlighting localized changes in the material structure, such as the presence of dislocation substructure after material fabrication or in-service defect accumulation. GROD is occasionally used to quantify strain level; however, the parameter correlates closely with the accumulated damage as high-GROD areas in the deformed material may be connected to inclusions or defects.

5.3.3 Kernel Average Misorientation (KAM)

To evade the difficulties associated with grain detection and the proper selection of reference orientation, KAM is frequently utilized as a qualitative measure for localizing plastic deformation (Lehto, 2021). KAM has been demonstrated to be influenced by the GND density, which is a measure of lattice curvature, and it is associated with the applied macroscopic strain when considered over multiple grains or an entire measurement field. The parameter calculates the average misorientation between a central point and its nearest neighbours. The size of the kernel is determined by the number of nearest neighbours from a central point, with analysis typically carried out using 1 to 3 nearest neighbours. The sensitivity of KAM results to various factors has been reported: 1) the angular and spatial resolution of the data, 2) the size of the kernel, and 3) the threshold angle θ_{max} for excluding data-points originating from neighbouring grains, which is usually in the range of 2-5°. In particular, the evaluation of misorientation angles below 0.5

degrees is hindered by the angular resolution of EBSD. Lehto 2021, suggested that EBSD-based analysis methods should be advanced beyond nearest-neighbour or point-to-point procedures to detect small local misorientation gradients.

The orientation data was processed using the half-quadratic filter developed by (R. Bergmann, 2016) to reduce measurement noise and assign orientations to non-indexed points. This filter is edge-preserving and suitable for analysing sub-structural features, as opposed to other commonly used filters. The KAM value was calculated using only the nearest neighbours with a maximum misorientation of 4° and utilizing all points in the kernel. KAM does not rely on the direct use of EBSD grain definition and is therefore less susceptible to grain fragmentation compared to GROD However, the KAM value depends on the EBSD step size and may be affected by factors such as specimen preparation and quality, as well as voltage.

5.4 Strain characterization as a function of fatigue damage

5.4.1 Average Misorientation to mean orientation.

The results are shown in Figure 31 for all material states. The annealed material state mostly has very low misorientation angles. However, there a few spots with higher angle grain boundaries of between 10° to 12° which is considered higher for an annealed steel. A closure look at these areas (area 1 and area 6) as shown in Appendix D and in comparison, to the index pole figure (IPF) image with grain boundaries drawn, it is clear that what appears to be localised deformation at these areas is actually incomplete boundaries which has one area of the grain which is at a different orientation to the next grain. The software sees this as one grain and takes an average orientation between two different grains. When the difference between the actual pixel orientation and the average orientation is worked out, high values of misorientation will result. These are artifacts of the reconstruction.

The specimen cycled to 500k cycles (Figure 32 (b)) shows more areas of deformation as compared to the annealed specimen. Generally, this specimen is dominated by very low misorientation angles in the region between 0° to 4°. However, similar to the previous material states, isolated spots of deformation between misorientation angles of 4° to 8° are evident. Further, very minimal large misorientation angles between 10° to 12° are evident. Specific areas that make up this montage image have also been investigated as shows, corresponding to item 1 and 6 in the montage image. Analysis of this area with the IPF shows that the different coloured grains are all part of one grain.

In the 1 million cycled specimen (Figure 32 (c)), there are similarities in the data in line with the analysis performed in the 500k cycled specimen. However, this specimen contains more misorientation angles between 1.5° to 4. A closer look of the area montage shows that for area 6, the misorientation between 4° to 6° is part of one grain while the misorientation between 10° to 12° occurs in a grain boundary. While area 1 in the same image shows that the misorientation angles between 4° to 6° are part of one grain and there is no grain boundary between them.

A qualitative comparison of the 3 million cycled specimen as shown Figure 31 (d) indicates that the level of deformation may be lower than what was observed in the 500k cycled and the 1 million cycled specimen. This observation contradicts the understanding of cumulative fatigue damage with increased levels of cycles in the specimen. With that being noted, an assessment similar to the ones discussed above is performed by zooming into area 1 and 6 of the montage. The misorientation angle between 10° to 12° in area 1 does not occur at a grain boundary but at a sub-grain boundary. Similarly, the misorientation between 6° to 8° in area 6 does not occur at a grain boundary.

The 11 million cycled specimen has more areas of deformation evident in the micro-structure with increased sub-grain boundaries as shown in Figure 31 (e). Area 1 of this montage shows that the deformation is not on the grain boundary but on the sub grain boundary while the deformation in area 5 also occurs on the sub grain boundary.

The last specimen in this analysis as shown in Figure 31 (f) depicts has a higher scale bar in relation to the previous specimens. This is done to qualitatively show the resolution of the misorientation that occurs in the sample as a result of higher deformation.

The histograms of the material states are shown in Figure 32. It can be clearly seen that there are less misorientation angle, implying less dislocations, in the annealed specimen in comparison to all other specimens in the study. Also, the misorientation angle in this specimen ranges between 0° to 0.5°.

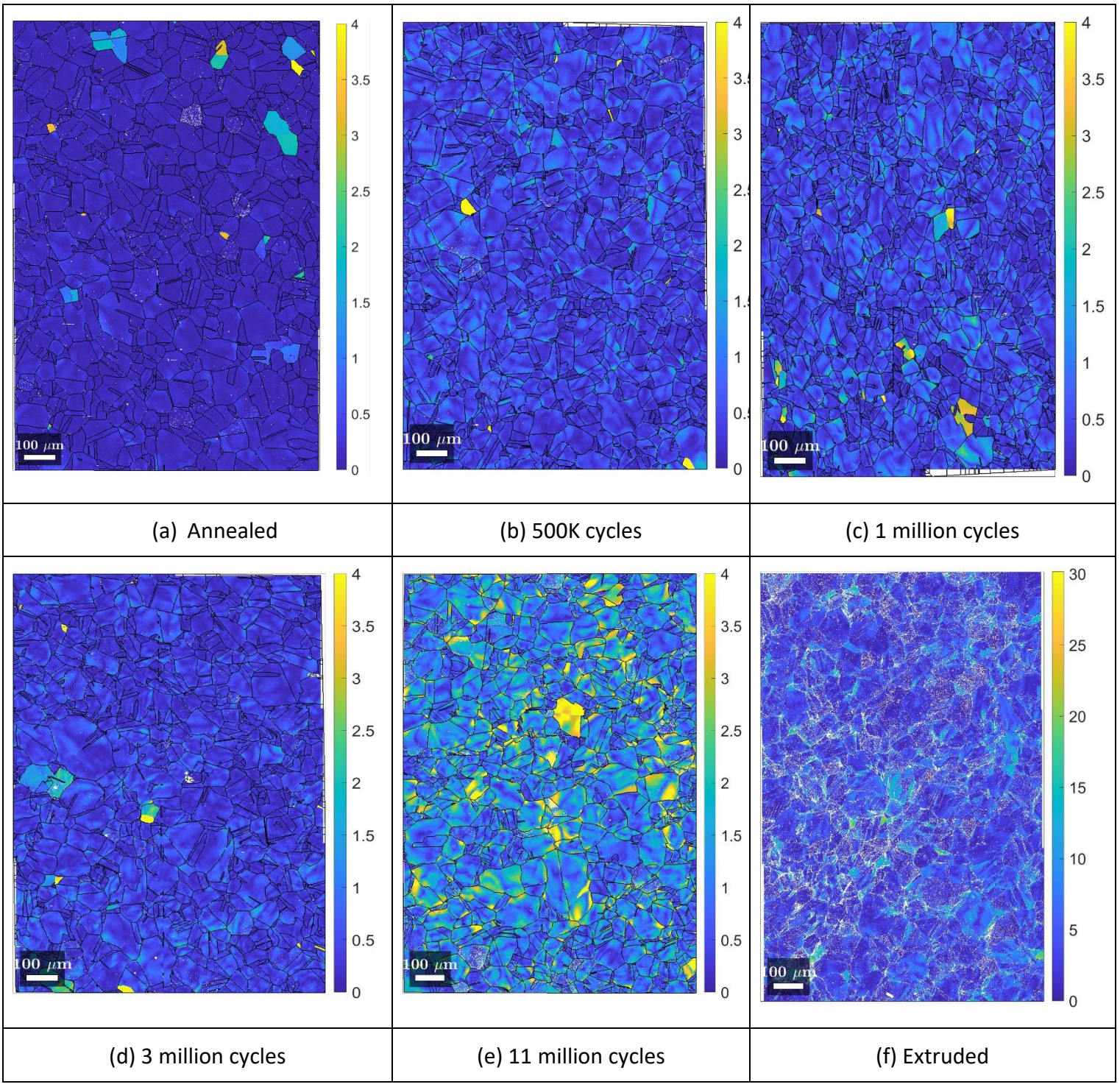

(a) Annealed | (b) 500K cycles | (c) 1 million cycles

(d) 3 million cycles | (e) 11 million cycles | (f) Extruded

Figure 31: Misorientation to mean maps of AISI316L stainless steel for different material states.

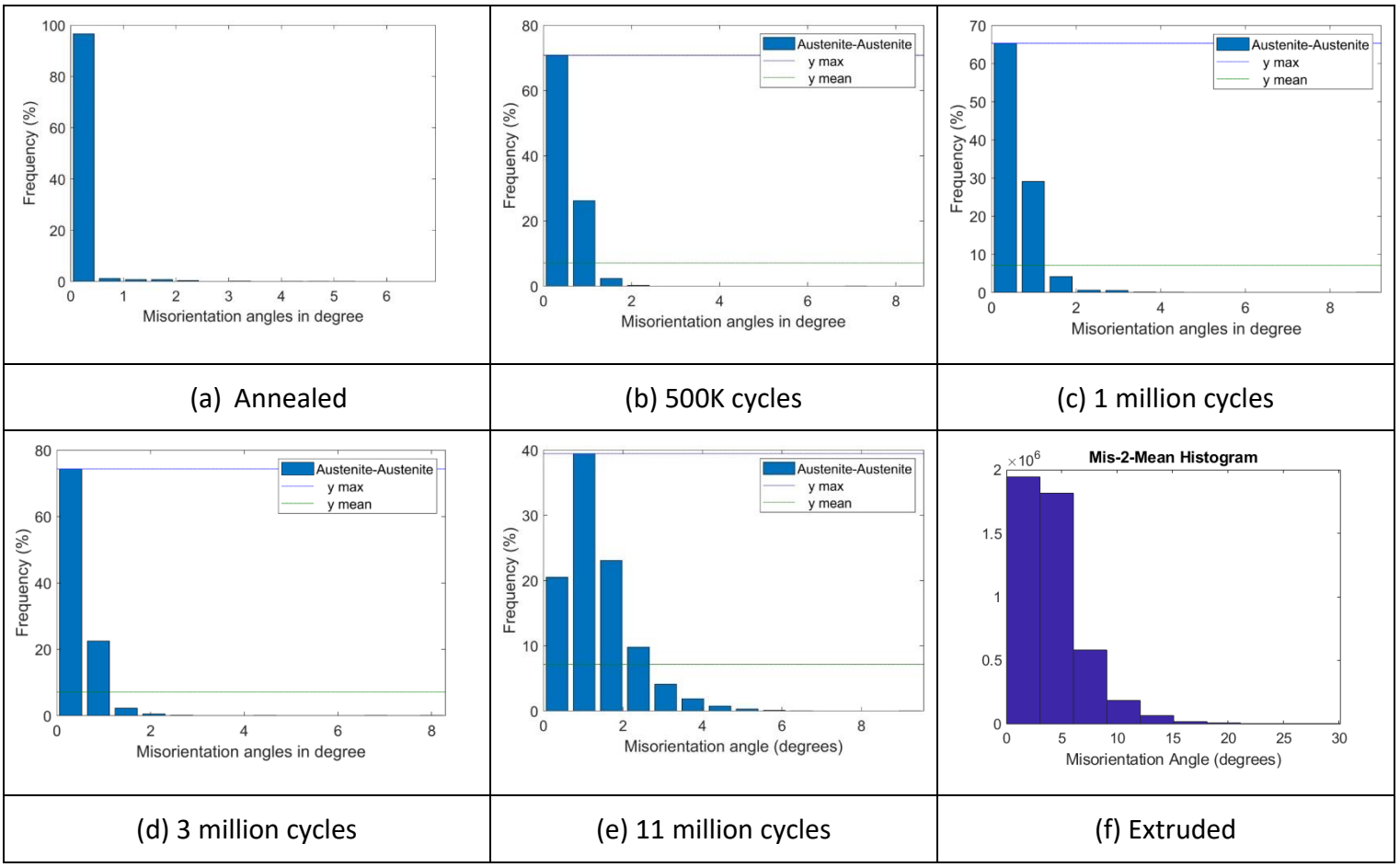

(a) Annealed | (b) 500K cycles | (c) 1 million cycles

(d) 3 million cycles | (e) 11 million cycles | (f) Extruded

Figure 32: Histograms of misorientation angle for all material states

5.4.2 Grain Reference Orientation Deviation (GROD)

Figure 33 (a) shows 0° to 4° misorientation on annealed steel. The 2° to 4° misorientation matches the deformation in Figure 32. Misorientation between grains is visible at grain boundaries and triple points, although it is spread out in this sample. Compared to Figure 33 (b), misorientation is more pronounced in the annealed sample. The image also shows misorientation lines (faint red lines) within the grains. Figure 34 (c) shows more misorientation lines and angles in the 2° to 4° range in the 1 million cycle specimen. Figure 34 (d) shows less misorientation compared to the 500k and 1 million cycled specimens. The 11 million cycled specimen has more deformation with misorientation angles in the 2° to 4° range. The misorientation lines in this specimen are higher than in the others. The extruded specimen (Figure 34 (e)) shows increased deformation, with misorientation to mean angle in the 3°-4° range. As the number of fatigue cycles is increased, local GROD values increase in the austenitic steel.

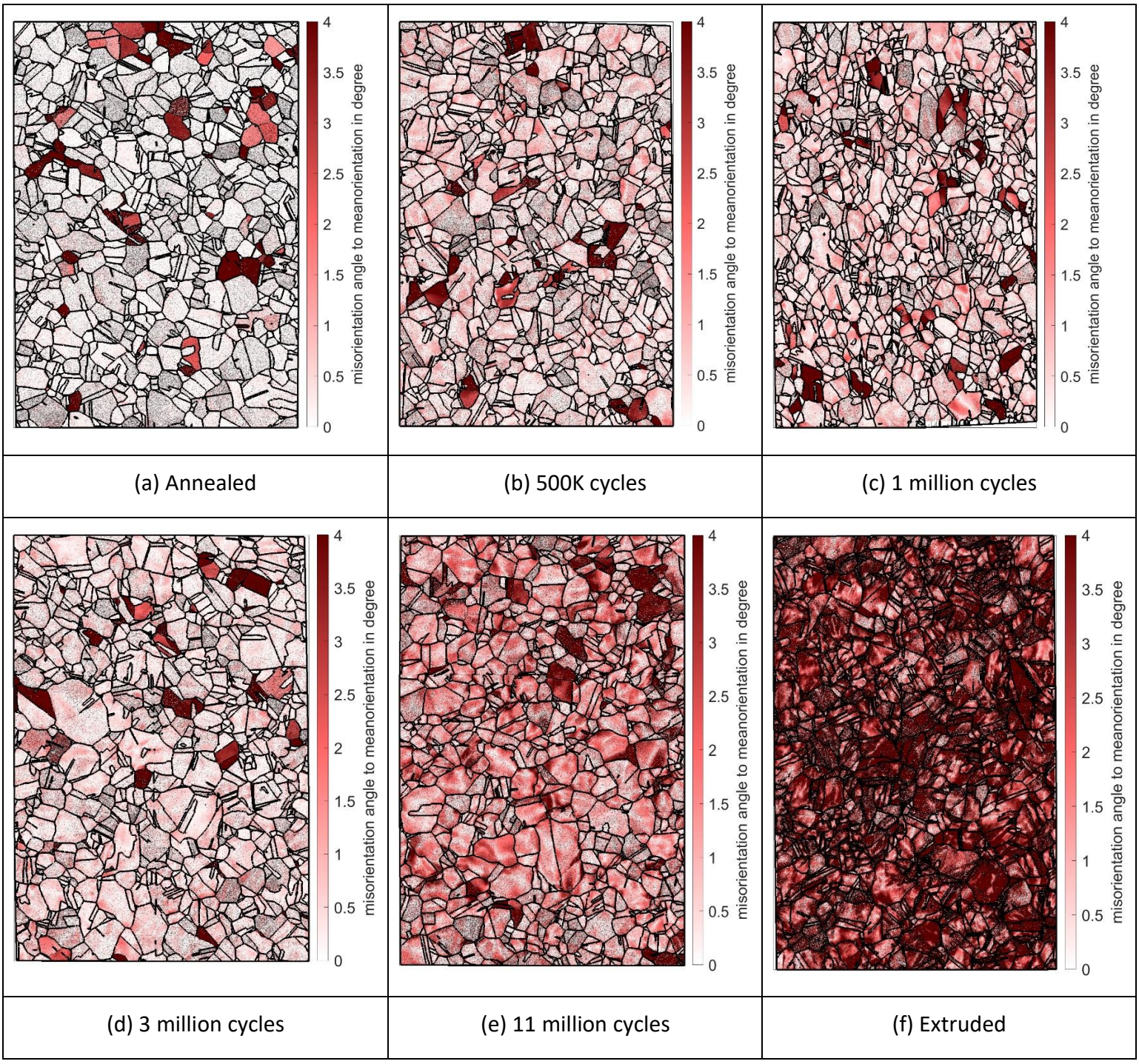

(a) Annealed | (b) 500K cycles | (c) 1 million cycles

(d) 3 million cycles | (e) 11 million cycles | (f) Extruded

Figure 33: GROD maps of AISI316L stainless steel for different material states

5.4.3 Kernel Average Misorientation (KAM)

KAM dataset plotted as a map in Figure 35, reveals areas with an increased density of the defects, and as an average value for the whole scan, may reflect material strain history. The KAM map for the annealed material (Figure 34 (a)) does not exhibit any significant gradients inside grains, showing the material was practically deformation-free. At increased loading cycles, the increased KAM values are often observed along grain boundaries, indicating the formation of fine channels or slip lines at different locations.

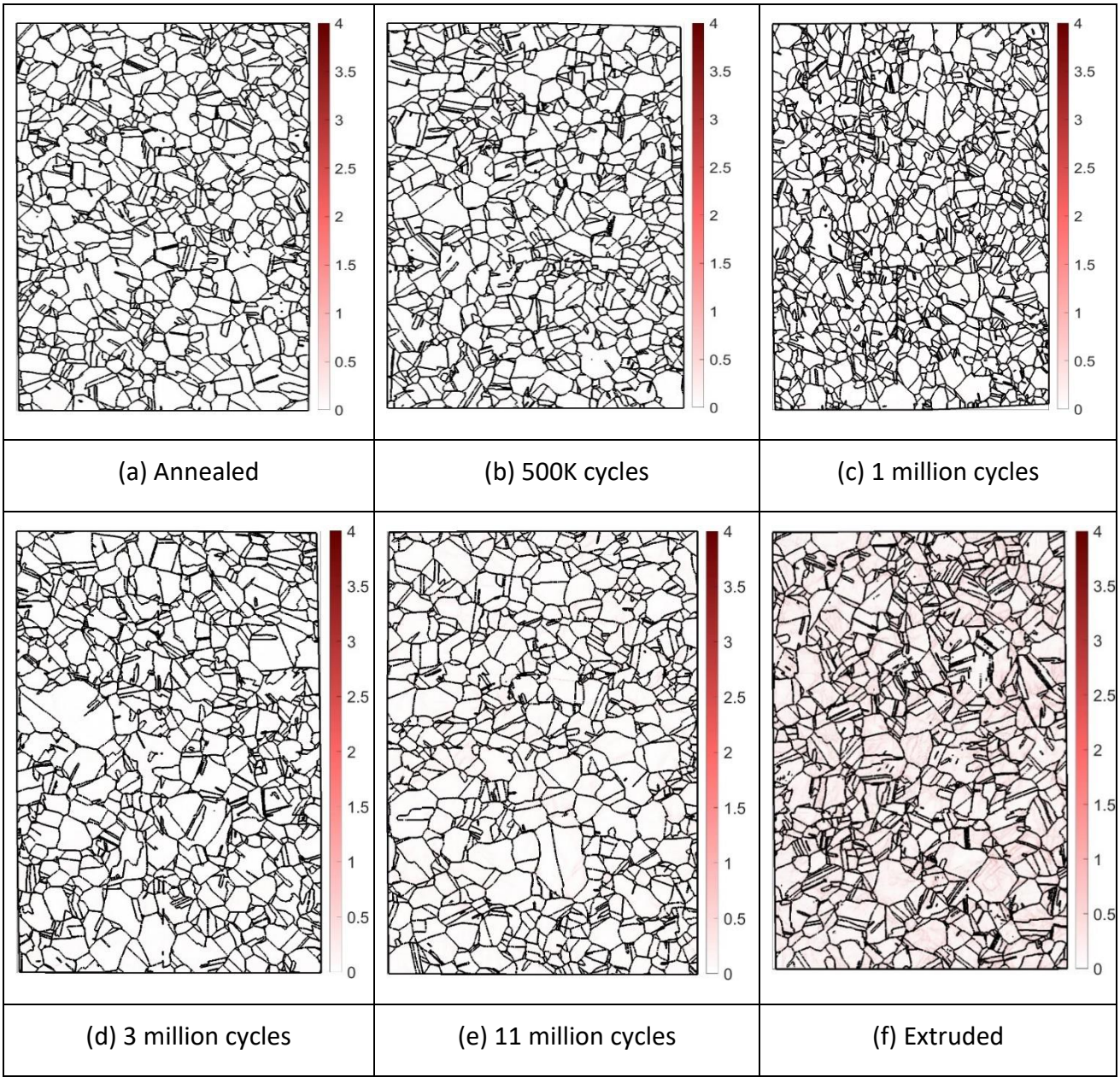

(a) Annealed	(b) 500K cycles	(c) 1 million cycles
(d) 3 million cycles	(e) 11 million cycles	(f) Extruded

Figure 34: KAM maps of AISI316L stainless steel for different material states

At small strain levels applied to the specimen, the increased KAM values usually coincide with a GROD hot spot. However, increased KAM values are often observed along grain boundaries, indicating the formation of fine channels or slip lines at different locations. A qualitative measure of deformation localisation is quite evident in the specimen cycled up to 11 million cycles (Figure 34 (e)) as well as in the extruded specimen (Figure 34 (e)). While the 500k and the 1 million cycled specimens (Figure 34 (b and c)) also show the sub grain structures very faintly The KAM values characterize changes in the local misorientation caused by dislocations.

5.5 Discussion of the influence of fatigue on final misorientation distribution using misorientation analysis techniques

The application of automated EBSD in the scanning electron microscope, to the qualitative and semi-quantitative analysis of grain structures based on final misorientation level of post-mortem low alloy steel after fatigue tests, was analysed. Despite its simplicity, misorientation is a fundamental quantity in EBSD measurements, and there are multiple methods for quantifying and depicting it or related attributes. Misorientation is a relative orientation, it is relative to some other orientation. The specific orientation chosen for reference has a significant impact on the nature of the measurement or visualization. The most basic measurement and visualization of misorientation is grain boundary mapping. The locations in EBSD where the scalar misorientation between adjacent pixels is greater than a certain critical value is referred to as grain boundaries. The critical misorientation value for high angle grain boundaries (HAGB) in a polycrystal is generally between 7 and 15 degrees, but one can also plot the density of low angle grain boundaries (LAGB) with misorientations between 1 and 10 degrees (Brewer LN, 2006). These maps will show a higher density of LAGBs in areas of deformation. The four misorientation parameters used in EBSD analysis in the section above are largely similar as they all display qualitative evidence of localised LAGB in the region of 0 and 4˚.

To qualitatively compare the EBSD parameters used in the study, Figure 35 displays only the low cycle fatigue specimen. By close inspection, it is evident that the regions of highest internal misorientation in Figure 36 (a) correspond somewhat to the regions of highest misorientation network density in Figure 35 (b) and (c). However, the intensity in the KAM maps is relatively uniform for each grain, while the level of misorientation in the integrated misorientation maps varies more from grain to grain as is seen in the orientation maps of Figure 36 which displays consistency in the localisation of deformation across the Mis-2-mean, GROD and KAM plots.

Similarly, the qualitative distribution of localised dislocation is evident in the annealed, the 11 million cycles and the extruded specimen in Figure 36 has the same observation as above. However, a qualitative evaluation of these specimen shows that the level of deformation across each specimen is sufficiently different. With regards to the extruded specimen, it should be noted that scalar misorientation does not provide any information about the character of the boundaries with small angles. One reason for this scarcity of detail is that the definition of the misorientation axis becomes increasingly unclear as the misorientation angle decreases (Prior 1999). One disadvantage of using LAGB maps is that they only reveal the local sources of misorientation rather than their overall impact across the grain. As a result, LAGB maps can be quite noisy.

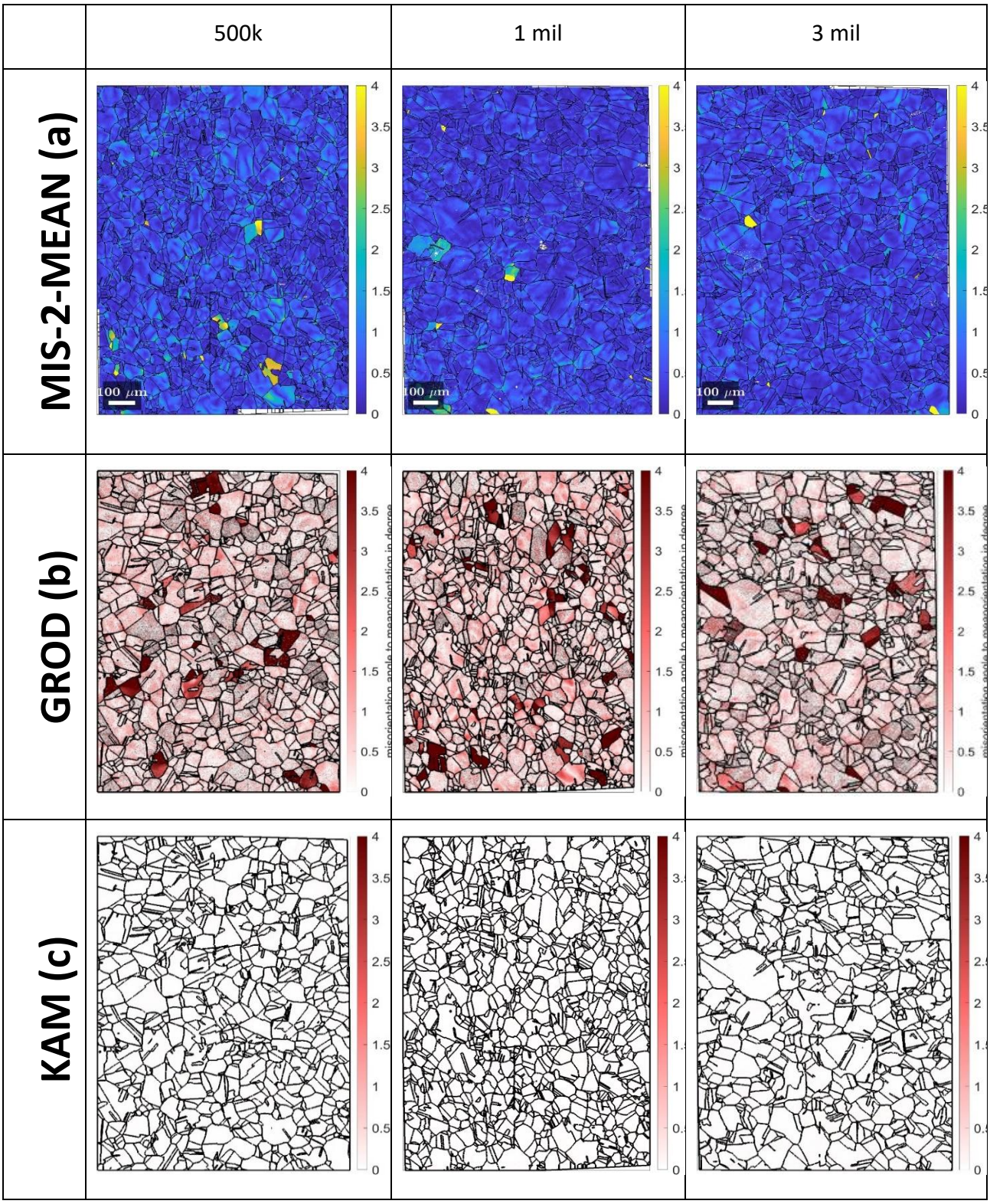

Figure 35: Different orientation map parameters for low fatigue cycled specimen. (a) Misorientation to mean, (b) GROD and (c) KAM.

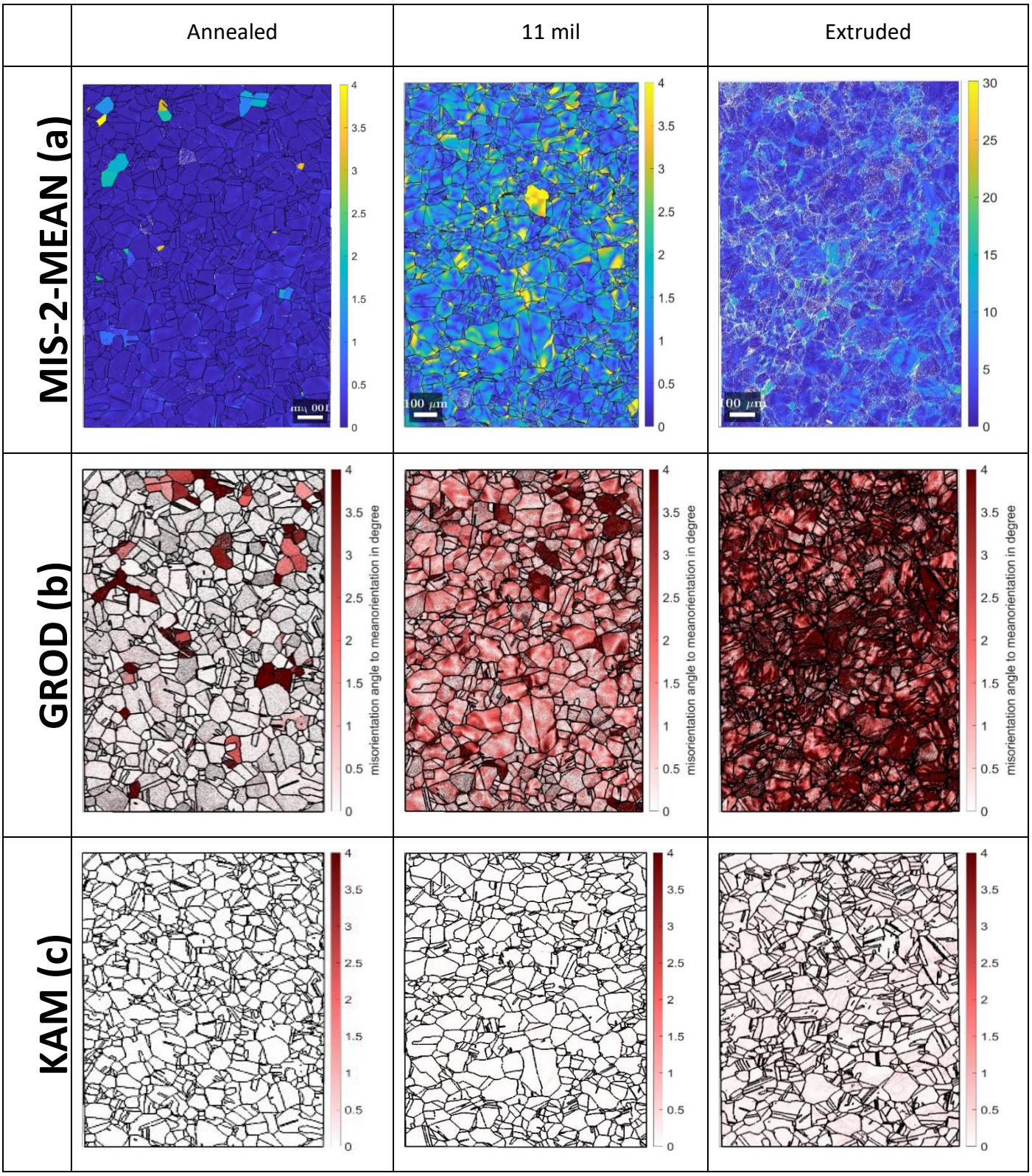

Figure 36: Different orientation map parameters for (a) Misorientation to mean, (b) GROD and (c) KAM.

5.6 Chapter Summary

In this chapter, an analysis of EBSD images was performed using various misorientation analysis techniques to qualitatively quantify the level of deformation for each material state. The misorientation analysis techniques used were as follows:

a) Calculating the average misorientation to mean
b) Calculating the GROD maps
c) Calculating the misorientation according to crystal symmetry
d) Calculation the Kernel Average Misorientation (KAM) maps

The analysis was performed using MTEX and the same specimen used for PXRD analysis were used. The technique was largely capable of qualitatively differentiating between the different material tests provided an adequate deformation signal is evident.

In comparison to the PXRD technique, the EBSD results mostly agree with the PXRD, except for the 11M and 3M fatigue tested samples. The PXRD analysis shows that the 3M has more dislocation density for all sets of samples, while for EBSD, the results present a lower relative misorientations for the 3M sample. This could be largely as a result of the differences in the characterization technique since EBSD is surface characterization technique while PXRD is a bulk technique.

A qualitative evaluation of the EBSD data for the 11M cycle sample should have much more dislocations that the observations in Figure 32 and Figure 33. It is evident that there is a structured rearrangement of the dislocations for the 11M sample into domains. This could be as a result of the free dislocations that contribute to the PXRD microstrain forms dislocation tangles/walls and causes misorientations within the grains as measured using EBSD but invisible to PXRD.

Chapter 6. Quantitative dislocation density analysis from TEM micrographs of fatigued specimens

6.1 Introduction

Quantification of dislocations in material states has been performed using several techniques including those described in Chapter 4 (PXRD) and Chapter 5 (EBSD). Of these, only TEM images show dislocations directly as described in section 2.4.2. To resolve a dislocation during TEM imaging, an objective aperture is used which only lets the electrons to go through the sample. The literature study has resolved that TEM in scanning mode could provide micro-textures supporting PXRD, see Section 2.4.2.2. Further, resolution of STEM images is not limited by the effect of chromatic aberrations of imaging lenses due to inelastic scattering of the electrons within the specimen as seen in TEM bright-field images (Zheng CL et al, 2013). In this chapter, STEM characterization was used to investigate the microstructural evolution on deformation-induced specimens at room temperature in comparison to the extruded and annealed material states by quantify the dislocation densities in the different material states.

6.2 Experimental details

Thin foils of 3 mm diameter discs were prepared for TEM observations from each of the sample material states. The foils were cut in the gauge section of fatigue tested specimen starting with approximately 300 µm thicknesses and ground up to a final thickness of 150 µm. The specimens were then jet-electropolished with a suitable solution to obtain transparent areas near the central hole. The jet electro-polishing was performed by TENUPOL 5. TEM observations were performed using JEOL 2100 LaB_6 operated at 200 kV and fitted with JOEL ABF/ADF STEM detectors. Areas of 6x6 μm^2 in size are imaged (2048x2048 pixels) using a 20 mRad STEM-probe convergence semi-angle with an annular dark field (ADF) detector. The camera length is chosen such that the signal over collection angles of 18 mRad (inner) and 47 mRad (outer) are captured. The specimens for TEM investigations were prepared perpendicular to the external load axis where a cross sectional slice was cut out from the gauge area and jet polished to make a TEM

sample. The imaging was performed using the annular dark-field (ADF) scanning transmission electron microscope (STEM) mode where the electron probe is scanned across the specimen disc; in this way, more dislocations are resolved. It should be noted that no tilting was performed during this experimental test and the thickness was not measured at the particular location.

The semi-quantitative evaluation of dislocation densities in the TEM micrographs can be manually performed by performing a linear intercept method (LIM) whereby horizontal and vertical lines of known line length are superimposed on the image central micro grain as shown in Figure 37. These lines, with same length, represent test lines traditionally used in manual quantitative assessments (George Crowly, 2019). The number of instances where the superimposed lines intersect with the dislocations added and the dislocation density calculated with as shown in Equation 13.

(a) (b)

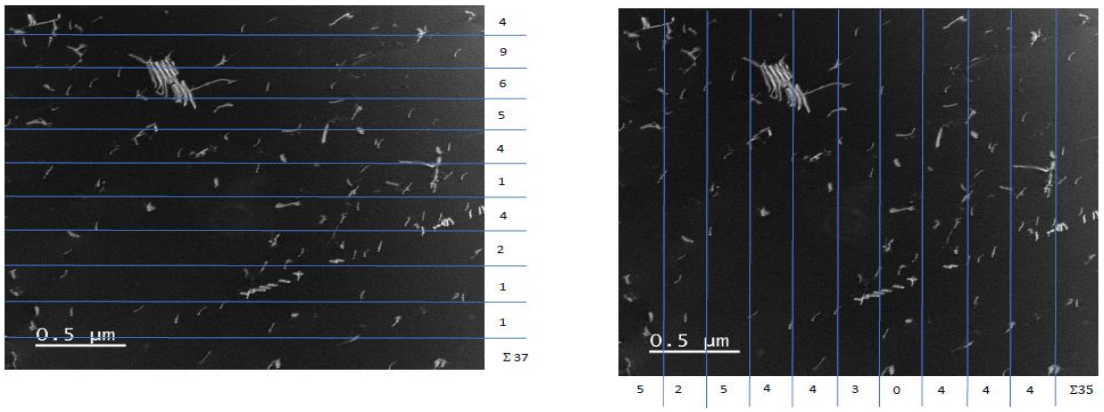

Figure 37: TEM micrograph with superimposed (a) horizontal and (b) vertical lines.

Dislocation density quantification was originally performed using multi-level image segmentation from the TEM micrograph using Image-J software. This process enables the individual TEM images to be filtered for noise and calibrated. Thereafter, the image background is segmented from the dislocations using Otsu's method. The final steps include measuring the dislocations and processing the results. However, since the boundaries could not be accurately determined, this option was aborted. This prompted the use of a manual dislocation counting using the naked eye. It was found that the eye was more accurate in resolving the intersection of the dislocations within the micrograph without the need for the automated resolution with the software. The film thickness was estimated to be approximately 100nm for all micrographs.

6.3 Results

Appendix E shows ten raw images per material state. These were printed and ten vertical and horizontal lines were drawn on each image as preparation for dislocation counting using the LIM method. One site per material state is shown on Figure 38, qualitatively, there is marginal differences between the lower fatigue tested cycled material states. However, there are significant differences between the extruded and the annealed material states even when compared to the fatigue cycled specimen. A statistical analysis of the variance in dislocation density between the applicable material states is shown in Table 9. A T-test was performed to check whether there is any significant difference between the data set of the samples tested. This is to give some data objectivity thereby eliminating bias in the results presented. The mean does not provide a conclusive case in identifying biases. In this test, a value that is smaller than the critical value ($P < 0.05$), where there is a less than 5% chance that the data is random and greater than 95% chance that the data is significant. A t-test does not only look at the spread but also the mean of the standard deviation. In this instance, a two-tailed unpaired T-test was performed as there is no linkage between the data and one is looking at outliers from both extremes.

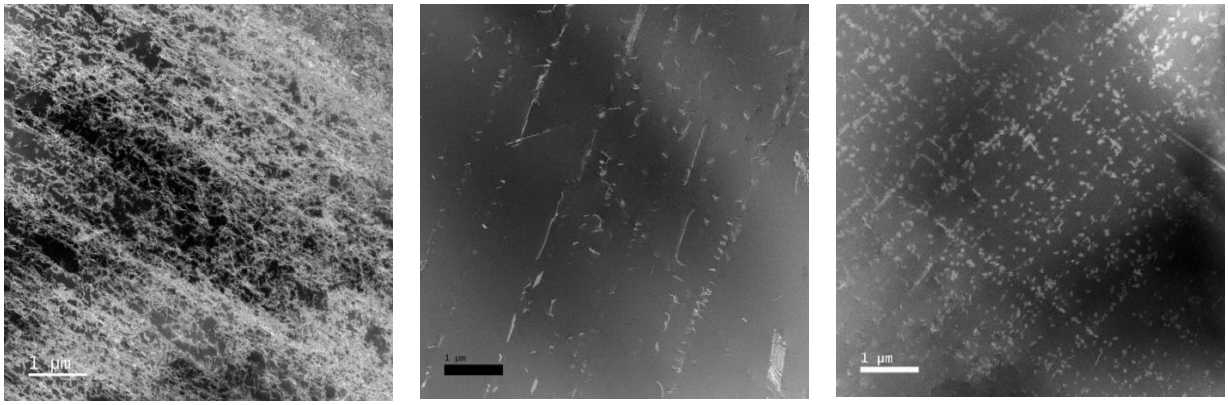

(a) Extruded (b) Annealed (c) 500K

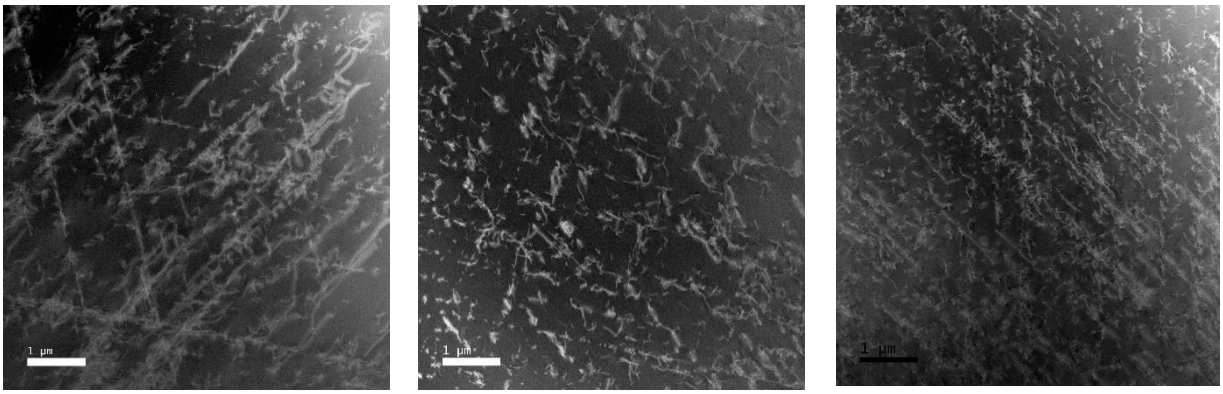

(d) 1M (e) 3M (f) 11M

Figure 38: TEM micrographs per material state

The results indicate that the dislocation densities from the annealed sample data is significantly different to the sample cycled up to 500 000 cycles as well as another higher cycled specimen. For the hypothesis test of the dislocation densities between the specimen cycled to 11 million cycles in comparison to the annealed specimen, the test results showed a critical value of P = 0,000000211. This value is significantly lower than 5% thus indicating that the dislocations variance in the two specimen is significantly different. Therefore, there is a low probability that the data is random. Since the mean values of the 500 000 cycles to the 1 million cycles are close to each other, a t-test was also performed for these samples which resulted in a critical value of P = 0,004152365. This value is less than 5% which is an indication that there is a significant difference between the two specimens and further gives greater confidence that although the mean values are close, the dislocation density is significantly different.

Table 9: Dislocation density results per material state (m^{-2})

Site no.	Material States					
	Extruded	Annealed	500k cycles	1 million cycles	3 million cycles	11 million cycles
Site 1	1,46E+14	3,47E+13	4,96E+13	5,78E+13	7,36E+13	5,00E+13
Site 2	8,53E+13	3,42E+13	6,79E+13	6,05E+13	5,39E+13	6,76E+13
Site 3	9,75E+13	3,47E+13	7,46E+13	5,38E+13	7,04E+13	6,79E+13
Site 4	1,27E+14	3,95E+13	4,75E+13	3,47E+13	7,22E+13	7,60E+13
Site 5	1,40E+14	5,22E+13	4,93E+13	6,53E+13	5,76E+13	7,06E+13
Site 6	8,74E+13	3,28E+13	5,23E+13	5,68E+13	6,74E+13	7,53E+13
Site 7	5,23E+13	2,74E+13	6,06E+13	5,32E+13	7,23E+13	6,52E+13
Site 8	1,15E+14	2,68E+13	6,85E+13	5,96E+13	6,11E+13	6,13E+13
Site 9	7,75E+13	4,87E+13	3,28E+13	3,36E+13	5,84E+13	6,42E+13
Site 10	1,06E+14	3,10E+13	3,46E+13	4,97E+13	5,41E+13	4,61E+13
Total	1,03E+15	3,62E+14	5,38E+14	5,25E+14	6,41E+14	6,44E+14
Minimum	5,23E+13	2,68E+13	3,28E+13	3,36E+13	5,39E+13	4,61E+13
Q1	8,583E+13	3,145E+13	4,795E+13	5,0575E+13	5,78E+13	6,2025E+13
Median	1,016E+14	3,445E+13	5,645E+13	5,53E+13	6,425E+13	6,775E+13
Q3	1,236E+14	3,83E+13	6,6525E+13	5,915E+13	7,175E+13	7,4125E+13
Maximum	1,032E+15	5,22E+13	5,377E+14	6,53E+13	7,36E+13	6,442E+14
Mean	9,801E+14	3,62E+13	5,377E+13	5,25E+13	6,41E+13	6,44E+13
Range	1,03E+14	2,54E+13	5,049E+14	3,17E+13	1,97E+13	5,981E+14
$\sigma_{\bar{x}}$	9,236E+12	2,6584E+12	4,4513E+12	3,3481E+12	2,4977E+12	3,1035E+12

During the TEM testing, the thicknesses of each specimen was not measured. There is therefore an influence of thickness variations across each sample which may distort the results. Another limitation is that we only looked at small areas within the TEM, this is because the techniques is quite time consuming. Therefore, there is no confidence in the precision and accuracy of the techniques performed. It has also proven that there are difficulties in segmenting the images to perform the analysis in these samples. However, in this case, human segmentation was performed, and it has proven that this methodology is better that using software as the software may find difficulty is resolving a dislocation. Between the material states, there is clearly a large scatter of dislocations as seen in the image above. In all the imaging performed, the samples were not tilted. Orientation of grains to favour maximum dislocation contract on each image was not performed and this has contributed to the scatter in the results.

Figure 39 shows a box plot of the specimens in the study based on the dislocation density analysis methodology used. When solely analysing the dislocations in fatigued specimen, the results show that there is a large scatter and overlap of the dislocation density in all specimens. Also, there is a large variance between the annealed specimen and the fatigued specimen as expected. It is also evident that the extruded specimen has extensive deformation within the material sample. The dots in the image represent outliers which fall outside a certain number of standard deviations from the mean and the box plots take it out of the calculation.

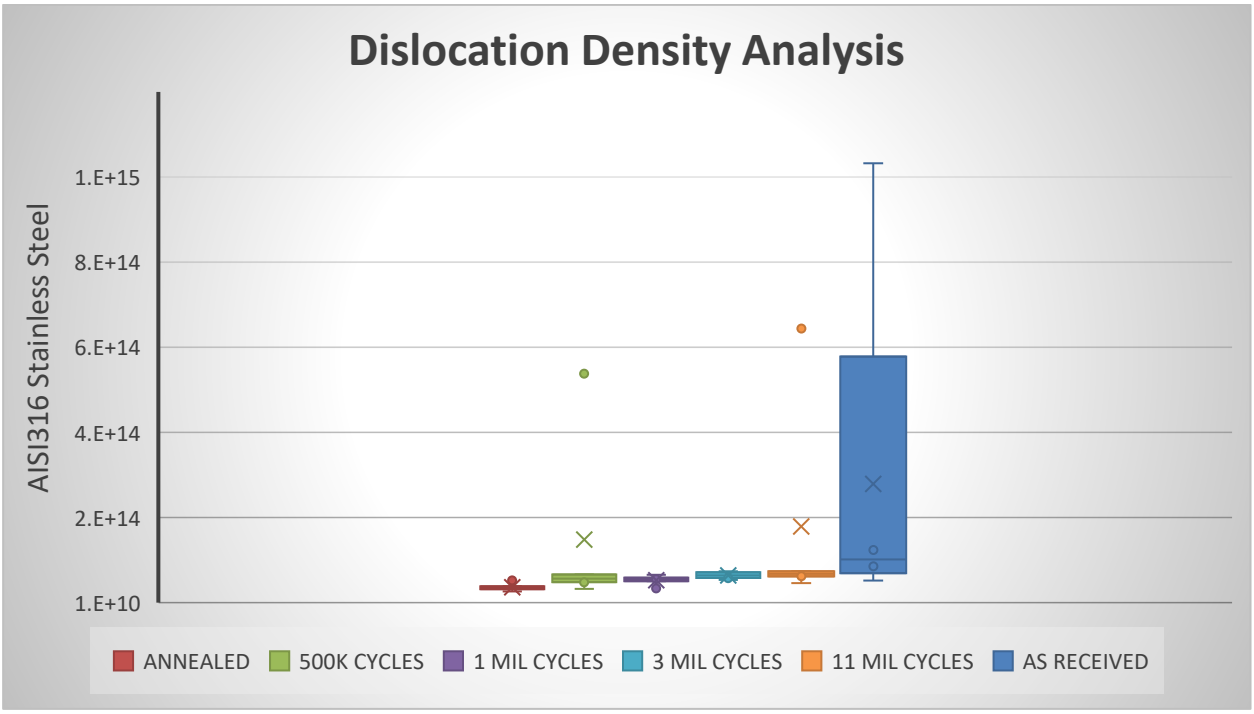

Figure 39: Dislocation Density per specimen

6.4 Discussions

The results indicate that STEM imaging mode is suited to study the evolution of dislocation densities in the austenitic stainless steel with differing material sates. The technique provides good dislocation contrasts and allows dislocation densities to be assessed over large fields of view. The results of dislocation showed good agreement of very high initial dislocation density in the order of greater than 10^{15} m^{-2} in cold rolled samples 316L-Type stainless steel subjected to cold or warm rolling followed by annealing in the study by (M. Odnobokova, 2020). A decrease in dislocation density is observed upon annealing to an average of approximately of 10^{13} m^{-2} which is comparable to the decreased dislocation density results obtained in this study. This

dislocation density decrease is as a result of continuous recrystallisation followed by grain growth during annealing. For fatigue exposed specimen at the same temperature, the results show the following:

i. There is at least moderate difference in dislocation density between the annealed state and its fatigue damage state.
ii. There is large spread in dislocation density which could also be affected by limited sampling makes it difficult to separate the different fatigue damage conditions.

6.5 Chapter summary

This chapter entails the analysis of the different material states by the transmission electron microscopy (TEM). The same material states discussed 3.4 were analysed to determine the dislocation densities in the specimens by systematically counting the dislocation density in the micrograph images for each sample using the line intercept method. The results indicate good ability of the technique to resolve dislocations in the micrographs, however, the quantification of dislocation density values overlaps for different fatigue damage conditions. This situation is influenced by:

i. Inhomogeneous strain (dislocation) distribution
ii. Limited sampling due to the tedious nature of acquiring appropriate TEM images.
iii. Estimation of constant thin foil thickness.

A quantitative comparison of dislocation density measurements using the TEM and PXRD techniques is shown in Figure 40.

In general, higher dislocation densities have been resolved using TEM. There is correlation between the annealed and extruded material states using both methodologies. However, large scatter exists between the fatigue cycled specimen. Albeit there is more spread of the TEM measurements for the low dislocation density samples. The TEM efforts for the evaluation of TEM micrographs for dislocation features such as the screening of strain fields, long-range internal stresses, dipole character, fractal character, etc., involves a tedious process. Whereas PXRD characteristic peak profile asymmetry; long-range internal stresses and the dipole structure of a dislocation system are closely related phenomena, where all have the same physical origin in the plastic deformation of materials having heterogeneous microstructures.

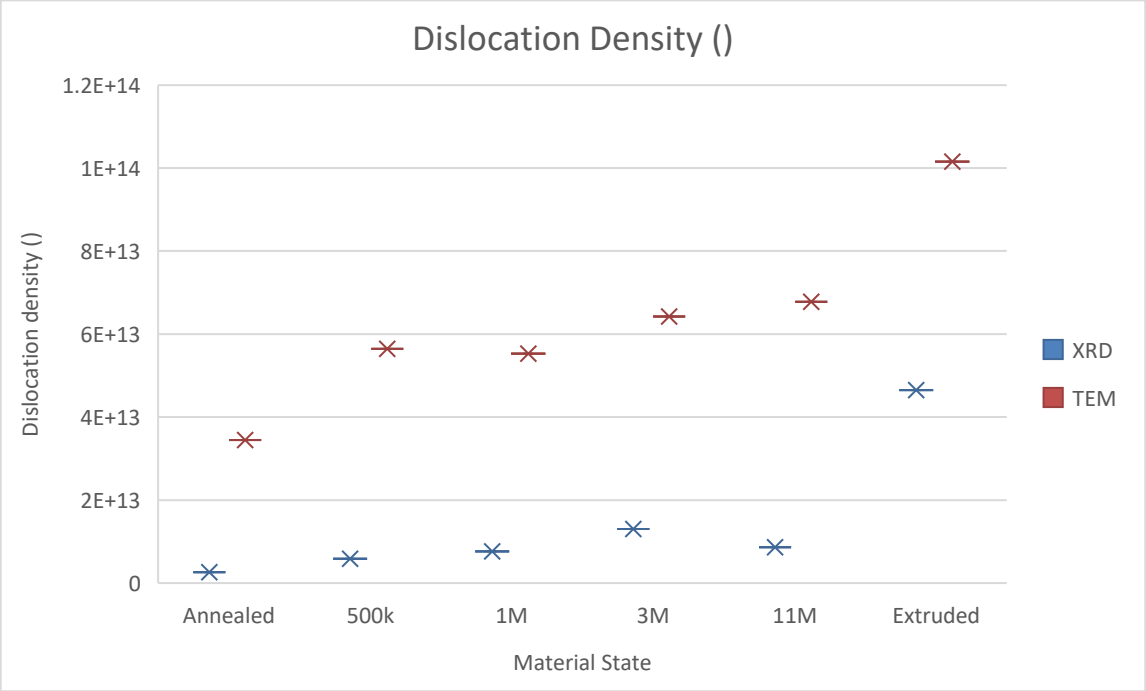

Figure 40: Dislocation density comparison using TEM and PXRD techniques.

Dislocation density measurements using PXRD and TEM can yield different values for a polycrystalline material due to the fundamental differences in their measurement principles, resolution, and statistical representation of the microstructure. These differences occur due to:

1. Measurement Principles – PXRD determines dislocation density indirectly through peak broadening in diffraction patterns. The broadening occurs due to strain fields around dislocations and grain size effects, which are analysed using models such as Williamson-Hall. While TEM provides a direct imaging-based measurement by counting dislocations in a given volume. The dislocation density is estimated as the number of dislocations per unit area in the image, extrapolated to a volumetric density.

2. Scale and Sampling Volume - PXRD averages over a much larger volume (hundreds of microns to millimeters) since it captures diffraction from a large number of grains and TEM analyses a very small, localized volume (typically in the nanometer range), leading to potential statistical bias, especially if the dislocation density is not homogeneous across the sample.

3. Crystallographic and Geometric Considerations - PXRD is sensitive to an overall distribution of strain but cannot distinguish between individual dislocations or their specific arrangements and

TEM captures discrete dislocations, but only those that are edge-on in the thin foil. Some dislocations may be invisible due to their orientation relative to the imaging conditions.

4. Effects of Grain Boundaries - In polycrystalline materials, dislocations can pile up at grain boundaries, leading to strain fields that affect PXRD measurements. However, TEM may not capture these effects fully, as it only observes a thin slice of material. PXRD also averages over many grains, including both high- and low-dislocation density regions, whereas TEM focuses on a select few grains, possibly skewing the observed density.

5. Strain Relaxation in TEM Samples - The process of preparing thin TEM foils (via ion milling or electropolishing) can lead to strain relaxation, reducing the observed dislocation density. In contrast, PXRD measures the bulk material, preserving the original dislocation distribution more effectively.

6. Experimental Limitations - PXRD can overestimate dislocation density if other factors contribute to peak broadening (e.g., stacking faults, nano-twinning). TEM can underestimate density if some dislocations are not visible due to thickness effects or imaging conditions.

In conclusion PXRD generally provides an average, bulk estimate of dislocation density, often higher than TEM values due to its sensitivity to strain fields. TEM, on the other hand, gives a localized, direct count of dislocations, which can be lower or variable depending on the observed regions. For the most reliable characterization, both techniques should be used in a complementary manner.

Chapter 7. Discussion

Chapters 3 to 6 in this study fulfil the objective requirements of the study in line with Section 1.5, following a journal article style consisting of introductory sections, results, discussions, and conclusions. This chapter broadens the discussion by combining the findings from the different techniques conducted and consequently uses this data to systematically correlate the damage assessment from PXRD, TEM, and SEM orientation imaging analysis results with the main aim of identifying the limitations and applicability of the PXRD technique against the TEM and SEM techniques after fatigue testing of the specimens. Future work encompassing quantification of the SEM and TEM datasets is explored in Section 7.5, which leads to a summary of recommendations on the applicability of this work to power plant utilities.

7.1 Fatigue damage accumulation of austenitic stainless steel AISI 316L

Literature has revealed that austenitic 316L stainless steels have a range of favourable mechanical properties, including good corrosion resistance, high strength under elevated temperatures, excellent ductility, and good weldability. This renders the material suitable for several effective applications because metastable austenitic stainless steels are versatile materials with good mechanical properties, good formability, and high corrosion resistance. The fatigue testing undertaken in Chapter 3 demonstrates that austenitic stainless steel AISI 316L exhibits a complex cyclic deformation response at room temperature, which can be characterized by three stages: cyclic hardening followed by cyclic softening, and finally a cyclic saturation stage before failure, where internal stresses play a significant role. The question that needs to be answered is whether austenitic stainless steel AISI316L serves as a model single-phase polycrystalline alloy to attempt to track fatigue damage accumulation. The answer lies in the microstructural state and its evolution during various cycles of fatigue testing. During cold working of austenitic stainless steel, stacking faults, stacking fault bundles or faulted α ‘martensite, deformation twins, deformation bands, and α’ martensite may be formed, in addition to intensive dislocation multiplication. The deformation substructure is determined by the stacking fault energy (SFE) level of a material. Generally, a lower SFE makes dislocation cross-slip more difficult, favouring a more homogeneous dislocation distribution with less tendency

towards the formation of dislocation cells. In low-SFE FCC metals and alloys, SFE has an indirect effect by increasing dislocation density and strain hardening. Thus, when the deformed metal is annealed, recovery and/or recrystallization may occur depending on several factors that may have a minor effect on the macroscopic strain-hardening behaviour of austenitic stainless steel. However, this changes the dislocation density and distribution around the particles. In general, a lower SFE makes dislocation cross-slip more difficult, resulting in less dislocation mobility. This favours a more homogeneous dislocation distribution with a lower tendency towards the formation of dislocation cells. Thus, in its annealed state, this steel presents a microstructure that is more stable and has little or no dislocations. Even if the macroscopic strain appears uniform and homogeneous, the local strain of the polycrystalline material is inhomogeneous owing to the anisotropy of crystal grains and their random or nearly random orientation distribution (K. Hashimoto, 1983).

In Chapter 3, it is emphasized that conducting experimental tests is crucial to develop a fatigue damage accumulation model. These tests serve as the physical basis for the formulated numerical dependencies of the material being studied. The fatigue damage experimental model proposed in this study adheres to the standard E466-15 and involves conducting forced-controlled uniaxial cyclic testing of cylindrical austenitic stainless-steel samples as a model alloy at room temperature. The working surfaces of the specimens are polished until a satisfactory smoothness is achieved. Preliminary tests, including the cyclic loading of a flat sample and observation of the amount of energy dissipated from the material due to the action of plastic strains, are performed to investigate the fatigue damage accumulation process. The model's capability to account for the loading history in the fatigue damage accumulation process is a significant advantage. This process involves determining the stress or strain tensor components based on the method of the affecting force, whether it is a force or displacement. Tests have shown that in the initial loading phase, due to the effect of cyclic loads, damage accumulates gradually with every cycle of high amplitude loading until the material reaches a certain limit state. Once this limit is exceeded, the "damage density" becomes high enough that the material can no longer safely carry the load applied to it. This leads to the appearance of microcracks in the material, which results in a sharp increase in damage during further loading. Subsequently, faults increase exponentially until macrocracks form, leading to the decohesion of the material. Elevated temperatures can facilitate the yielding of the material and make it easier for dislocations to move within the material. Additionally, temperature changes can alter the cracking character and time until failure.

7.2 Measurement and analysis protocol to enable accurate strain measurements using PXRD.

A number of PXRD tests were conducted during the study to determine the susceptibility of the technique to various parameters. The WH method is commonly used for primary PXRD analysis due to its simplicity, but it relies on the assumption of isotropic peak broadening. It is necessary for a qualitative investigation of peak broadening behaviour, and the crystallite size affects the peak width. The Rietveld method does not properly determine the FWHM for each diffraction peak, as it only provides a mean description of a full-line profile. It accounts for crystallographic anisotropy in the phases. (Juan Macchi, 2021). However, variations instrumentation modelling performed to ensure accurate pattern fitting explored in Section 4.2.2 minimises the limitation of the technique. Using the instrumental resolution function and a LaB_6 strain-free standard with a crystallite size of 800nm using different approaches in TOPAS enabled the extraction of realistic micro-strain and crystallite sizes. Therefore, it can be inferred that the Rietveld refinement method using TOPAS does not support isotropic modelling as it may lead to the introduction of an excessive number of parameters in the modelling, resulting in over-fitting of data, which may result in meaningless values extracted from the model. If allowed, these values may have non-physical values in the data, making the approach adopted in this study more conservative.

The study resolved that there is good agreement between the two methods in ranking material states based on micro-strain levels, as demonstrated in Figure 29. It has been concluded that both methods are capable of ranking different material states within limitations. The use of PXRD analysis with the TOPAS analysis showed that the pattern fitting methodology utilized with option 3 is more accurate and has less scatter in extracting micro-strain and crystallite size. However, it is essential to establish a measurement protocol to ensure the accuracy of results. The four main areas identified that tend to influence the results are as follows:

a) Instrument - A quality check of the instrumentation is performed using the standard material to eliminate any problems associated with the instrument. Random changes made to the diffractometer such as slits, etc, affect the results.
b) Polishing - Inconsistencies in sample preparation; mechanical polishing has the potential of leaving some damage in the material specimen undergoing analysis. The application of electropolishing, as realised in the study, there is no chance of scratching or mechanical

deformation on the samples. This is further proven by the standard quality check performed prior to observing the samples.

c) Repeatability - Three data points per sample have been chosen for this study. This provides additional accuracy for the information that is required. Further, the scans were repeated to ensure consistency in the data.

d) Sample height - Figure 41 shows an example of two scans performed as part of this study. The scans showed significant strain values; this observation was impacted by the sample height of the evaluated specimens with a 0,2 mm difference; however, a significant change in the position peak was observed. The sample height is also influenced by the mounting of the sample into the instrument. Therefore, a functional sample holder that eliminates the discrepancies in height is desirable.

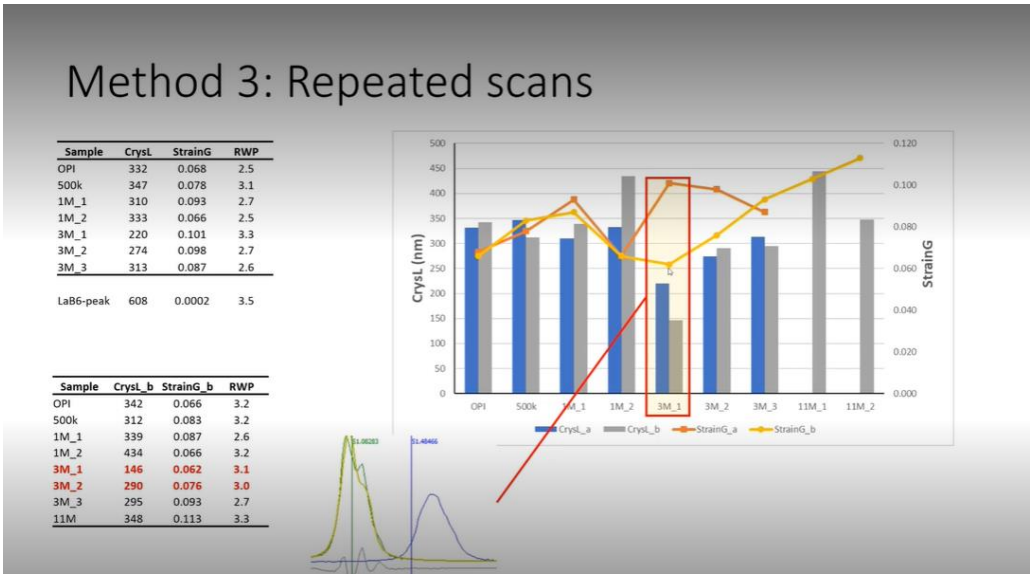

Figure 41: Effect of sample height on micro-strain scan data.

e) Optimal TOPAS fitting methodology – The four methods explored in Section 4.2.2 to select that best methodology of accurately accounting for instrumentation broadening is of utmost importance. This is to ensure that all parameters are physically verifiable to deliver an optimal pattern fit is key.

f) Absence or wrong calibration standard - Early samples tested at Witwatersrand University using a Si reference, while UCT used an Al_2O_3 showed discrepancies. These standards aim to verify whether the peaks are at the correct positions and are not suitable for micro-

strain calibrations. Literature as well as this study has shown that the LaB_6 NIST standard is most suitable.

These external factors can lead to variations in the material state that can be distinguished by PXRD. However, PXRD can be used to distinguish whether the differences in dislocation density are sufficiently large. In this ideal case, model steel was used, where the samples were deliberately made with large changes in the material. However, power-plant steels may exhibit smaller changes in their material states. If these changes are less than 0,02µm strain, then is really at its boundary in terms of distinguishing between material states. EBSD may better discriminate between the material states. This may fall under future work or may have been partially modelled in this study. However, this technique requires scanning of more areas.

The PXRD study explored a number of ways to extract critical parameters for the quantification of fatigue damage in the stainless steel. In the first analysis, a Gaussian curve is fitted to the peak; however, in nature, the peak profile shape is more complicated, and it is not Gaussian. The Rietveld Refinement method considers the shape parameters of the peaks, but still assumes isentropic broadening of the crystallite. Fundamentally, this is not a reality for all materials, especially FCC materials. However, the establishment of a controlled pattern fitting approach coupled with the outcome of rational accurate dislocation density values as established in this study gives confidence in the methodology to be followed when performing similar work.

7.3 Advantages of using PXRD techniques over historical techniques utilised.

Chapters 5 and 6 discuss techniques for deformation analysis using EBSD and TEM, respectively. EBSD uses strain-induced misorientation evolution and four parameters for evaluation, while TEM provides a semi-quantitative analysis of dislocations from micro-graphs. These techniques can provide comparative data from a single specimen and test compared to several conventional test pieces and tests. Table 10 compares the mean dislocation density (deformation) that can be resolved using TEM with the average micro-strain per material state calculated using PXRD. While the average and mean have similar mathematical definitions, they are fundamentally different in statistics. By ranking the six material states according to the level of deformation in the sample, with 1 representing the specimen with the least deformation and 6 having the maximum level of deformation, the table shows that both methods of analysis consistently rank the as received and

annealed specimens as having the most and least level of deformation, respectively. However, for the fatigued specimen, there was no consistency in the deformation ranking between the methods used. Additionally, the 500k cycled and 1 million cycled specimens had similar levels of deformation according to PXRD analysis, but the mean dislocation density was very close between the specimens, while the average micro-strain was significantly different. The 3 and 11 million cycled specimens were also very close to each other, despite inconsistent raking.

Table 10: Ranking of all specimens using PXRD and TEM for level of deformation.

	ANNEALED	500k CYCLES	1 MILLION CYCLES	3 MILLION CYCLES	11 MILLION CYCLES	EXTRUDED
Mean dislocation density using TEM Analysis.	3.445E+13	5.645E+13	5.530E+13	6.425E+13	6.775E+13	1.0155E+14
Average dislocation density using PXRD.	2.626E+12	5.837E+12	7.6642E+12	1.305E+13	8.65881E+12	4.653E+13
Ranking on TEM results	1	3	2	4	5	6
Ranking on PXRD results	1	2	3	5	4	6

While it is acknowledged that the deformation (i.e. dislocation density) measurement using PXRD is qualitative due to the modelling of line broadening effects resulting from crystallite size and lattice strain, and the analysis of these effects using the double-Voigt approach, which involves both Lorentzian and Gaussian components to eliminate instrumental contributions to peak broadening, it should be noted that the TEM analysis involved the manual counting of dislocations in TEM images, which includes a level of qualitative assessment of the dislocation density in the material sample. TEM is well-suited to interpret heterogeneous microstructures and is especially suited to measure lower dislocation densities, while PXRD is less reliable for these low densities. PXRD can provide average data for larger specimen volumes than TEM, but it cannot account for microstructural heterogeneity. PXRD data supports the TEM results in the

present study, which have limited statistical power on their own. Due to the limitations of the TEM technique, advanced techniques in scanning electron microscopes are employed to overcome these restrictions.

Although PXRD analysis provides information from larger material volumes than TEM measurements, it becomes less accurate for low dislocation densities because more dislocations are needed to produce significant broadening. The interpretation of PXRD data assumes a homogeneous distribution of dislocations, which only applies to martensitic material states and short/intermediate temperature times. TEM is better suited to interpret heterogeneous microstructures and measure lower dislocation densities. PXRD provides average values for larger specimen volumes than TEM can investigate, but dislocation counting by TEM is limited by its local scope and the possibility that dislocations in the specimen might slip away from the surface (Masumura, 2022).

This section equally explores the sensitivity of the PXRD technique compared to EBSD by discussing its ability to rank different material states, the precision of the techniques, and the limitations of the technique in the context of this study. Back-scatter imaging requires high magnification and the ability to zoom in on grains, and the dislocations can only be seen in crystals at a specific orientation. Despite the SEM micrographs being taken without knowledge of the individual crystallographic orientation of the specimen, many grains were in good condition for imaging dislocation arrangements without additional tilt or rotation of the specimen. In Chapter 5, it was shown that EBSD was more accurate in determining the deformation level in the specimen. However, the analysis was limited to qualitative modelling of the KAM, GROD and misorientation to mean. A quantitative EBSD study has the potential to complement PXRD in the local and global characterization of the microstructure, revealing the complementary nature of the two techniques as demonstrated in this study. Additionally, distinctive evaluation of dislocation types can be achieved in both techniques.

7.4 Recommendations for future work

To support the country's demand for reliable power plant operations and the integration of clean energy technologies, material asset management must be greatly expanded by minimizing and preventing material failure challenges through proven science-based condition assessment methods. Industries such as the electricity generation utilities which are dominant players in the generation, transmission and distribution of electrical energy in Southern Africa will often face

potential threats as a result of policy changes in the energy sector. This work aims to address such utilities by suggesting advanced methods of asset and/or component management.

In particular, the steam turbine fleet is one system that has the potential of benefiting in the evaluation of non-destructive technique methodology such as PXRD. As the turbine fleet ages, new demands are being placed on these systems and their critical sub-components such as low-pressure turbine last stage blades. These include the operation of the components in a cycling mode to counter for additional capacity from other uses. Therefore, operators are experiencing increasing incidences of turbine starts. The development of this technique has the potential to provide operator guidelines on the performance of non-destructive evaluation (NDE) to enable the risk-based management of last stage blades through plant inspections and modelling. The use of appropriate NDE methods is a crucial approach to the detection and mitigation of component life fraction including reducing failures and improving availability.

Previous work in the field investigated the relationship between cyclic fatigue properties and the microstructural evolution for a 12% Cr ferritic-martensitic steel material used in steam tubing and turbine parts and resolved that material with high dislocation densities exhibits specific mechanical properties which results in a softening behaviour when exposed to cyclic loading and a strong decrease of creep rate in very small strain intervals during primary creep (Zhang, 2016). Furthermore, literature has proven that the possibilities of X-ray diffraction technique in the field of the material degradation extent during fatigue loading where the material damage curves evaluated experimentally on the basis of the X-Ray diffraction were in a good agreement with the course of damage in dependence on acting load and resulting cycles to failure (Fiala, 2009) which provided a framework for this study. Chapter 4 thus evaluated the quantification of dislocation density via the PXRD method as a result of the broadening of diffraction peaks that occurs when atoms in crystal unit cells are displaced from their ideal position due to small crystallite below one micrometre and an abundance of lattice defects such as dislocations (Muiruri, 2020) with the aim of evaluating dislocation density and the crystallite size, the PXRD coherent domain using a best fit the diffraction peaks analytical methods. Although this evaluation approaches were tested on AISI 316L stainless steel, in this work, certain aspects can be directly translated to the assessment of a steam turbine blade material.

The visualisation of condensed dislocation arrangements near the surface of bulk specimens, such as dislocation walls/cells after fatigue, makes the electron channelling contrast imaging

(ECCI) technique a good candidate for characterising microstructures after plastic deformation. The incorporation of this technique can also aid in damage evaluations of ex-service material, not only limited to X-Ray diffraction. Furthermore, broadening the TEM analysis to include the measurement of foil thickness and tilting of foils for visualisation can enhance the accuracy of dislocation measurements. These studies will assist the industry in developing more accurate and less conservative damage evolution rate models, leading to informed maintenance decisions and cost and service continuity benefits.

Additionally, a more sophisticated X-ray diffractometer that has a monochromator can be utilised to reduce the instrumental line contributions and get eliminate the peak doublet. This feature will distinguish between samples with lower dislocation density differences.

Chapter 8. Conclusions

This research was prompted by the necessity to evaluate the X-ray diffraction technique in assessing deformation in a metastable stainless-steel alloy, with the objective of comprehending the sensitivity of the non-destructive technique in relation to other complementary material evaluation techniques, as discussed in Chapter 1. A cyclic loading experimental setup that mimics actual operating conditions was created to determine the limitations of the model material through forced controlled fatigue testing. Subsequently, the data was utilized to establish multiple material states as baseline stage gates for the evaluation of the extent of deformation in each material state. PXRD analysis of the material states was carried out using a whole pattern fit method in TOPAS collected on a Bruker D2 Phaser diffractometer and the Williamson-Hall plot methods to determine the micro-strain and crystallite size of the specimen. This data was compared to the quantitative analysis of the EBSD and TEM deformation characteristics for each material state. The focus of this work was the validation of the PXRD technique sensitivity in relation to the EBSD and TEM microscopy analysis. The results revealed the need for increased signal input in the material states to enable the identification of more pronounced deformation or material state differences across all microscopy techniques.
The key conclusions are outlined below:

- The selection of AISI316L austenitic stainless steel, uniaxial fatigue specimen design, and cyclic stress range has resulted in a desirable S-N curve, which serves as a basis for identifying damage using PXRD and electron microscopy. All specimen failures occurred at cycles lower than 10,000, indicating low cycle fatigue and high stresses close to the material's ultimate tensile strength. Further analysis of fracture surface characterization could potentially provide an S-N curve indicating the number of cycles for crack initiation.

- The SEM-EBSD analysis shows potential for providing semi-quantitative damage characterization, which can be compared with the quantitative PXRD strain analysis. During EBSD analysis, it was found that local misorientation developed due to cyclic and uniform strain and that its spatial distribution was not uniform. In fatigue samples, the large local

misorientation tended to form clusters, whereas it was localized to grain boundaries in tensile samples. The degree of localization increased with strain amplitude, and statistical processing was used to quantify it. The source of damage (cyclic or uniform strain) and loading direction could also be deduced from EBSD observations of the damaged sample. It was concluded that EBSD results show mostly good qualitative agreement with PXRD analysis but enhancing the scale of measurement can reveal the heterogeneous distribution of deformation in the microstructure.

- However, the use of TEM diffraction also has limitations. The results may have large scatter and extracting data from image scans can be time-consuming. Despite these challenges, TEM diffraction shows good potential for quantitative damage characterization, which can be compared with the quantitative PXRD strain analysis.

- During PXRD peak-profile analysis, it was determined that the accuracy and precision of extracted parameters such as crystallite size and dislocation density are sensitive to data fitting methods, sample surface preparation, and the material state. The results indicate that the PXRD technique used is viable for determining dislocation density if the material states are sufficiently different. However, standardization of sample preparation, instrument calibration, and data processing pipeline is crucial for reliable measurements. The PXRD technique is not dependable for detecting small increments in accumulated fatigue damage to monitor the damage over a period of operating life and signal imminent risk. It is also important to consider that real-life operation involves a much more complex material than the simple material presented in this study.

- The extrapolation of the PXRD results and the application to a turbine blade actual real material (X20Cr13) from the model alloy (AISI 316L) requires considering the material's microstructure. This martensitic stainless steel has a starting microstructure with high dislocations, and the mechanism of dislocation movement will differ due to some dislocations moving at the operating environment and aggregating into domain walls. Consequently, a decrease in micro-strain and an increase in crystallite size are expected. The mechanism of dislocation movement is different and must be understood. In service, X20Cr13 has smaller grains and is affected by temperature, while this study starts with zero or very little dislocations at room temperature. At high temperatures, the mechanism of fatigue will differ

due to inherent pre-existing dislocations compared to a starting point with dislocations at room temperature. However, if there is a 0.02 difference in micro-strain from the starting point, PXRD should be able to detect it. Literature shows that X20Cr13 material has micro-strain scatter in the region of 0.08. Therefore, if changes in micro-strain are large enough in service, PXRD can detect them. Additionally, the TOPAS analysis in the study assumes isotropic broadening of the microstructure, while the martensitic microstructure consists of grains that are not fully annealed and have too much tetragonality.

- The accuracy of dislocation density results is limited by the dislocation pole structure and approximations of the physical models for fitting the peak profiles and the instrument have a potential to affect the resultant dislocation density values.

Bibliography

Ali, A., 2022. X-ray Diffraction Techniques for Mineral Characterization: A Review for Engineers of the Fundamental, Applications, and Research Directions. *Minerals,* 12(205).

Ameh, E., 2019. A review of basic crystallography and X-Ray diffraction applications. *International Journal of Advanced Manufacturing Technology,* Volume 105, pp. 3289-3302.

Anon., 2008. *Dissemination of IT for the promotion of Material Science (DoITPoMs).* [Online] Available at: https://www.doitpoms.ac.uk/tlplib/dislocations/observing.php [Accessed 15 October 2022].

Argon, A., 2007. *Strengthening Mechanism in Crystal Plasticity.* USA: Oxford.

B.C. Nzogang, J. B. P. C. ,. A. M. ,. J. G. a. S. K., 2018. Characterization by Scanning Precession Electron Diffraction of an Aggregate of Bridgmanite and Ferropericlase deformed at HP-HT. *Geochemistry, Geophysics, Geosystems,* Volume 19, pp. 582-594.

Balzar, D., 2004. Size-strain line-boardening analysis of teh ceria round tobin sample. *Journal of Applied Crystallography,* Volume 37, pp. 911-924.

Balzar, e. a., 2004. Size–strain line-broadening analysis of the ceria round-robin sample. *Journal of Applied Crystallography,* 37(6), pp. 911-924.

Banerjee, D., 2007. *IIT Kanpur.* [Online] Available at: chrome-extension://efaidnbmnnnibpcajpcglclefindmkaj/https://www.iitk.ac.in/che/PG_research_lab/pdf/resources/XRD-reading-material.pdf [Accessed December 2022].

Binyan, H., 2013. The Effects of Shot Peening on Short Crack Growth Rate and Resulting Low Cycle Fatigue Behaviour in a Low Pressure Turbine Blade Material. *Materials Science and Technology,* 29(7), pp. 788-796.

Booysen, C., 2015. Fatigue life assessment of a low pressure steam turbine blade during transient resonant conditions using a probabilistic approach. *International Journal of Fatigue,* Volume 73, pp. 17-26.

Borbely, A., 2022. The modified Williamson-Hall plot and dislocation density evaluation from diffraction peaks. *Scripta Materialia,* Volume 217.

Borzi, A., 2020. Microstructure analysis of epitaxial BaTiO3 thin films on SrTiO3- buffered Si: Strain and dislocation density quantification using HRXRD methods. *Materialia,* Volume 14.

Brewer L.N., 2006. Misorientation mapping for visualization of plastic deformation via electron back-scattered diffraction. *Microsc Microanal,* 12(1), pp. 85-91.

Bunaciu, A. 2015. X-Ray Diffraction: Instrumentation and Applications. *Critical Reviews in Analytical Chemistry,* 45(4).

C.E. Feltner, C. L., 1967. Cyclic strain response of FCC metals and alloys-I Phenogical experiments. *Acta Metallurgica,* Volume 15, pp. 1621-1632.

Catlow, C., Richard, A., Synchrotron radiation techniques in materials and environmental sciencePhil. Trans. R. Soc. A.37320130162, 2015, http://doi.org/10.1098/rsta.2013.0162

Chandrasekhar, S., 2000. *The Enigma of Bragg's Law,* India: Department of Organic Chemistry, Indian Institute of Science.

Cheary, R. C. A., 1992. A fundamental parameters approach to X-Ray line profile fitting. *Journal of Applied Chrystalography,* 25(2), pp. 109-121.

Cheary, R., 2004. Fundamental Parameters Line profile Fitting in Laboratory Diffractometers. *Journal of Research of the National Institute of Standards and Technology,* Volume 109, pp. 1-25.

Cline J.P., 2015. The optics and alignment of the divergent beam laboratory X-ray powder diffractometer and its calibration using NIST standard reference manual. *Journal of Research of teh National Institute of Standards and Technology,* Volume 120.

Connolly, J. R., 2007. Introduction to X-Ray Powder Diffraction. *EPS400-001.*

Cullity, B., 2014. *Elemets of X-Ray Diffraction.* Third Edition ed. England: Pearson.

David B. Williams, 2009. *Transmission Electron Microscopy: A Textbook for Materials Science.* New York: Springer.

de Keijser, T., 1982. Use of the Voigt function in a single-line method for teh analysis of X-ray diffraction line broadening. *Journal of Applied Crystallography,* Volume 15, pp. 308-314.

Delobbe, A., 2014. High speed TEM sample preparation by Xe FIB. *Microscopy and Microanalysis,* 20(S3), pp. 298-299.

Dolabella, S. B. A. D. A. N. A., 2022. Lattice Strain and Defects Analysis in Nanostructured Semiconductor Materials and Devisesby High Resolution XRD: Thoretical and Practical Aspects. *Small Methods,* Volume 6.

Dutta, S., 2013. Comparison of residual stress in deep boron diffused silcon (100), (110) and (111) wafers. *Materials Letters,* Volume 100, pp. 44-46.

Elstad, K. A. B. K. M. W. I. H. J., 2016. *The Effect of Sample Preparation on Quantification of Retained Austenite in Supermartensitic Stainless Steel Studied by EBSD and XRD.* Rhodes, Greece, International Society of Offshore and Polar Engineers.

Endrenyi, J., 2001. The Present Status of Maintenance Strategies and the impact of maintenance on reliability. *IEEE Transactions on Power Systems,* 16(4).

EPRI, 2020. *Nondestructive Evaluation Methods - Application to Power Plant Steam Turbine Systems,* s.l.: Electric Power Research Institute.

F. Christein, M. T. K. K., 2013. Neutron diffraction in-situ monitoring of teh dislocation density during martensitic transformation in a stainless steel. *Scripta Materials,* Volume 68, pp. 506-509.

Fahlman, B. D., 2011. Material Characterization. *Material Chemistry,* pp. 585-667.

Fernadez-Galiana, 2023. Fundamentals and Applications of Ramn-Based Techniques for teh design and developement of active biomedical materials. *Advanced Materials.*

Fiala, J. M. V., 2009. Evaluation of fatigue damage by X-Ray diffraction technique of steam turbine rotor steels at elevated temperatures. *Proceedings of the ASME 2009 Pressure Vessels and Piping Division Conference.*

Fukuya, K., 2013. Local strain distribution near grain boundaries under tensile stresses in highly irradiated SUS316 stainless steel. *Journal of Nucleur Materials,* Volume 432, pp. 67-71.

G.K. Williamson, R. S., 1956. Dislocation densities in some annealed and cold-worked metals from measurements on teh X-Ray debye-scherrer spectrum. *Philosophical Magazine,* 1(1), pp. 34-46.

Garcia-Mateo, C., 2016. Analyzing the scale of the bainitic ferrite plates by XRD, SEM and TEM. *Materials Characterization,* Volume 122, pp. 83-89.

Gardiner, D., 1989. *Patrical Raman Spectroscopy.* Germany: Springer-Verlag.

Gedeon, M., 2013. Characterization of Fatigue Behaviour. *Materion Brush Performance Alloys Technical Tidbits Issue 54*, June.

Gedeon, M., 2013. Fatigue and Stress Ratios. *Materion Brush Performance Alloys Technical Tidbits Issue no. 53*, May.

George Crowly, 2019. Quantitative lung morphology: semi-automated measurement of mean linear intercept. *BMC Pulm Med,* 19(206).

Girard, G., 2020. Development of Bragg coherent X-Ray diffraction and ptychgraphy methods. *Materials Science.*

Girgsdies, F., 2006. *Peak Profile Anlysis in X-Ray Powder Diffraction,* Berlin: Electron Microscopy Group.

Godfrey, A. C. W. L. Q. H. N., 2005. Stored energy, microstructure, and flow stress of deformed metals. *Metallurgical and Materials Transactions A,* Volume 36, pp. 2371-2378.

Groma, I., 1998. X-ray line broadening due to an inhomogeneous dislocation distribution. *Physical review B,* 57(13).

Guo, Y. B. T. W. A., 2014. Slip band-grain boundary interactions in commercial-purity titanium. *Acta Materialia,* Volume 76, pp. 1-12.

Gussev, M. L. K., 2019. In situ SEM-EBSD analysis of plastic deformation mechanisms in neutron-irradiated austenitic steel. *Journal of Nucleur Materials,* Volume 517, pp. 45-56.

Haghshenans, A., 2018. Damage accumulation and crack initiation detection based on the evolution of surface roughness parameters. *International Journal of Fatigue,* Volume 107, pp. 130-144.

Halder, N. W. C., 1966. Separation of paricle size and lattice strain in integral breadth measurements. *Acta Crystallographica,* Volume 20, pp. 312-313.

Hammond, C., 2009. *The Basics of Crystallography and Diffraction.* Third Edition ed. UNiversity of Leeds: Oxford Science Publications.

TY - JOUR

Hanke, R., Fuchs, T.,Uhlmann, N., X-ray based methods for non-destructive testing and material characterization, JO, 2008, Volume 591, pp 14-18.

Hargreaves, J., 2016. Some consideration related to the use of tthe Scherrer equation in powder X-ray diffraction as applied to heterogenous catalysts. *Catalysis, Structure & Reactivity,* 2(1-4), pp. 33-37.

Harrington, G. S. J., 2021. Back-to-Basics tutorial: X-ray diffraction of thin films. *Journal of Electroceramics,* Volume 47, pp. 141-163.

Hart, M., 1981. Bragg angle measurement and mapping.. *Journal of Crystal Growth,,* 55(2), pp. 409-427.

Hertzberg, R., 1967. Fatigue fracture surface appearance. *ASTM STP 415,* pp. 205-225.

Hindson, J. S. Z. H.-G. J. M. P. G. N., 2011. Morphological study of nanoparticle polymer solar cells using high-angle annular dark-field electron tomography. *nano Letters,* Volume 11, pp. 904-909.

J. I. Langford, D. L. a. P. S., 2000. Effect of a crystallite size distribution on X-ray diffraction line profiles and whole-powder-pattern fitting. *Journal of Applied Crystallography ,* Volume 33, pp. 964-974.

J.F. Falth, M. G. X. L. T. A. I. I. B. M. H. Y. S. W., 2005. Influence of dislocation dnesity on photoluminescence internsity of GaN. *Journal of Crystal Growth,* Volume 278, pp. 406-410.

J.P. Cline, D. B. D. G. A. H. D. W., 2010. The application of teh fundamental parameters approach as implemented in TOPAS to divergent beam powder diffraction data. *Materials Science Forum,* Volume 651, pp. 201-219.

J.Z. Lu, W. D. K. L. L. W. H. L., 2017. Surface EBSD analysis and strengthening mechanism of AISI304 stainless steel subjected to massive LSP treatment with different pulse energies. *Materials Charactrization,* Volume 125, pp. 99-107.

Jahil, S. M. I. K. A. J. K. H. K., 2022. Application the Halder – Wagner to Calculation Crystal Size and Micro Strain by X0ray diffraction peaks analysis. *NeuroQuantology,* Volume 20(Issue 1), pp. Page 199-204.

JM Cowley, Y. H., 1992. De-chanelling contrast in annular dark-field STEM. *Ultramicroscopy,* 40(2), pp. 171-180.

Juan Macchi, S. G. G. G. J. T. S. D., 2021. Dislocation densities in a low-carbon steel during martensite transformation determined by in situ high energy X-Ray diffraction. *Materials Science & Engineering,* Volume 800.

K. Hashimoto, H. M., 1983. The role of elastic interaction stresses on teh onset of slip in polycrystalline alpha brass. *Acta Metallurgica,* Volume 31.

Kamaya, M., 2009. Measurement of local plastic strain distribution of stainless steel by electron backscatter diffraction. *Materials Characterization,* Volume 60, pp. 125-132.

Kamaya, M., 2012. Assessment of local deformation using EBSD: Quantification of local damage at grain boundaries. *Materials Characterization ,* Volume 66, pp. 56-67.

Kamaya, M., 2015. Loading sequence effect on fatigue life of Type 316 stainless steel. *International Journal of Fatigue,* Volume 81, pp. 10-20.

Kandemir T., K. i. G. F. Z. S. K. S. T. M. S. R. &. B. M., 2014. Microstructural and defect analysis of metal nanoparticles in functional catalysts by diffraction and electron microscopy: The Cu/ZnO catalyst for methanol synthesis. *Topics in Catalysis,* Volume 57, pp. 188-206.

Karuthapandian, S., 2017. Effective Photodegradation of CR & MO dyes by morphologically controlled Cerium oxide nanocubes under visible light Illumination. *Optik,* Volume 154.

Kim, J. S. S. K. H. K. B. P. M. O. S. K. D., 2023. Ptychographic lens-less birefrigence microscopy using a mask-modulated polarization image sensor. *Sci Rep,* Volume 13.

Kostka, A. T. K. H. R. E. Y. E. G., 2007. On teh contribution of carbides and micrograin boundaries to the creep strength of tempered martensite ferritic steels. *Acta Materialia,* Volume 55, pp. 539-550.

Kostka, A. T. K. H. R. E. Y. E. G., 2007. On the contribution of carbibes and micrograin boundaries to the creep strength of tempered martensite ferritic steels. *Acta Materialia,* Volume 55, pp. 539-550.

Koyama M., S. M. N. K. a. T. K., 2021. Stacking fault aggregation during cooling composing FCC–HCP martensitic transformation revealed by in-situ electron channeling contrast imaging in an Fe-high Mn alloy. *Sci Technol Adv Mater,* 22(1), pp. 135-140.

Kumar, A. R. M., 2021. *The Handbook of Reliability, Maintenance, and System Safety Through Mathematical Modeling.* Netherlands: Elsevier Science.

L.C.F. Canale, J. V. G. T., 2014. Introduction to Steel Heat Treatment. *Comprehensive Materials Processing,* Volume 12, pp. 3-37.

Landau, P., 2010. In-situ TEM study of dislocation patterning during deformation in single crysta aluminium. *Journal of Physics: Conference Series,* Volume 241.

Langford, J. W. A., 1978. Scherrer after sixty years: a survey and some new results in the determination of crystalline size. *Journal of Applied Crystallography,* Volume 11, pp. 102-113.

Lehto, P., 2021. Adaptive domain misorientation approach for the EBSD measurement of deformation induced dislocation sub-structures. *Ultramicroscopy,* Volume 222.

Leoni, M., 2012. Information on Imperfections. In: U. Kolb, ed. *Uniting Electron Crystallography and Powder Diffraction.* Italy: Springer.

Lu, J. D. W. L. K. W. L. a. L. H., 2017. Surface EBSD analysis and strengthening mechanism of AISI304 stainless steel subjected to massive LSP treatment with different pulse energies. *Materials Characterization,* Volume 125, pp. 99-107.

M. Calcagnotto, D. P. E. D. D. R., 2010. Orientation gradients and geometrically necessary disclocations in ultrafine grained dual-phased steels studied by 2D and 3D EBSD. *Material Science & Engineering,* A(527), pp. 2738-2746.

M. Odnobokova, Z. Y. R. K., 2020. On the strength of a 316L-Type stainless steel subjected to cold or warm rolling followed by annealing. *Materials,* Volume 13.

M.S. Pham, S. H. K. J. E. M., 2013. Cyclic deformation response of AISI316L at room temepreature: Mechanical behaviour, microstructural evolution, physicaly-based evolutionary constitutive modelling. *International Journal of Plasticity,* Volume 47, pp. 143-164.

Maksimov, V. M. E. S. T. P. V., 2020. Evolution of a Non-Uniform Deformed Satte in teh Structure of Zinc Chalcogenide Cubc Crystals Doped by #d ions. *Journal of Surface Investigation: X-ray, Synchrotron and Neutron Techniques,* Volume 14, pp. 31-41.

Malis, T. C. S. a. E. R., 1988. The EELS Log-ratio Technique for Specimen-Thickness Measurement in the TEM. *J. Electr. Microsc. Tech.,* Volume 8, p. 193–200..

Marinkovic B., R. d. A. R. S. A. C. R. A. F., 2001. A comparison between the Warren-Averbach method and alternate methods for X-ray diffraction microstructure analysis of polycrystalline specimens. *Mat. Res.,* 4(2).

Marinkovic, B. d. A. R. S. A. A. F., 2001. A comparison between the Warren-Averbach method and alternate methods for X-Ray diffraction microstructure analysis of polycrystalline specimens. *Materials Research,* Volume 4, pp. 71-76.

Masumura, T., 2022. Quantitative evaluation of dislocation density in as-quenched martensite with tetragonality by X-ray line profile analysis in a medium-carbon steel. *Acta Materialia,* Volume 234.

Mccloskey, T. H., 1999. *Turbine Steam Path Damage: Theory and Practice Volume 1: Turbine Fundamentals,* s.l.: EPRI.

Miedema, P. S., 2017. Raman Spectroscopy with X-Rays. In: M. Khan, ed. *Raman Spectroscopy and Applications.* Pakistan: Intech, p. 364.

Mishra, S. R. H. L. A. S. S. T. S. D. K., 2015. A comparative assessment of crystallite size and lattice strain in differently cast A356 aluminium alloy. *IOP Conference Series: Matreials Science and Engineering,* Volume 75.

Misture, S. S. R., 2001. Profile Fitting and Rietveld Analysis. In: *Encyclopedia of Materials: Science & Technology.* s.l.:s.n.

Mittemeijer E.T., S. P., 2004. *Diffraction Anlysis of the Microsructure of Materials.* s.l.:Springer.

Morito, S. N. J. M. T., 2003. Dislocation density within lath martensite in Fe-C and Fe-Ni alloys. *ISIJ International,* Volume 43, pp. 1475-1477.

Muiruri, A. M. M. d. P. W., 2020. Evaluation of Dislocation Densities in Varius Microstructures of Additively Manufactured Ti6Al4V (Eli) by teh Method of X-Ray Diffraction. *Materials,* Volume 13.

Muniz, F., Miranda, M., MOrilla dos Santos, C. & Sasaki, J., 2016. The Scherrer equation and the dynamical theory of X-ray diffraction. *Acta Cryst.,* A(72), pp. 385-390.

Nasiri, S. R. M. P. A. J. G. V. A. N. V. M. A., 2023. Nasiri, S., Rabiei, M., Palevicius, A., JanusasModified Scherrer equatiion to calculate crystal size by XRD with high accuracy, examples Fe2O3, TiO2 and V2O5. *Nano Trends,* Volume 3.

Nations, U., 2015. *Transforming our world: The 2030 agenda for sustainable development,* NY, USA: A/RES/70/1.

Nicolas Brodusch, S. B. E. B. d. M., 2021. Scanning Electron Microscopy versus Transmission Electron Microscopy for material characterization: A comparative study on high-strength steels. *Scanning,* Volume 4.

Ou, X., Qin, X., Huang, B. et al. High-resolution X-ray luminescence extension imaging. Nature 590, 410–415 (2021). https://doi.org/10.1038/s41586-021-03251-6

Padilha, A. P. R. R. P., 2003. A Review: Annealing of Cold-worked Austenitic Stainelss Steels. *ISIJ International,* Volume 43, pp. 135-143.

Pan, Z. D. C. &. S. R., 1994. Measurement of foil thickness in transmission electron microscopy. *Journal of Material Science,* Volume 29, pp. 1920-1924.

Paolo, S. L. M., 2002. Whole powder pattern modelling. *Acta Crystallographica Section A,* 58(2), pp. 190-200.

Peckner, D. a. B. I., 1977. *Handbook of Stainless Steel.* University of Michigan: Mc Graw Hill.

Pesicka, J., 2010. How dislcoations substructures evolve during long-term creep of a 12% Cr tempered martensitic ferritic steel. *Scripta Materialia,* Volume 62, pp. 353-356.

Pesicka, J. R. K. A. D. G. E., 2003. The evolution of dislocation density during heat treatment and creep of tempered martensite ferritic steels. *Acta Materialia,* Volume 51, pp. 4847-4862.

Peterson, V. K., 2005. Lattice parameter measurement using Le Bail versus structural (Rietveld) refinement: A caution for complex, low symmetry systems. *Powder Diffraction,* 20(1), pp. 14-17.

Pinheiro, B. L. J. P. I. B. E. B. E., 2013. X-ray diffraction of microstructural changes during fatigue damage initiation in pipe steels: Role of the initial dislocation structure. *Materials Science & Engineering,* Volume 580, pp. 1-12.

Plesiutschnig, E., 2016. Fracture analysis of a low pressure steam turbine blade. *Case Studies in Engineering Failure Analysis,* 5(6), pp. 39-50.

R. Bergmann, R. C. R. H. J. P. G. S., 2016. Restoration of manifold-valued images by half-quadratic minimization. *Inverse Probl. Imaging,* Volume 10, pp. 281-304.

Rabiei, M. P. A. M. A. N. S. V. A. J. G., 2020. Comparing Methods for Calculating Nano Crystal Size of Natural Hydroxyapatite Using X-Ray Diffractio. *Nanomaterials,* 10(9).

Radamson, H., 2023. X-Ray Techniques. In: Cham, ed. *Analytical Methods and Instruments for Micro-and nanomaterials.* s.l.:Springer.

Randle, V., 2009. Electron backscatter diffraction: Strategies for reliable data acquisition and processing. *Materials Characterization ,* Volume 60, pp. 913-922.

Ren, Y., Xie, Y., Chen, Z.i, Ma Z., Applications of synchrotron X-rays and neutrons diffraction in energy storage materials research, Energy Storage Science and Technology, 2017, Vol. 6, Issue (5), pp 855-863.

Rezaei, E., 2017. A new model for the optimization of periodic inspection. *Case Studies in Engineering Failure Analysis,* Volume 9, pp. 148-156.

Rietveld, H., 1967. Line profiles of neuro powder-diffraction peaks for structure refinement. *Acta Crystallographica,* 22(1), pp. 151-152.

Saadi, S. A. I. K. A. J. K. H. K., 2022. Application the Halder – Wagner to Calculation Crystal Size and Micro Strain by Z-ray Diffraction Peaks Analysis. *Neuro Quantology,* 20(1), pp. 199-204.

Santecchia, E. e. a., 2016. A Review on Fatigue Life Prediction Methods for Metals. *Advances in Materials Science and Engineering,* p. 26.

Sardela, M., 2014. X-Ray Diffraction and Reflectivity. In: U. o. Illinois, ed. *Practical Materials.* New York: Springer.

Sauzay, M., 2011. Scaling laws for dislocation microstructures in monotonic and cyclic deformation of fcc metals. *Progress in Materials Science,* Volume 56, pp. 725-784.

Scheepers, R., 2014. *Hendrina LP Turbine L0 Blades,* Johannesburg: Eskom.

Scherrer, P., 1918. Determination of teh size and internal structure of colloid paricles usin X-rays, News from the Society of Sciences in Gottingen. *Mathematical-Physical Class,* pp. 98-100.

Scherrer, P., 1918. Nachrichten von der Gesellschaft der Wissenschaften zu Göttingen. *Mathematisch-Physikalische Klasse,* Volume 2, pp. 98-100.

Schwartz, A. K. M. A. B., 2000. *Electron Backscatter Diffraction in Materials Science.* 2nd ed. Livermore CA: Springer.

Schwenk, M., 2014. Residual Stresses and Distortion in Quenched and Tempered Steels. In: J. L. Dossett, ed. *Steel Heat Treating Technologies.* s.l.:ASM, p. Volume 4B.

Shao-Shi Rui, Y.-B. S. Y.-N. F. Q.-N. H. L.-S. N. H.-J. S. K. H. N. K., 2018. EBSD analysis of creep deformation induced grain lattice distortion: A new method for creep damage evaluation of austenitic stainless steels. *Materials Science & Engineering,* A(733), pp. 329-337.

Shojaati, M., 2020. The heat affected zone of X20Cr13 martensitic stainless steel after multiple repair welding: Microstructure and mechanical properties assessment. *International Journal of Pressure Vessels and Piping,* Volume 188.

Simon, T. K. A. S. C. D. A. E. G., 2010. On the multiplication of dislocation during martensitic transformation in NiTi shape memory alloys. *Acta Materialia,* 58(5), pp. 1850-1860.

Singh, A. & Balasingh, C., 2001. X-ray diffraction line broadening under elastic deformation of a polycrystalline sample: An elastic-anisotropy effect. *Journal of Applied Physics,* 90(5).

Soleimanian, V. M. M., 2015. A comparison between different X-Ray diffraction line broadening analysis methods for nanocrystalline ball milled FCC powders. *Applied Physics,* Volume A, pp. 977-987.

Song Z, Li J, Davis KD, Li X, Zhang J, Zhang L, Sun X. Emerging Applications of Synchrotron Radiation X-Ray Techniques in Single Atomic Catalysts. Small Methods. 2022 Nov;6(11):e2201078. doi: 10.1002/smtd.202201078. Epub 2022 Oct 7. PMID: 36207288.

Speakman, S., 2014. *Estimating Crystallite Size using XRD,* s.l.: MIT Centre for Materials Science and Engineering.

Stephens, R., 2001. *Metal Fatigue in Engineering.* 2nd ed. Iowa: John Wiley.

Stokes, A. R., 1948. A Numerical Fourier-Analysis Method for the Correction of Widths and Shapes of Lines on X-ray Powder Photographs. *Proceedings of the Physical Society,* 6(4), p. 382.

Swapp, S., 2022. *University of Wyoming.* [Online] Available at: https://serc.carleton.edu/person/1955.html [Accessed 21 February 2022].

Technology, N. I. o. S. &., 2015. *Standard Reference Material® 660c,* United States of America, Gaithersburg: Department of Commerce.

Toby, B., 2019. Estimating observed structure factors without a structure. *International Tables for Crystallography ,* Volume H, p. 468.

Ungar, T., 2001. Crystallite size distribution and dislocation structure determined by diffraction profile analysis: principles and practical application to cubic and hexagonal crystals. *Applied Crystallography,* Volume 34, pp. 298-310.

Ungár, T., 2001. Dislocation densities, arrangements and character from X-ray diffraction experiments. *Materials Science and Engineering: A,* Volume 309-310, pp. 14-22.

V. Tong, E. B. B., 2018. Characterisation of slip and twinning in high rate deformed zirconium with electron backscatter diffraction. *Materials Science.*

Valerio, A. & Morelhao, S., 2019. Usage of Scherrer's formula in X-ray diffraction analysis of size distribution in systems of monocrystalline nanoparticles.

Vincentis, N. D., 2017. XRD and EBSD analysis of anisotropic microstructure development in cold rolled F138 stainless steel. *Materials Characterization,* Volume 123, pp. 137-152.

Viswanathan, R., 1989. *Damage Mechanisms and life assessment of High Temperature Components.* USA: ASM International.

Vogel, D., 2013. *Measuring techniques for deformation and stress analysis in micro-dimensions.* Wroclaw, Poland, IEEE.

Warren, B., 1969. Diffraction by Imperfect Crystals. In: *X-Ray Diffraction.* s.l.:Addison-Wesley.

Warren, B. A. B., 1950. The Effect of Cold-Work Distortion on X-Ray Patterns. *J. Appl. Phys,* Volume 21, pp. 595-599.

Warren, B. A. B., 1950. The Effect of Cold-Work Distortion on X-Ray Patterns. *Apllied Physics,* Volume 21, pp. 595-599.

Weidner, A. P. F. B. H., 2013. Scanning and transmission electron microscopy investigations of defect arrangements in a two-phase g-TiAl alloy. *Materials Science & Engineering,* Volume 571, pp. 49-56.

Welze, U. L. J. L. P. V. A. M. E., 2004. Stress analysis of polycrystalline thin films and surface regions by X-ray diffraction. *Journal of Applied Crystallography,* 38(1), pp. 1-29.

Willamson, G. H. W., 1953. X-ray line broadening from Filed Aluminium and Wlfram. *Acta Metall,* Volume 1, pp. 22-31.

Williams, J., 2003. *Electron Microscopy,* Texas: Sam Houston State University.

Williamson, G. H. W., 1953. X-ray line broadening from filed aluminium and wolfram. *Acta Metallurgica,* 1(1), pp. 22-31.

Wright S.I., N. M. a. F. D., 2011. A review of strain analysis using Electron Backscatter Diffraction. *Microscopy and Microanalysis,* Volume 17, pp. 316-329.

Xi X., D. G. W. L. H. J. S. C. a. W. J., 2022. Formation mechanism of faulted bands and its effect on α'-martensitic transformation. *Materials & Design,* Volume 224.

Xina, J. Z. H. S. W. W. W. W. D. L. B. S. F. F. Z. H. C. L. L., 2023. Microstructure evolution of austenitic stainless steels under high-cycle-fatigue loading at deep cryogenic temperature. *Scripta Materialia,* Volume 226.

Xu Z., H. Z. S. Y. F. X. R. M. L. X. H. A. Z. J. F. F., 2018. Topic Review: Application of Raman Spectroscopy Characterization in Micro/Nano-Machining. *Micromachines,* Volume 9.

Yeddu, H. K., 2012. *Martensitic Transformations in Steels - A 3D phase-filed study,* Stockholm, Sweden: KTH Industrail Engineering and Management.

Zhang, Z. H. Z. S. S., 2016. Cyclic behaviour of 12%Cr ferritic-martensitic steel upon long-term on-site service in power plants. *Fatigue & Fracture of Engineering Matrials & Structures,* 39(10), pp. 1179-1192.

Zheng CL et al, 2013. Measurement of chromatic aberration in STEM and SCEM by coherent convergent beam electron diffraction. *Ultramicroscopy,* Volume 125, pp. 49-58.

Zhuo, W. X. Y. B. M. G. J. M. R. Z. J., 2020. XRD and SEM/EDS characterization of two quanernary fuel alloys (U-2.5Mo-2.5Ti-5.0Zr and U-1.5Mo-1.5Ti-7.0Zr in wt.%) for fast reactors. *Materials Characterization,* Volume 170.

Appendix A TOPAS script

```
out_file = Concat(String(filename), ".out");


do_errors
RAW(filename)
  r_exp  4.25792745 r_exp_dash  10.8317665 r_wp  5.01632373 r_wp_dash  12.7610552 r_p
3.92804177 r_p_dash  12.0675851 weighted_Durbin_Watson  1.54891396 gof  1.17811395
  range 1
  bkg @ 1666.897864 122.4544228 0
  start_X  20
  finish_X  125
  LP_Factor( 0)
  One_on_X(@, 6378.595539)
  Specimen_Displacement(height,-0.0`_0.01)
  Rp 141
  Rs 141
  lpsd_th2_angular_range_degrees  3.220261914
    lpsd_equitorial_divergence_degrees  1.422439897
    lpsd_equitorial_sample_length_mm  21.73365404_LIMIT_MIN_0.0001
    lpsd_beam_spill_correct_intensity 0
  axial_conv
    filament_length  13_LIMIT_MIN_0.0001
    sample_length  15_LIMIT_MIN_0.0001
    receiving_slit_length  12_LIMIT_MIN_0.0001
```

```
  primary_soller_angle  2.5
  secondary_soller_angle  2.5
  axial_n_beta  30
Absorption(@, 116.50112`_7.59136)
lam
  ymin_on_ymax  0.0001
  la  0.378 lo  1.7889847 lh  0.4633522
  la  0.144 lo  1.7892524 lh  0.6958819
  la  0.127 lo  1.7896946 lh  1.176738
  la  0.088 lo  1.7888515 lh  0.208542
  la  0.197 lo  1.7927905 lh  0.4127550602
  la  0.095 lo  1.7930637 lh  0.7190761
  la  0.05 lo  1.7934738 lh  1.1578452
xo_ls
  xo @  51.13
  LVol_FWHM_CS_G_L( 1, 264.758736, 0.89, 370.1350245,,,csl, 200)
  e0_from_Strain( 0.0001909655365, gs, 0.1,,)
  I @  296.75786`_0.82329
  peak_type fp
xo_ls
  xo @  59.71
  LVol_FWHM_CS_G_L( 1, 264.758736, 0.89, 370.1350245,,,csl, 200)
  e0_from_Strain( 0.0001909655365, gs, 0.1,,)
  I @  268.41249`_1.26603
xo_ls
  xo @  89.47
```

```
  LVol_FWHM_CS_G_L( 1, 264.758736, 0.89, 370.1350245,,,csl, 200)
  e0_from_Strain( 0.0001909655365, gs, 0.1,,)
  I @  623.38053`_2.26581
xo_ls
  xo @  111.17
  LVol_FWHM_CS_G_L( 1, 264.758736, 0.89, 370.1350245,,,csl, 200)
  e0_from_Strain( 0.0001909655365, gs, 0.1,,)
  I @  119.00082`_1.11281
xo_ls
  xo @  119.00
  LVol_FWHM_CS_G_L( 1, 264.758736, 0.89, 370.1350245,,,csl, 200)
  e0_from_Strain( 0.0001909655365, gs, 0.1,,)
  I @  119.00082`_1.11281
```

Appendix B PXRD FWHM using PVII fit

1. Annealed specimen

FWHM						
RAM280_5 (Annealed)	51.1	59.7	89.5	111.1	119	r_wp
RAM280_5_1.out	0.07082	0.10351	0.09176	0.13927	0.13923	2.996501
RAM280_5_2.out	0.06932	0.08418	0.10474	0.13321	0.13453	2.917082
RAM280_5_3.out	0.10049	0.11653	0.11698	0.13158	0.13606	3.194006

Instrument subtracted (average of 3 samples)

RAM280_5 (Annealed)	51.1	59.7	89.5	111.1	119
RAM280_5_1.out	0.010342355	0.044342995	0.020542	0.043218	0.030717
RAM280_5_2.out	0.008842355	0.025012995	0.033522	0.037158	0.026017
RAM280_5_3.out	0.040012355	0.057362995	0.045762	0.035528	0.027547
Average	0.019732355	0.042239662	0.033275	0.038635	0.028093

2. 500K samples specimen

RAM280_2 (500k)	51.1	59.7	89.5	111.1	119	r_wp
RAM280_2_1.out	0.0748	0.09258	0.12688	0.19119	0.17912	3.193226
RAM280_2_2.out	0.07084	0.08647	0.12291	0.17367	0.15927	3.488636
RAM280_2_3.out	0.09862	0.1026	0.12714	0.17824	0.17227	3.183956

Instrument subtracted (average of 3 samples)

RAM280_2 (500k)	51.1	59.7	89.5	111.1	119
RAM280_2_1.out	0.014322355	0.033412995	0.055662	0.095138	0.070607
RAM280_2_2.out	0.010362355	0.027302995	0.051692	0.077618	0.050757
RAM280_2_3.out	0.038142355	0.043432995	0.055922	0.082188	0.063757
Average	0.020942355	0.034716328	0.054425	0.084982	0.061707

3. 1 million cycles specimen

RAM280_3 (1M)	51.1	59.7	89.5	111.1	119	r_wp
RAM280_3_1.out	0.08403	0.11251	0.12111	0.18177	0.18536	3.296526
RAM280_3_2.out	0.07134	0.10002	0.12147	0.19581	0.16308	3.066062
RAM280_3_3.out	0.07914	0.10379	0.10755	0.19714	0.17752	3.428912

Instrument subtracted (average of 3 samples)

RAM280_3 (1M)	51.1	59.7	89.5	111.1	119
RAM280_3_1.out	0.023552355	0.053342995	0.049892	0.085718	0.076847
RAM280_3_2.out	0.010862355	0.040852995	0.050252	0.099758	0.054567
RAM280_3_3.out	0.018662355	0.044622995	0.036332	0.101088	0.069007
Average	0.017692355	0.046272995	0.045492	0.095522	0.066807

4. 3 million cycles specimen

RAM280_4 (3M)	51.1	59.7	89.5	111.1	119	r_wp
RAM280_4_1.out	0.09133	0.14973	0.18679	0.29152	0.21136	3.178431
RAM280_4_2.out	0.09679	0.14388	0.18338	0.26428	0.21755	3.321814
RAM280_3_3.out	0.09299	0.16682	0.19967	0.28083	0.20486	3.393832

Instrument subtracted (average of 3 samples)

RAM280_4 (3M)	51.1	59.7	89.5	111.1	119
RAM280_4_1.out	0.030852355	0.090562995	0.115572	0.195468	0.102847
RAM280_4_2.out	0.036312355	0.084712995	0.112162	0.168228	0.109037
RAM280_3_3.out	0.032512355	0.107652995	0.128452	0.184778	0.096347
Average	0.033225688	0.094309662	0.118729	0.182825	0.102743

5. 11 million cycles specimen

RAM280_1 (11M)	51.1	59.7	89.5	111.1	119	r_wp
RAM280_1_1.out	0.07588	0.13265	0.14276	0.25268	0.21761	3.320371
RAM280_1_2.out	0.07605	0.12167	0.12968	0.22486	0.20172	3.565624
RAM280_1_3.out	0.08091	0.11445	0.13516	0.23774	0.20881	3.358607

Instrument subtracted (average of 3 samples)

RAM280_1 (11M)	51.1	59.7	89.5	111.1	119
RAM280_1_1.out	0.015402355	0.073482995	0.071542	0.156628	0.109097
RAM280_1_2.out	0.015572355	0.062502995	0.058462	0.128808	0.093207
RAM280_1_3.out	0.020432355	0.055282995	0.063942	0.141688	0.100297
Average	0.017135688	0.063756328	0.064649	0.142375	0.100867

6. Extruded specimen

RAM280_6 (Extruded)	51.1	59.7	89.5	111.1	119	r_wp
RAM280_6_1.out	0.13061	0.25354	0.32657	0.48503	0.39274	3.110396
RAM280_6_2.out	0.12537	0.24811	0.31562	0.51494	0.39633	3.003063
RAM280_6_3.out	0.11937	0.23325	0.27097	0.48276	0.41082	2.869392

Instrument subtracted (average of 3 samples)

RAM280_1 (Extruded)	51.1	59.7	89.5	111.1	119
RAM280_1_1.out	0.070132355	0.194372995	0.255352	0.388978	0.284227
RAM280_1_2.out	0.064892355	0.188942995	0.244402	0.418888	0.287817
RAM280_1_3.out	0.058892355	0.174082995	0.199752	0.386708	0.302307
Average	0.064639022	0.185799662	0.233169	0.398192	0.29145

Appendix C MTEX EBSD Commands

```
%create a phase plot

plot(ebsd)

%create a phase plot with band contrast

plot(ebsd, ebsd.bc)

mtexColorMap('black2white')

%plotting mean angular deviation - deviation between experimental patter and theoretical pattern (Kikuchi pattern)

% create a plot showing the Inverse Pole Figure map overlay

plot(ebsd, ebsd.bc, 'micronbar', 'off')

mtexColorMap('black2white')

hold on

plot(ebsd('Austenite'), ebsd('Austenite').orientations, 'FaceAlpha', 0.5)

hold off

% plotting IPF Key with properties

oM = ipfHSVKey(ebsd('Austenite'))

>> plot(oM)


% Grain Analysis

>> [grains] = calcGrains(ebsd)

>> [grains, ebsd.grainId] = calcGrains(ebsd, 'angle', 5*degree)


Grain Boundary Types

For sigma-3 boundaries; first we have to specify the boundary type as an axis-angle pair.

rot = rotation('axis',vector3d(1,1,1),'angle',60*degree);

gB = grains_FMC.boundary('Austenite','Austenite')

ind = angle(gB.misorientation,rot)<10*degree;
```

```
% Plot grain boundary map
close all
plot(gB)
hold on
plot(gB(ind),'linewidth',1.5,…
'linecolor','r')
```

gB = grains_FMC('Austenite') .boundary

```
% to get a map of just the GBs:
plot(gB)
plot(gB('Austenite', 'Austenite'),gB('Austenite',
'Austenite').misorientation.angle/degree,'linewidth', 1.5)
% an analysis of the grain boundaries in your map by making a histogram of the misorientation
angles.
plotAngleDistribuon(gB ('Austenite' ,'Austenite'));
% export the figure directly, here's a new trick.  Save the figure as a MatLab object:
w1 = figure(1);
% export it in, say,  PNG format thus:
set(gcf,'PaperPosionMode','auto') print(w1,'-dpng',  'path_to_your_directory');
[grains,ebsd.grainId,ebsd.mis2mean] = calcGrains(ebsd('indexed'),'angle',10*degree)
% plot a histogram of the misorientation angles
plotAngleDistribution(mori)
xlabel('Misorientation angles in degree')

%plot the misorientation of each point relative to the average value.
plot (ebsd ('Austenite'), ebsd ('Austenite').mis2mean.angle./degree, 'colorrange',[0
4],'antipodal')
mtexColorbar
plot (ebsd ('Austenite'), ebsd ('Austenite').mis2mean.angle./degree,'antipodal')
mtexColorbar
```

```
% plot IPF with grain boundary overlaid
>> plot(ebsd('Austenite'), ebsd('Austenite').orientations, 'FaceAlpha', 0.5)
hold on
>> plot(grains.boundary)
>> hold off
% grain boundary plotting without non-indexed grains
>> ebsd_indexed = ebsd('indexed')
>> plot(ebsd_indexed('Austenite'), ebsd_indexed('Austenite').orientations,
'FaceAlpha', 0.5);
hold on
>> plot(grains.boundary,'lineWidth',2)
>> hold off
% remove one-to-three pixel grains
>> ebsd(grains(grains.grainSize<=3)) = []
>>   [grains.ebsd.grainId]   =     calcGrains(ebsd('indexed'),('threshold',[1*degree,
10*degree])
% smooth grains
>> grains = smooth(grains,5)
% denoise grains
F = halfQuadraticFilter
ebsd = smooth(ebsd,F,grains,'fill')
% compute grain reference orientation deviation (GROD)
grod = ebsd.calcGROD(grains)
% plot the misorientation angle of the GROD
plot(ebsd.grod.angle./degree,'micronbar','off','colorrange',[0 4])
mtexColorbar('title','misorientation angle to meanorientation in degree') mtexColorMap
LaboTex
hold on
plot(grains.boundary,'lineWidth',1.5)
```

```
plot(grains.innerBoundary,'edgeAlpha',grains.innerBoundary.misorienation.angle/(5*degree))
hold off

% Specifying a reasonable small theshold angle δ=2.5◦ the subgrain boundaries can be effectively removed from the KAM.
plot(ebsd,ebsd.KAM('threshold', 2.5*degree)./degree,'micronbar','off')
caxis([0.4])
mtexColorbar
mtexColorMap LaboTex
hold on
plot(grains,boundary,'lineWidth',1.5)
hold off
```

Appendix D Misorientation to Mean Plots for Annealed Stainless Steel

Misorientation to Mean Plots for Annealed specimens of Stainless Steel		
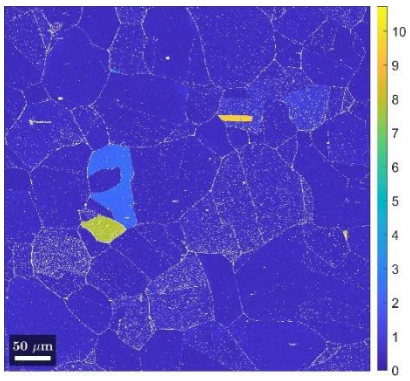	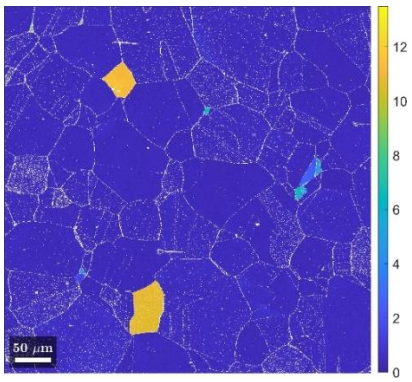	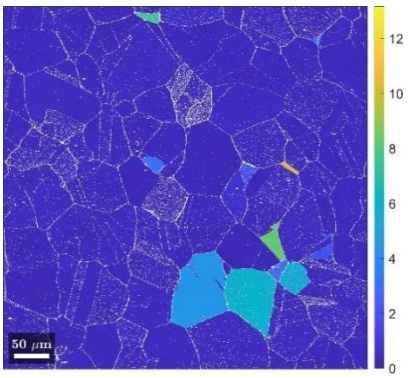
AREA 1	AREA 2	AREA 3
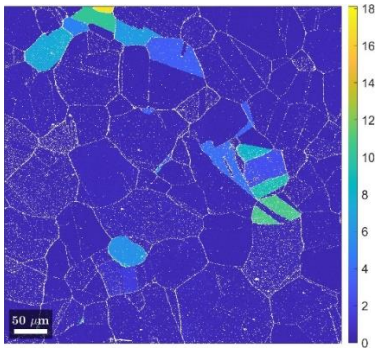	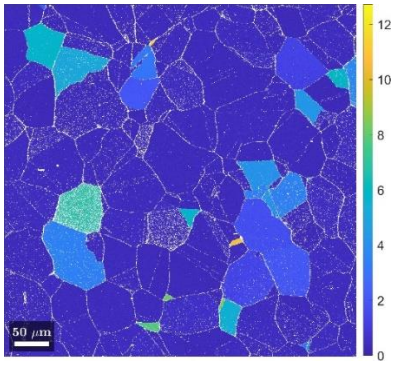	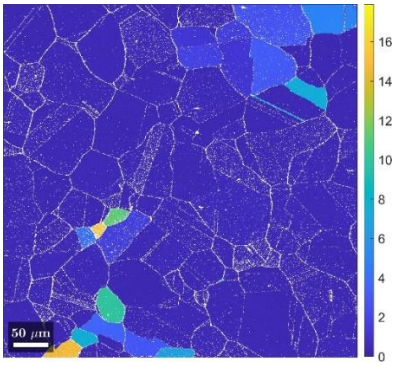
AREA 4	AREA 5	AREA 6

Misorientation to Mean Plots for 500k cycled Stainless Steel		
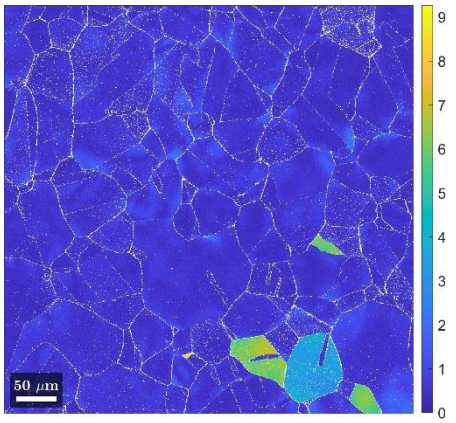	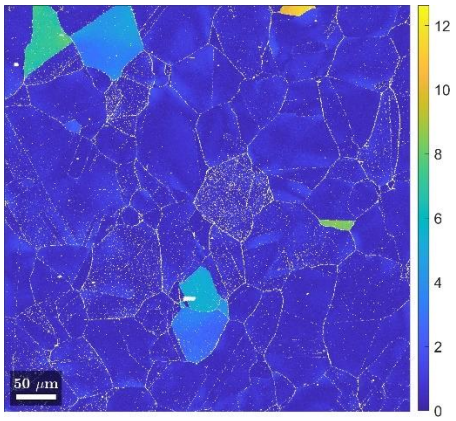	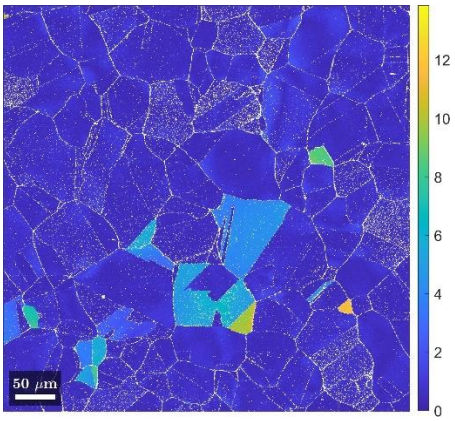
AREA 1	AREA 2	AREA 3
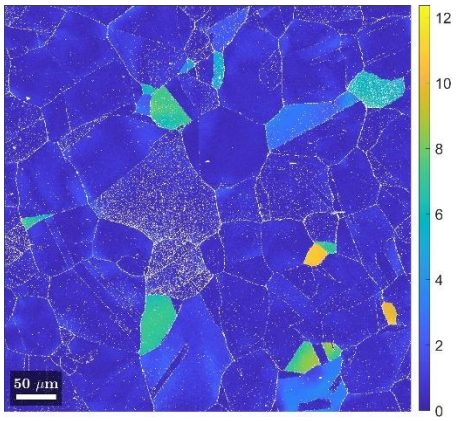	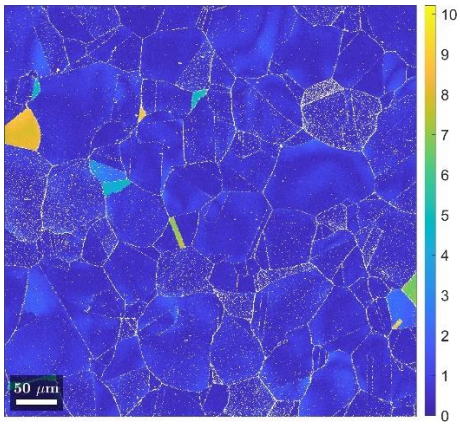	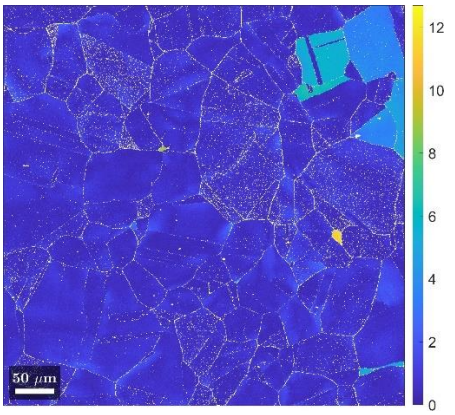
AREA 4	AREA 5	AREA 6

Misorientation to Mean Plots for 1 Million cycled Stainless Steel		
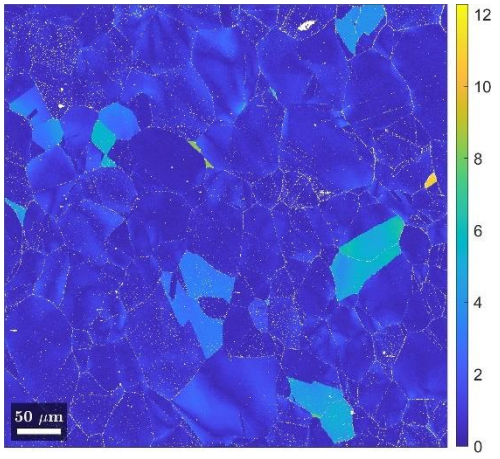	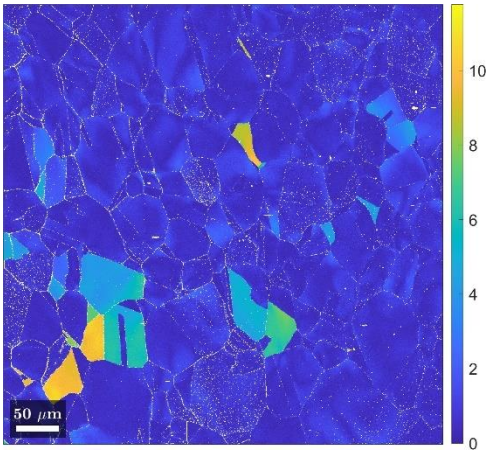	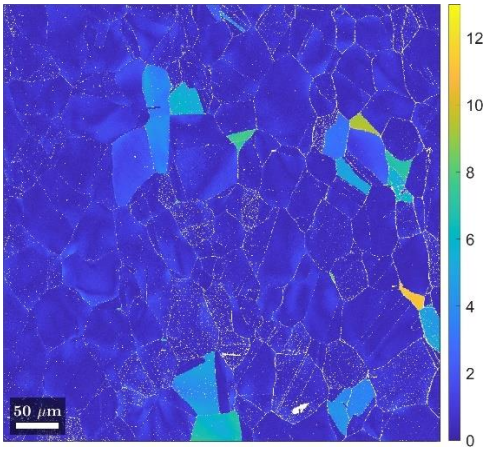
AREA 1	AREA 2	AREA 3
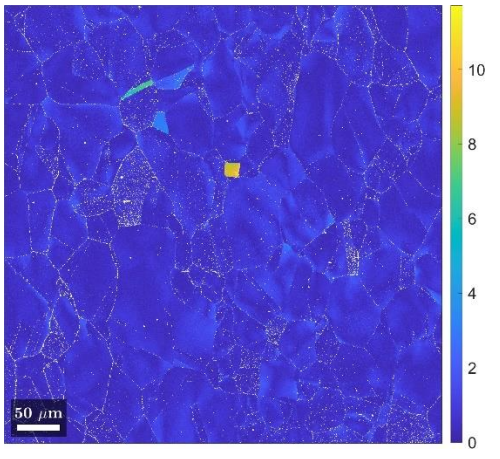	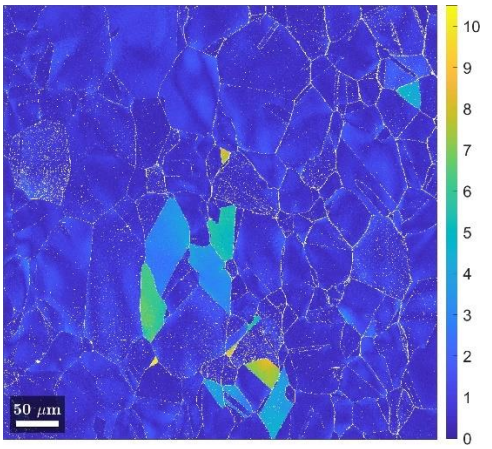	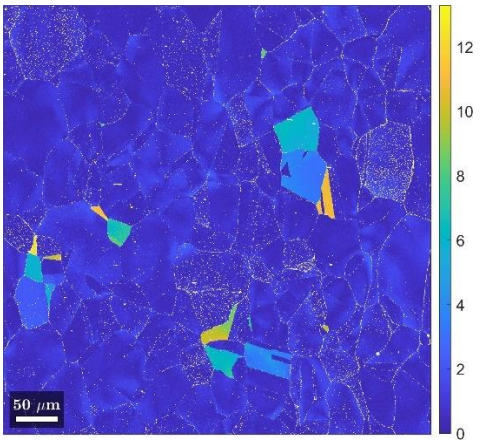
AREA 4	AREA 5	AREA 6

Misorientation to Mean Plots for 3 Million cycled Stainless Steel		
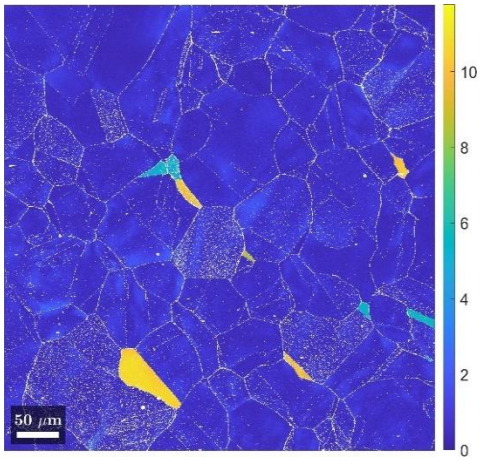	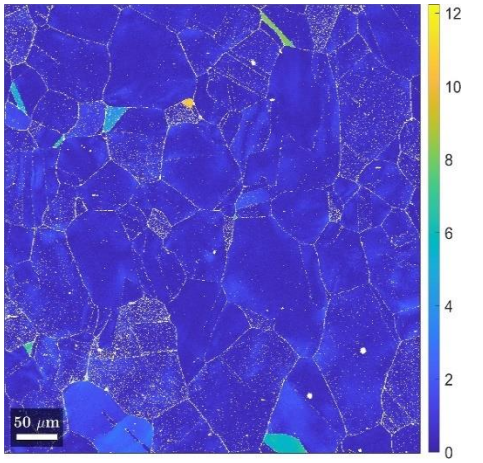	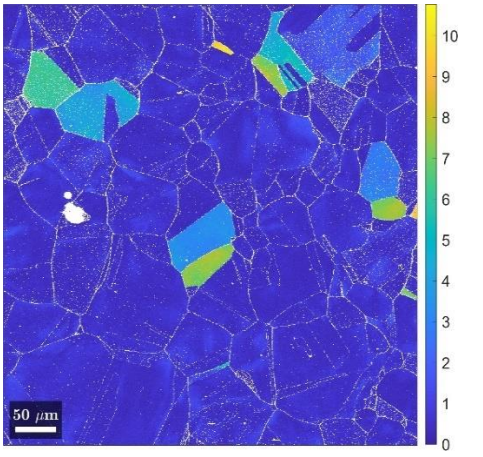
AREA 1	AREA 2	AREA 3
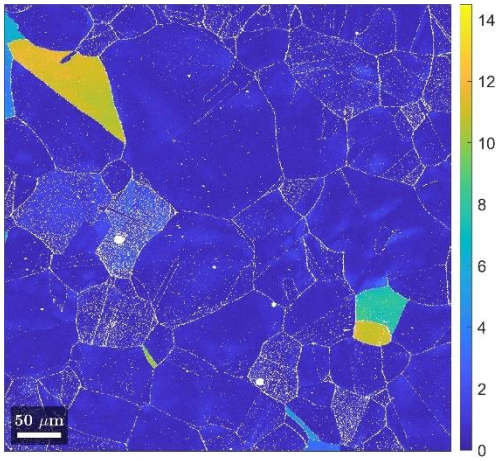	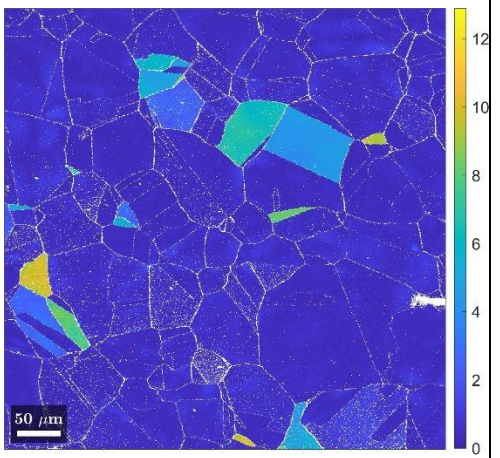	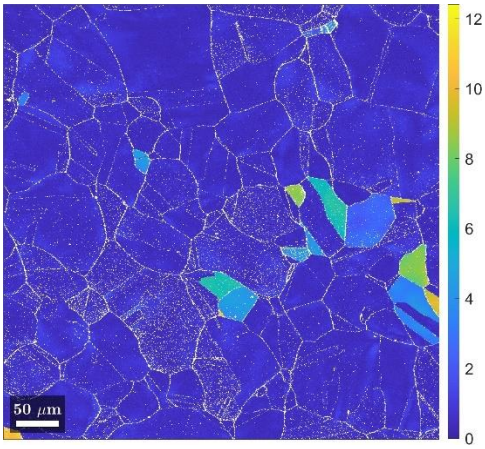
AREA 4	AREA 5	AREA 6

Misorientation to Mean Plots for 11 Million cycled Stainless Steel		
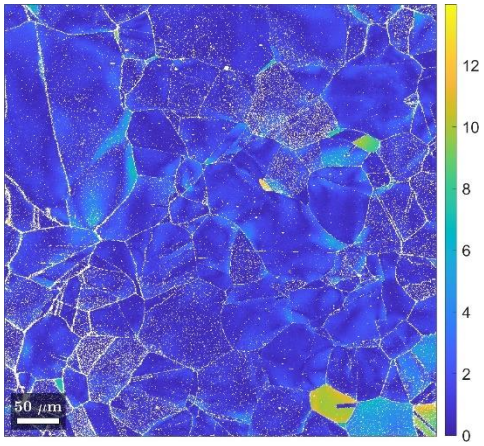	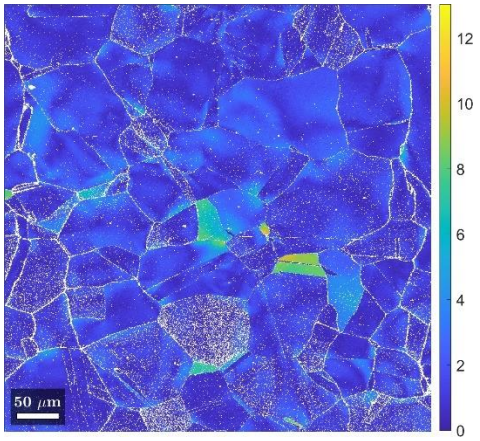	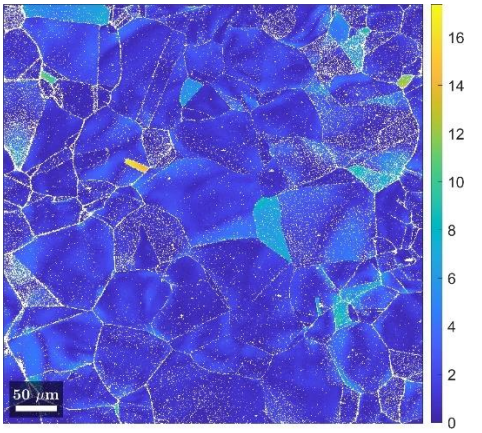
AREA 1	AREA 2	AREA 3
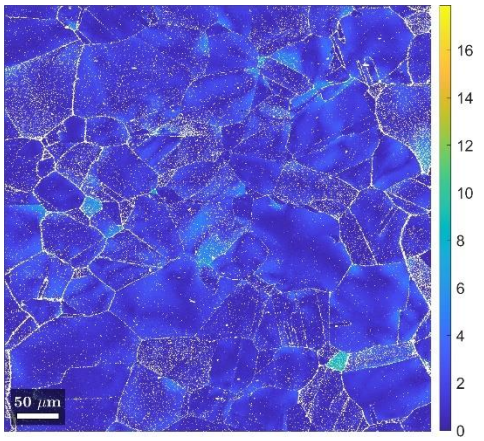	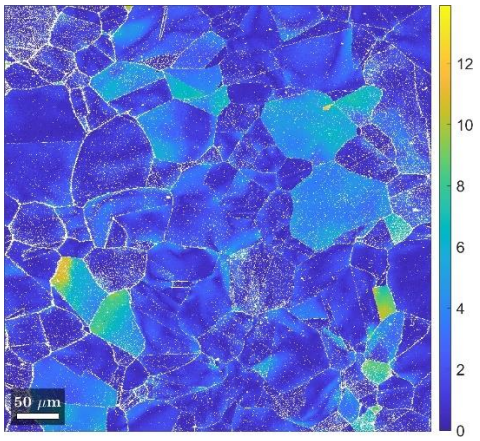	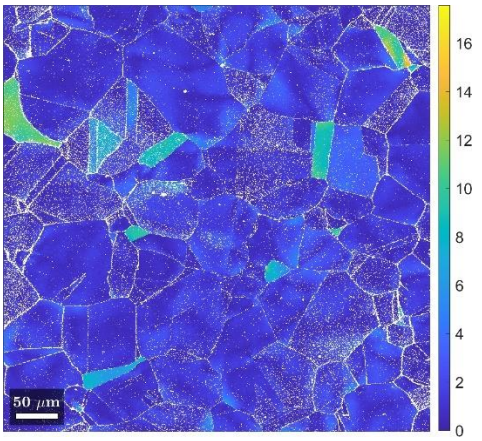
AREA 4	AREA 5	AREA 6

Misorientation to Mean Plots for Extruded Stainless Steel		
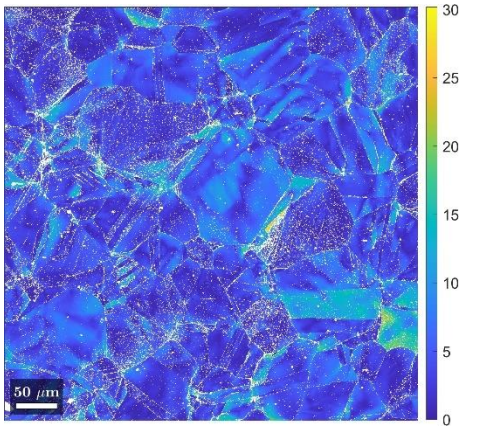	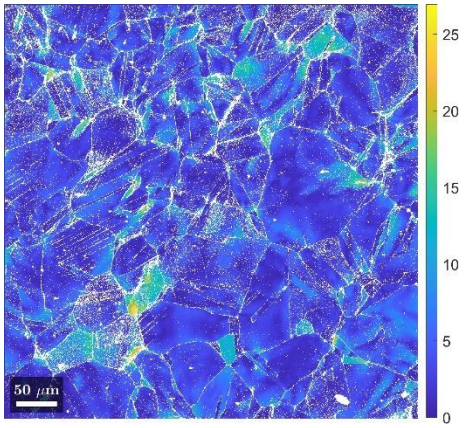	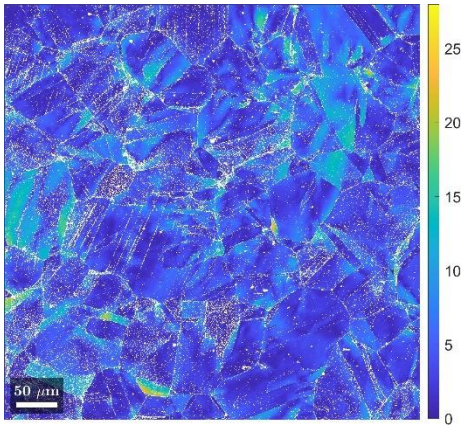
AREA 1	AREA 2	AREA 3
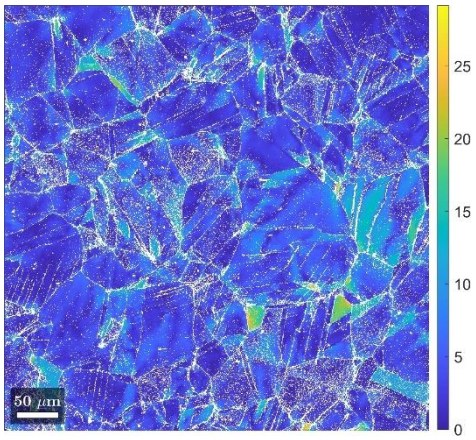	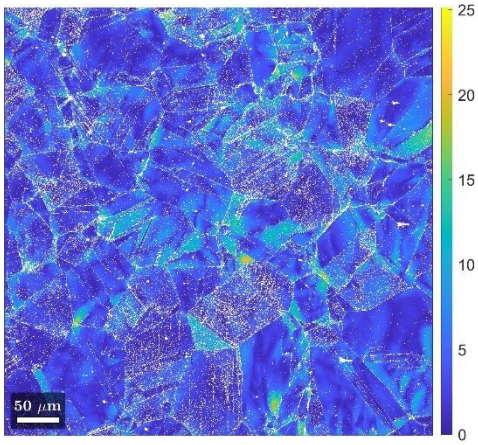	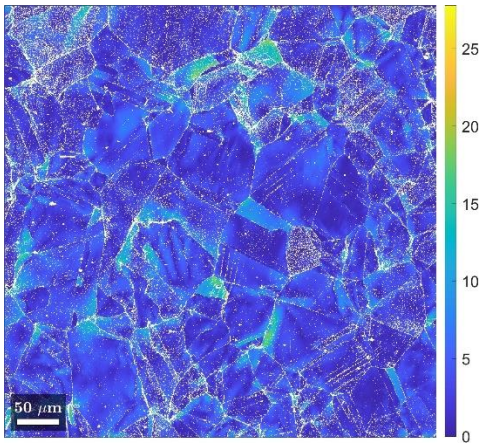
AREA 4	AREA 5	AREA 6

Appendix E TEM images of all material states

ANNEALED SPECIMEN (RAM 5)				
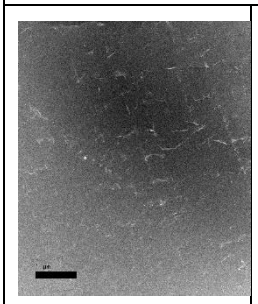 Site 1	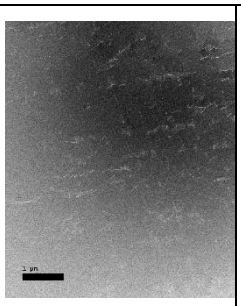 Site 2	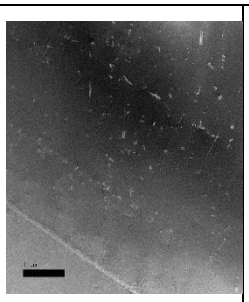 Site 3	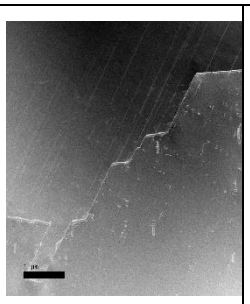 Site 4	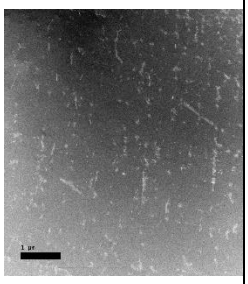 Site 5
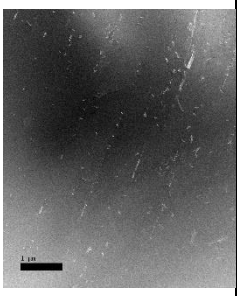 Site 6	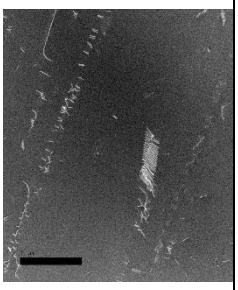 Site 7	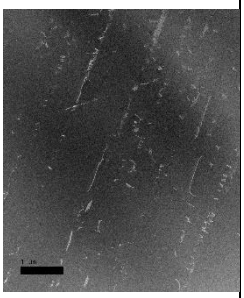 Site 8	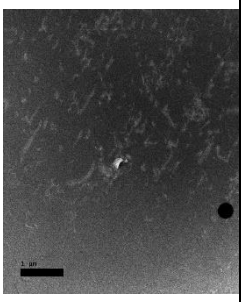 Site 9	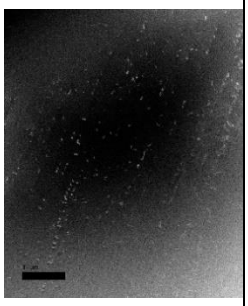 Site 10

500k SPECIMEN (RAM 2)				
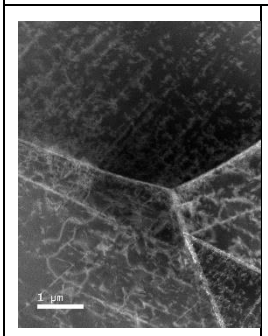 Site 1	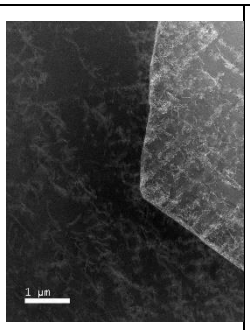 Site 2	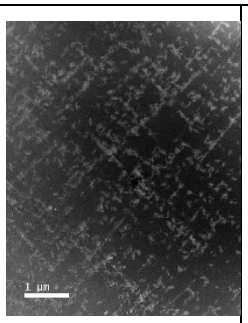 Site 3	 Site 4	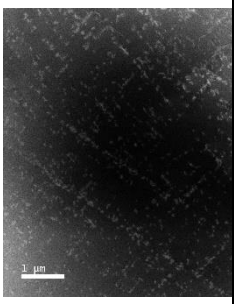 Site 5
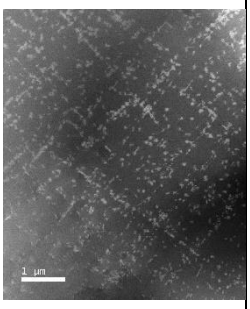 Site 6	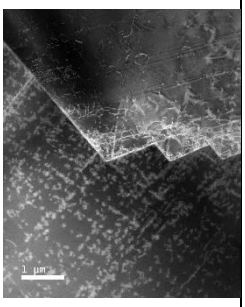 Site 7	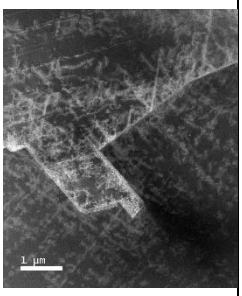 Site 8	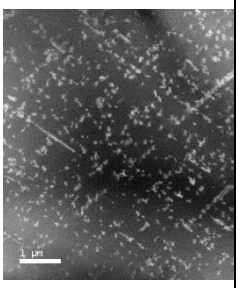 Site 9	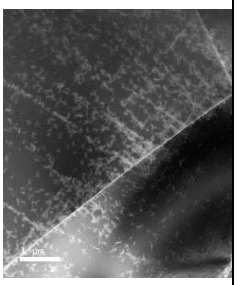 Site 10

1 MILLION SPECIMEN (RAM 3)				
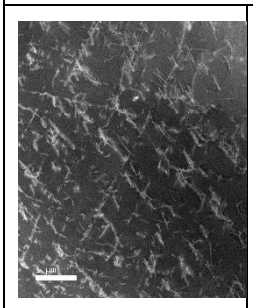 Site 1	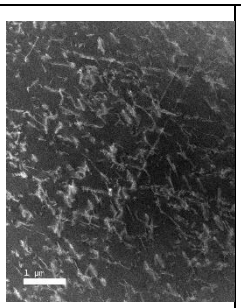 Site 2	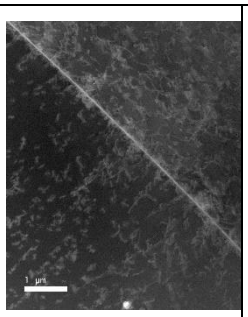 Site 3	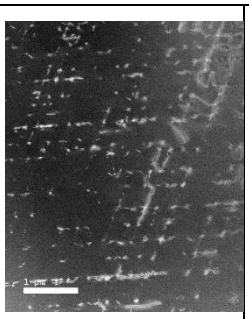 Site 4	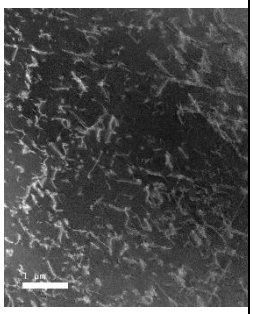 Site 5

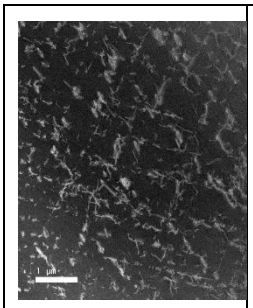	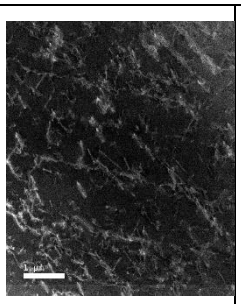	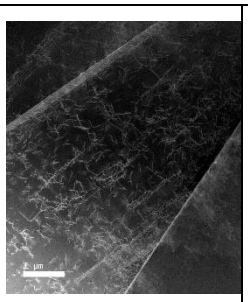	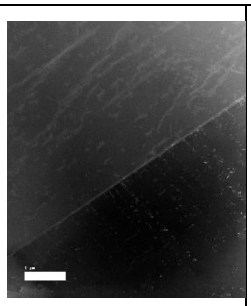	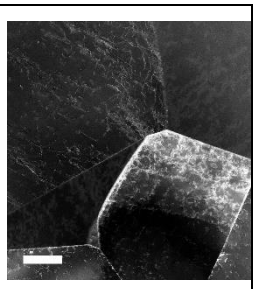
Site 6	Site 7	Site 8	Site 9	Site 10

3 MILLION SPECIMEN (RAM 4)				
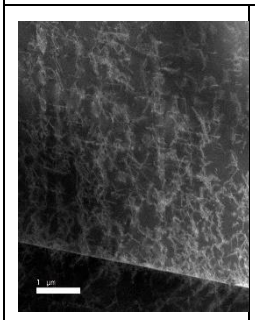		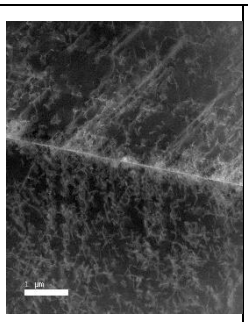	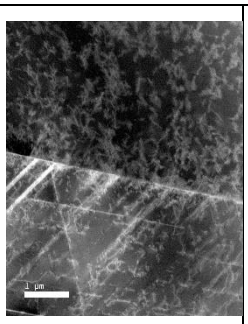	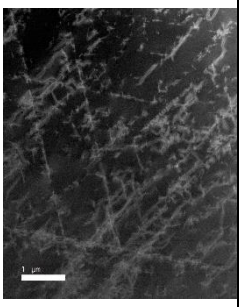
Site 1	Site 2	Site 3	Site 4	Site 5
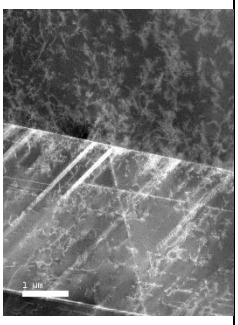	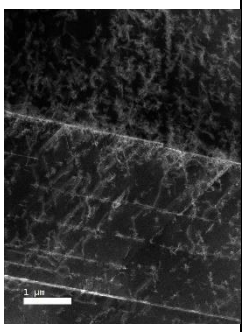	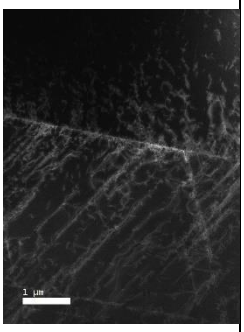	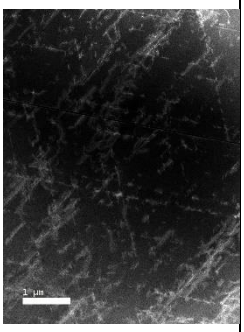	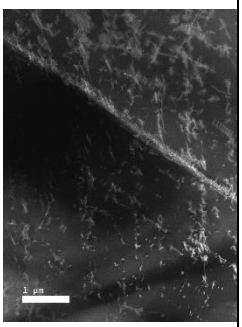
Site 6	Site 7	Site 8	Site 9	Site 10

11 MILLION SPECIMEN (RAM 1)				
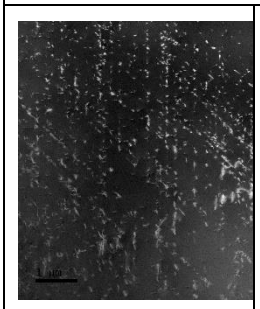	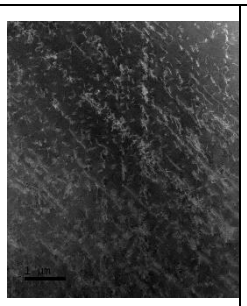	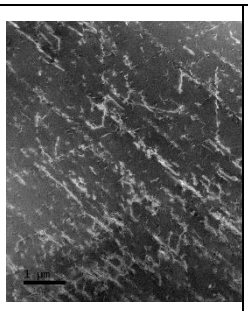	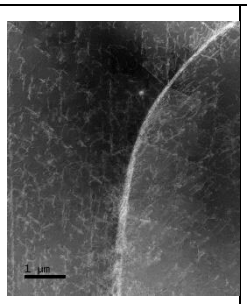	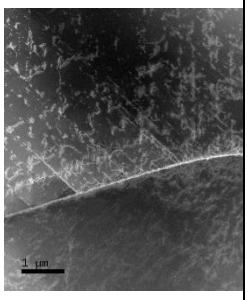
Site 1	Site 2	Site 3	Site 4	Site 5
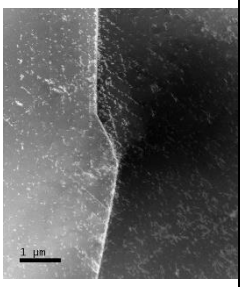	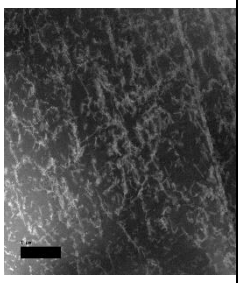	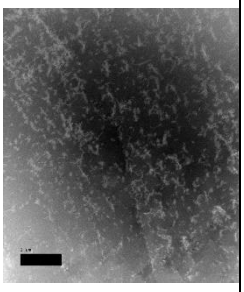	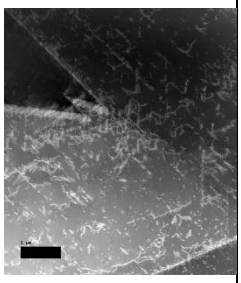	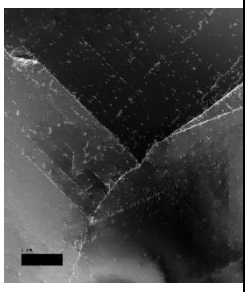
Site 6	Site 7	Site 8	Site 9	Site 10

EXTRUDED SPECIMEN (RAM 6 – 20kx)				
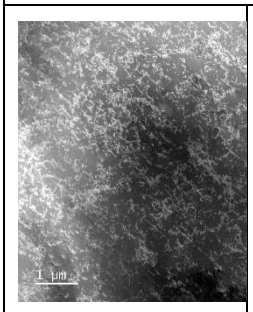	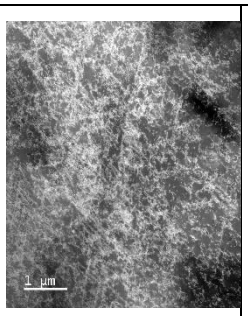	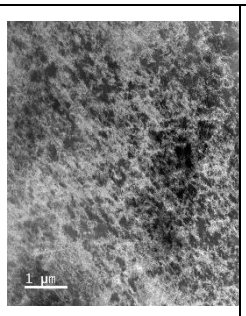		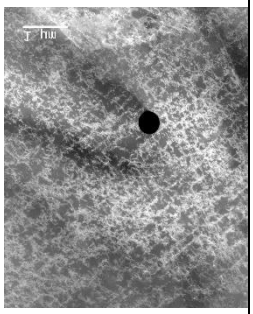
Site 1	Site 2	Site 3	Site 4	Site 5

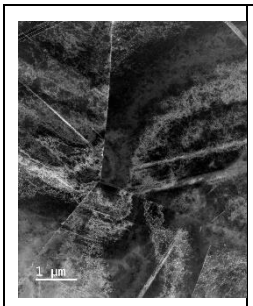	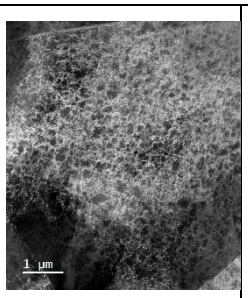	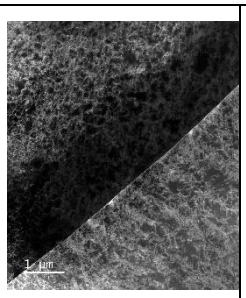	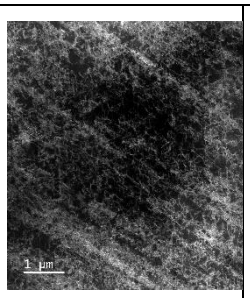	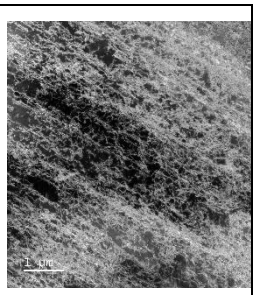
Site 6	Site 7	Site 8	Site 9	Site 10

Appendix F Ethics in research assessment